Crystalline Carbon Nitrides: Characterisation, Intercalation and Exfoliation.

Theo. M. Suter

Thesis submitted for degree Doctor of Philosophy

UCL

Department of Chemistry

March 2018

Declarations

I, Theo M. Suter confirm that the work presented in this thesis is my own. Where information has been derived from other sources, I confirm that this has been indicated in the thesis

Table of Contents

Declarations ... 2

Acknowledgements ... 8

List of figures ... 9

List of tables ... 15

Publications ... 16

Abstract ... 17

Chapter 1 - Introduction ... 19

- 1.1 Technological background ... 19
  - 1.1.1 The indispensability of semiconductors ... 19
  - 1.1.2 Low dimensional materials ... 19
  - 1.1.3 Carbon nitrides ... 20
- 1.2 Classification of carbon nitrides ... 21
  - 1.2.1 Typical terminology of carbon nitrides ... 21
  - 1.2.2 C_xN_y materials ... 23
  - 1.2.3 $C_xN_yH_z$ materials ... 24
  - 1.2.4 N-doped carbons ... 25
- 1.3 Potential applications of carbon nitride materials ... 25
  - 1.3.1 Current applications of gCN ... 25
  - 1.3.2 Potential applications of PTI ... 26
- 1.4 Exfoliation of layered materials ... 26
  - 1.4.1 General exfoliation methods ... 27

Chapter 2 – Methods ... 29

- 2.1 Characterisation techniques ... 29
  - 2.1.1 Scanning electron microscopy (SEM) ... 29
  - 2.1.2 Transmission electron microscopy (TEM) ... 29
  - 2.1.3 Microbeam FTIR ... 29
  - 2.1.4 Elemental analysis ... 30
  - 2.1.5 X-ray photoelectric spectroscopy (XPS) ... 30

    - 2.1.6 UV-Vis..30
    - 2.1.7 Raman Microscopy 30
    - 2.1.8 X-ray diffraction (XRD) 30
    - 2.1.9 Zeta potential and DLS 31
    - 2.1.10 Thermogravimetric analysis (TGA)..31
    - 2.1.11 Fluorescence 31
  - 2.2 High speed atomic force microscopy (AFM) 31
  - 2.3 Synthetic method...32
    - 2.3.1 Swagelok setup..32
- Chapter 3 – Structural characterisation of polytriazine imide (PTI) 33
  - 3.1 The structure of PTI...33
    - 3.1.1 Initial syntheses of PTI materials...33
    - 3.1.2 Identification of PTI.LiCl 35
    - 3.1.3 Identification of PTI.LiBr 36
    - 3.1.4 Further reports on the structure of PTI materials 36
  - 3.2 Synthesis of PTI materials in this thesis..38
    - 3.2.1 Synthetic method for PTI.LiBr and PTI.LiCl 38
    - 3.2.2 Deuterated PTI.LiCl...39
  - 3.3 Characterisation of PTI materials..39
    - 3.3.1 PXRD and Occupancy of PTI materials...39
    - 3.3.2 XPS of PTI materials...43
    - 3.3.3 Vibrational spectroscopy of PTI materials 49
    - 3.3.4 SEM and TEM images of PTI materials...52
    - 3.3.5 TGA analysis...55
- Chapter 4 – De-intercalation and re-intercalation of PTI compounds 57
  - 4.1 Synthesis and characterisation of intercalant free PTI (IF-PTI) 58
    - 4.1.1 Background and context 58
    - 4.1.2 IF-PTI synthesis...58
    - 4.1.3 X-ray photoelectron spectra and analysis..59

4.1.4 NMR and elemental analysis 61
4.1.5 TEM and SEM images 62
4.1.6 PXRD patterns and analysis 63
4.1.7 IR spectra and analysis 64
4.1.8 TGA and estimation of the absorbed water content 65
4.1.9 Summary 66
4.2 Reintercalation of PTI.LiBr and PTI.LiCl 66
4.2.1 Context and synthesis 66
4.2.2 PXRD patterns and analysis 68
4.2.3 XPS spectra and analysis 69
4.2.4 IR spectra and analysis 73
4.2.5 Summary 73
4.3 Synthesis and characterisation of PTI.HCl 74
4.3.1 Context and synthesis 74
4.3.2 XPS spectra and analysis 75
4.3.3 PXRD pattern and literature comparison 77
4.3.4 IR spectra and analysis 78
4.3.5 Summary 79
4.5 UV spectra of the different intercalated PTI materials 80
4.4.1 UV spectra and analysis 80
4.6 Conclusions 82
Chapter 5 – Exfoliation of PTI in aprotic polar solvents 83
5.1 Introduction 83
5.1.1 Exfoliation of PTI materials 83
5.2 Exfoliation of PTI.LiBr via alkali metal intercalation 83
5.2.1 Vapour intercalation of potassium followed by exfoliation in water 83
5.2.2 Lithium metal intercalation via liquid ammonia and exfoliation in organic solvents 85
5.2.3 Experimental method and initial observations 86

5.3 Dissolution of PTI.LiBr via sonication in aprotic polar solvents....87
5.3.1 Experimental methods and observations....88
5.3.2 Characterisation of deposited nanosheets....89
5.4 Spontaneous dissolution in aprotic polar solvents....90
5.4.1 Experimental methods and observations....90
5.4.2 Investigation of different solvents....92
5.4.3 Characterisation of the PTI.LiBr solutions....94
5.4.4 Characterisation of the deposited nanosheets....101
5.5 Conclusion....108
Chapter 6 – Spontaneous exfoliation of PTI in water....109
6.1 Experimental method and initial observations....109
6.2 TEM imaging and EDX mapping of the deposited nanosheets....111
6.3 The effect of pH on the dissolution of PTI.LiBr water solutions....115
6.3.1 UV-visible spectra PTI.LiBr solutions with different starting pH....116
6.3.2 pH of water before and after the addition of carbon nitrides....118
6.3.3 The effect of different starting mass on the concentration of PTI.LiBr solutions....119
6.4 Conclusion....121
Chapter 7 – Triazine based graphitic carbon nitride (TGCN)....123
7.1 Synthesis of ‘TGCN’....123
7.2 Characterisation of resultant material....125
7.2.1 Visual images of the recovered materials....125
7.2.2 TEM and SEM of the flakes....126
7.2.3 Powder and reflection geometry XRD....129
7.2.4 CNH analysis....130
7.2.5 XPS of the recovered flakes....132
7.2.6 The C:N ratio and structural implications....134
7.2.7 IR and Raman studies....137
7.3 Conclusions....138

Chapter 8 – Conclusion and outlook 141
Chapter 9 – Appendix 143
  9.1 Collection of TEM images of the flakes discussed in Chapter 7 143
References 149

Acknowledgements

There are a great many people I would like to thank who have made this journey not only possible but also interesting and unique.

First I would also like to thank my primary and secondary supervisors, Professor Paul McMillan and Dr Chris Howard for their knowledge, expertise, time and effort that got me to where I am now. In particular Professor Paul McMillan for his hard work turning into an effective researcher and Dr Chris Howard who has been incredibly supportive of me during this long process.

Secondly I would like to thank all those fellow students, researchers and technicians at UCL who are always willing to help out and answer a few questions. In particular I would like to thank Dr Thomas Miller for being what feels like my personal guide on the world of science and academia, his help and guidance have been so valuable over the last 3 years, and especially since I started writing this thesis. Professor Andrea Sella for always being more than happy to help out in a crazy scheme of mine, and re-introducing me to love of science when PhD life got me down. There are so many others that have helped me out, discussed science or chatted about nothing with, that I cannot mention them all by name, but I thank them all.

I would also like to thank my friends and family who have and continue to be always there for me. Your support, understanding and friendship has been invaluable over the last three years, so thank you so much.

Any finally I would like to thank the person that I only met one year into my PhD but has come to mean so much to me. It is to her that the credit of this thesis should go, without her love, support and understanding I would have not made it this far. She picked me up when I was down and has been pushing me on the entire time. I could not have done this without you. So thank you so much Ms Winnie Leung, and I wish you the best of luck on your own PhD journey.

List of figures

Figure 1.1 Ternary diagram showing the C/N/H compositions of various carbon nitride structures plotted with a red tie-line indicating the path a material will take if it losses only NH_3 components, also indicated is N-doped carbons. 21

Figure 1.2. Diagram showing the relationship of different carbon nitride materials and how they are commonly referred to in the literature. 22

Figure 1.3. Molecular structures of idealised carbon nitride materials. a) Melamine. b) Melem. c) Triazine based C_3N_4. d) Heptazine based g-C_3N_4. 23

Figure 1.4. Molecular structure of several hydrogen containing carbon nitride materials. a) Melon. b) Polytriazine imide. 24

Figure 2.1. Picture showing the Swagelok setup and quartz ampoule for both the larger and smaller tubes 32

Figure 3.1. Diagrams of triazine based layered crystalline carbon nitrides. (a) The polytriazine imide ‘backbone’ structure. (b) The polytriazine imide structure reported by Zhang *et al.*[129] H^+ and Cl^- ions are intercalated into the material as shown above. 34

Figure 3.2. Diagram showing the structure of PTI.LiCl. a) A charge balanced structure of PTI.LiCl showing the position of the chloride anion and the assumed position of the lithium cations. The lithium can either act as the counter ion to the chloride or it can replace the hydrogen on the bridging imide. Typically each void would have one chlorine, two hydrogens and two lithiums. It is possible that some of the voids are unoccupied. b) A diagram of PTI.LiCl showing the stacking and the intercalated chlorine between the layers. 35

Figure 3.3. a) Experimental and refined PXRD patterns of PTI.LiCl with a hexagonal unit cell. b) Experimental and predicted PXRD patterns of PTI.LiCl with an orthorhombic unit cell. c) Experimental and refined PXRD patterns of PTI.LiBr with a hexagonal unit cell. 40

Figure 3.4. The calculated XRD pattern as a function of halide percentage occupancy of two types of PTI materials. (a) PTI.LiCl. (b) PTI.LiBr. 41

Figure 3.5. C1s and N1s XPS spectra of melamine and carbon tape. a) Carbon 1s spectrum of melamine. b) Carbon 1s spectrum of carbon tape. c) Nitrogen 1s spectrum of melamine. d) Nitrogen 1s spectrum of carbon tape. 43

Figure 3.7. XPS Spectra of PTI.LiCl. (a) Survey spectrum. (b) Carbon 1s spectrum. (c) Nitrogen 1s spectrum. (d) Chlorine 2p spectrum. (e) Lithium 1s spectrum. 47

Figure 3.8. ATR FTIR spectra of PTI materials. a) Normalised IR spectra of PTI.LiCl and PTI.LiBr. b) Spectrum of deuterated PTI.LiBr. 49

Figure 3.9. Raman spectra of PTI.LiBr at several different excitation wavelengths, 325 nm is shown in red, 514.5 nm is shown in black and 785 nm is shown blue. 50

Figure 3.10. SEM images of bulk PTI materials. a) Image of PTI.LiBr showing large areas of hollow tubes. b) Image of PTI.LiBr showing hexagonal crystallites growing on the side of hollow tubes. c) Image of PTI.LiCl showing hexagonal crystallites face up as well on stacks on the side. d) Image of PTI.LiBr showing the hexagonal crystallites attached to the side of the hollow tubes as well as growing as a large block. 52

Figure 3.11. TEM images and SAED pattern of bulk PTI.LiBr. a) TEM image of various unaligned PTI crystallites. b) SAED of bulk PTI.LiBr showing the distances of the first three rings. c) Histogram of crystallite sizes counted from (a). d) TEM image of a tubular structure of PTI.LiBr crystallites. 53

Figure 3.12. TGA of PTI.LiBr showing the mass change of the sample as it is heated to 900°C at 20°C min^{-1}. 55

Figure 4.1. XPS Spectra of IF-PTI. (a) Survey spectrum. (b) Carbon 1s spectrum. (c) Nitrogen 1s spectrum. (d) Bromine 3p spectrum. (e) Lithium 1s spectrum. 59

Figure 4.2. Solid state ^{7}Li MASS NMR of two different PTI materials. a) PTI.LiBr. b) IF-PTI. 61

Figure 4.3. TEM images of IF-PTI. a) TEM image showing crystalline IF-PTI hexagons. b) Fourier transformed of the selected area shown in (a). c) TEM image showing large tube formed from PTI crystallites. 62

Figure 4.4. PXRD pattern of dried IF-PTI before and after exposure to air. 63

Figure 4.5. ATR-IR spectra of IF-PTI showing the comparison between PTI.LiBr and IF-PTI, also shown is the difference between IF-PTI after exposure to air for 2 minute and after 5 minutes. 64

Figure 4.6. TGA of wet IF-PTI showing only two mass loss events one associated with carbon nitride and the other with the removal of the intercalants, the sample was heated to 900˚C at 20˚C min^{-1}. 65

Figure 4.7. PXRD patterns showing as synthesised PTI compared against the washed and re-intercalated material. a) PTI.LiCl and Ri-PTI.LiCl. b) PTI.LiBr and Ri-PTI.LiBr. 68

Figure 4.8. XPS Spectra of Ri-PTI.LiCl (a) Survey spectrum. (b) Carbon 1s spectrum. (c) Nitrogen 1s spectrum. (d) Chlorine 2p spectrum. (e) Lithium 1s spectrum. 69

Figure 4.10. ATR-IR spectra showing the prewashed and re-intercalated PTI materials. a) PTI.LiBr and Ri-PTI.LiBr. b) PTI.LiCl and Ri-PTI.LiCl. 73

Figure 4.11. XPS Spectra of PTI.HCl. (a) Survey spectrum. (b) Carbon 1s spectrum. (c) Nitrogen 1s spectrum. (d) Chlorine 2p spectrum. (e) Lithium 1s spectrum. 75

Figure 4.12. Experimental PXRD of PTI.HCl showing a close match when compared with peak positions reported by Zhang *et al.*[129] 77

Figure 4.13. ATR-IR spectra of PTI.HCl compared with PTI.LiCl showing a very similar C-N bonding profile but additional vibrations in the 2700 – 3000 cm^{-1} region. 78

Figure 5.1. PXRD patterns and SEM images of potassium intercalated PTI.LiBr. a) PXRD pattern of potassium intercalated PTI.LiBr compared with PTI.LiBr and simulated KBr. b) SEM images of ‘exfoliated’ potassium intercalated PTI.LiBr. 84

Figure 5.2. Photograph of PTI.LiBr solutions, Left: Non-sonicated DMSO solution, Middle: Sonicated NMP solution, Right: Sonicated DMSO solution. 88

Figure 5.3. TEM and SAED images of sonicated PTI.LiBr dispersion after being dried onto a TEM grid. a) TEM image of PTI.LiBr flake from a DMF dispersion. b) SAED image of the PTI.LiBr flake from a DMF dispersion. c) TEM image of PTI.LiBr flakes from a NMP dispersion. d) TEM image of PTI.LiBr flake and some debris from the NMP dispersion. 89

Figure 5.4. Image showing the colour change in PTI.LiBr solutions over 48h. The solvents used at DMF, NMP and DMSO. 90

Figure 5.5. Pictures showing the dissolution of PTI.LiBr into different solvents overtime, UV-vis spectra of PTI.LiBr solutions and the solvent background. a) Pictures of the dissolution of PTI.LiBr DMSO, DMF, NMP and ethanol over 48 hours under UV-vis lamp and visible light for the DMSO solution. b) UV-vis spectra of DMSO/PTI solution compared with only DMSO solvent. c) UV-vis spectra of NMP/PTI solution compared with only NMP solvent. d) UV-vis spectra of DMF/PTI solution compared with only DMF solvent. 94

Figure 5.6. Graphs showing the zeta potential and particle size distribution data for PTI.LiBr DMF solutions. a) Particle size distribution graph for the DMF solvent. b) Measured zeta potential of the DMF solvent. c) Particle size distribution graph of DMF/PTI.LiBr solution, highlighted is expected diameter of PTI flakes. d) Measured zeta potential of DMF/PTI.LiBr solution. 97

Figure 5.7. Graphs showing the mass remaining as a function of sample temperature of a PTI.LiBr/DMSO solution, calculated via TGA. a) Graph of TGA of PTI.LiBr/DMSO solution showing the loss of the solvent between 100 – 200 ˚C b) Zoom in of the previous graph showing the PTI.LiBr/DMSO compared against bulk PTI.LiBr. 99

Figure 5.8. High resolution TEM images and Fourier transformed image of PTI.LiBr nanoflakes deposited out of NMP solution. a) HR-TEM image of a crystalline and undamaged PTI.LiBr flake. b) SAED of a flake of PTI.LiBr showing the typical lengths observed for PTI.LiBr. c) Zoomed in image of a, the focus has been changed to clearly show the hexagonal PTI structure. d) Image of c with the carbon background removed, the crystal structure of PTI.LiBr has been overlaid. 101

Figure 5.9. TEM calculated projections of PTI.LiBr under different defocus conditions, layer thickness and halide occupancy. a) TEM projection of PTI.LiBr without intercalated halides. b) TEM projection of PTI.LiBr with intercalation halides. 103

Figure 5.11. Photoluminescence emission spectra of PTI nanosheets obtain with excitation wavelengths between 260 - 330 nm. a) PL spectra with a range of excitation wavelengths of PTI.LiBr/DMF solutions, with the intensity normalised to that at ~ 380nm. b) PL spectra with a range of excitation wavelengths of PTI.LiBr deposited from PTI.LiBr/DMF solutions, with intensity normalised to that at ~ 450 nm. In both spectra the sharp peaks are observed at double the excitation wavelength are instrumental in origin. 106

Figure 6.1. Visible and UV-vis images of PTI.LiBr/water solutions a) Image showing the slight yellow colour of the PTI.LiBr/water solution. b) Image of PTI.LiBr/water under UV illumination showing the strong fluorescence of PTI.LiBr dissolved in water............. 110

Figure 6.2. TEM images and Fourier transform of two different PTI.LiBr nanosheets with different thicknesses dried out of a pH 13 water solution. Inset a) Fourier transform image of the thicker PTI.LiBr flake. Inset b) Fourier transformed image of the thinner PTI.LiBr flake. 111

Figure 6.3. EDX image and elemental data of the PTI.LiBr flakes shown in figure 6.2. a) TEM image of the overlapping flakes. b) Nitrogen content with the flake outline marked c) Carbon content with the flake outline marked. d) Bromine content with the flake outline marked e) Oxygen content with the flake outline marked. 112

Figure 6.4. TEM image of a stack of PTI.LiBr flakes from the side showing several different faces of the crystal, Fourier transforms of this different faces are shown (Inset a, b). 114

Figure 6.5. Images of PTI.LiBr/water solutions illumination by UV light. Several different water solutions are shown, the pH before the water was contacted with the PTI.LiBr was 1, 6.5 and 13. 115

Figure 6.6. UV-vis absorbance spectra of PTI.LiBr/water solutions with different initial pH values of the water. pH was measured before it was contacted with PTI.LiBr...... 117

Figure 6.7. A chart showing the pH of water before and after addition of a carbon nitride material........ 118

Figure 6.8. UV-vis absorbance spectra of PTI.LiBr/pH 13 water solutions formed using different quantities of either the solvent or the bulk PTI.LiBr. a) Absorbance spectra of PTI.LiBr /pH 13 water solution formed by different initial mass of PTI.LiBr, with inset showing the change of the relative intensity of the peak at 280 nm with initial mass. b) Absorbance spectra of PTI.LiBr /pH 13 water solution formed by different initial volume of pH 13 water, with inset showing the change of the relative intensity of the peak at 240 nm with initial volume........ 119

Figure 7.1. Pictures of the recovered materials. a) Picture of recovered bulk material showing the dark brown powder mixed with black reflective flakes. b) Black reflective flakes separated from the brown powder. c,d) Front lit images, showing the highly reflective surface of the cleaved flakes. 125

Figure 7.2. SEM images of uncleaved flakes. a) SEM image clearly showing layer stacking and some damage to the top sheet b) SEM image of inhomogeneity on the surface of the flakes as well as showing the layered stacking c) Zoomed out image showing a large crack between the millimetre sized flakes. 126

Figure 7.3. TEM images for an uncleaved thin flake of our sample focussed on a region showing lattice fringes. a) TEM image showing the presence of crystalline domains within a small region of the sample. b) Expanded filtered TEM image of one nanocrystalline region demonstrating the hexagonal layer symmetry with a characteristic 2.6Å separation between bright spots. c) Line scan across the image intensity variations used for the FT determination of the intralayer lattice spacing. d) SAED pattern indicating different crystalline layer orientations sampled by the electron beam passing through the flake........ 127

Figure 7.4. XRD patterns of different parts of the recovered materials a) Rocking geometry of the dark flakes b) PXRD of the dark brown powder. Note the scale of a is given where (λ = 1.54056 Å) and the scale of b is given where (λ = 0.827127 Å). This is for easier comparison to literature data........ 129

Figure 7.6. Schematic showing different types of sp^2 carbon nitride bonding. 133

Figure 7.7. Comparison of the IR and Raman spectra of the synthesised flakes and similar literature structures. a) IR spectrum for nanocrystalline C_3N_4 prepared by CVD synthesis redrawn from Ref,[51, 52] (red curve) IR spectrum for the synthesised flakes. (black curve) b) Unpolarized Raman spectra obtained at normal incidence using different laser excitation wavelengths (325, 514.5, 785 nm) for the synthesised flakes. 137

List of tables

Table 3.1. Table showing the measured characteristic distances from SAED. 54

Table 7.1. Stoichiometry of several carbon nitrides found by CNH analysis. 131

Table 7.2. Carbon and nitrogen composition found from XPS. Different compositions depending on which environments from XPS are considered. 134

Publications

Parts of this thesis have been published in the following articles:

T. S. Miller, T. M. Suter, A. M. Telford, L. Picco, O. D. Payton, F. Russell-Pavier, P. L. Cullen, A. Sella, M. S. P. Shaffer, J. Nelson, V. Tileli, P. F. McMillan, and C. A. Howard. Single Crystal, Luminescent Carbon Nitride Nanosheets Formed by Spontaneous Dissolution. *Nano Lett*, 2017. **DOI:** 10.1021/acs.nanolett.7b01353

T. S. Miller, A. B. Jorge, T. M. Suter, A. Sella, F. Cora and P. F. McMillan, Carbon nitrides: synthesis and characterization of a new class of functional materials. *Phys Chem Chem Phys*, 2017, **19**, 15613-15638. **DOI:**10.1039/C7CP02711G

Two further publications which include work from the thesis are in preparation.

Other articles to which I have contributed but were not a significant part of the thesis:

N. Mansor, J. Jia, T. Miller, T. Suter, A. Belen Jorge, C. Gibbs, P. R. Shearing, P. F. McMillan, C. Mattevi, M. Shaffer and D. J.L Brett. Graphitic Carbon Nitride-Graphene Hybrid Nanostructure as a Catalyst Support for Polymer Electrolyte Membrane Fuel Cells. *ECS Trans.* 2016 volume 75, issue 14, 885-897. **DOI**: 10.1149/07514.0885ecst

T. S. Miller, A. d'Aleo, T. Suter, A. E. Aliev, A. Sella, P. F. McMillan. Pharaoh's Serpents: New Insights into a Classic Carbon Nitride Material. Z. Anorg. Allg. Chem. 2017 **DOI**:10.1002/zaac.201700268 [

Abstract

In recent years there has been significant interest in, and research into, carbon nitride materials for use in applications such as photocatalysis. The most commonly described C/N materials are referred to as graphitic carbon nitride (gCN), though due to the layered amorphous nature structural characterisation is difficult. Polytriazine imide (PTI) is a crystalline layered carbon nitride that is less explored within the literature compared to gCN due to its more difficult synthetic procedure. In this thesis the synthesis, characterisation, intercalation chemistry and exfoliation of PTI is explored. The synthesis of a related material, triazine based graphitic carbon nitride (TGCN) is explored and the product characterised in detail.

PTI refers to the carbon, nitrogen and hydrogen framework ($C_6N_9H_3$) within which different ionic intercalants can be accommodated; then give rise to several different crystalline materials with the same underlying carbon nitride backbone. The structure of these crystalline, layered PTI was synthesised by reversibly removing and replacing the intercalated ions without affecting the carbon nitride structure. The structures of these new materials was investigated and how changing the intercalant can be used to tune the structures and properties. This methodology may facilitate the fine-tuning and optimisation of carbon nitrides for a number of applications.

I have also explored the exfoliation of the layered PTI materials. A number of methods have been used including intercalation and ultrasonication. Remarkably, however I found that the PTI gently, and even spontaneously dissolves to form solutions in highly polar organic solvents and even in water. This process takes place without the need for mechanical mixing, sonication or centrifugation. The resultant separated nanosheets solutions are characterised indepth. Few layer stacks of undamaged crystallites are observed. The photoluminescence of the nanosheets have been found to depend on the number of stacked layers, presenting exciting opportunities for optoelectronic devices.

Chapter 1 - Introduction

1.1 Technological background

1.1.1 The indispensability of semiconductors

Semiconductors have become the foundation of modern life. They are fundamental components of transistors, large numbers of which are integrated into microchips. From household appliances to social media the rapid and continuous increase in the effective power of computing has become a driving force for advancement of technology, for social change and economic growth.[1] As a society we have become not only reliant on this technology, but continually seek to develop and improve it. However this requires investigating new materials with improved physical properties with which the technologies of the future will be based.

It is not only computing power that is reliant on semiconductors, many of the problems facing the world at the moment; energy storage, reliance on fossil fuels and rare metal scarcity, could potentially all be mitigated by developing new semiconductor technologies. Photocatalysts use the energy gained by promotion of electrons across a semiconductor's bandgap to drive chemical reactions.[2-5] These photocatalytic materials been proposed to offer selective removal of waste products,[6-8] removal of CO_2 from the atmosphere,[9-12] and potentially the genesis of hydrogen economy by high yield water splitting reactions.[5, 13-15] Photovoltaic materials work off a similar principle where electron and holes are separated and used to generate electrical energy. If achievable on a large scale with cheap materials could it entirely remove our dependence on fossil fuels.[16-19] Cheap, efficient and energy saving light emitting diodes (LEDs) are a superior alternative to incandescent light bulbs. One major limit to this ideal is having the right semiconductor; one with a suitable bandgap and transport properties. The perfect semiconductor material would also be free from expensive, scarce and potentially toxic metal materials.

The key to developing and improving these materials, and to be in a position to apply them to devices in the future is indepth characterisation. This would allow for controllable structural modification of a given material that could improve their effectiveness. A prime example of the potential of and the interest in forming of 2-D nanomaterials from 3-D bulk materials, is the exfoliation of graphite to form graphene.

1.1.2 Low dimensional materials

As far back as the 1930s the questions of whether a strictly 2D crystal would be stable has been a centre of active speculation from theoreticians, notably Landau[20, 21] and

Peierls.[22, 23] They showed that in the standard harmonic approximation they are not stable due to thermal fluctuations. Although thin layers of carbonaceous materials with thicknesses in the range of 3 – 6 Å had been reported before 2004,[24, 25] it was Novoselov *et al.* who first isolated single layer graphene.[26] In their paper they reported on the observed electric field effect and produced the first graphene based metallic field-effect transistors (FET).[27] [28] Graphene itself is a 2-dimensional crystalline sheet composed of fused benzene rings, a single atomically thin layer of crystalline bulk graphite.[27] It was for this work and the subsequence interest in the unusual properties of graphene such as ballistic electron transport and it being a zero-band gap semiconductor that Novoselov and Geim shared the 2010 Nobel prize in physics. [27, 29] Among the remarkable properties of graphene are its high surface area per unit weight (2200 m^2/g) and very high charge carrier mobility (15,000 cm^2 V^{-1} S^{-1}).[26, 30] Apart from FET[27] graphene has been proposed as a component in hydrogen storage devices,[31] and battery technologies[32] to name just a few.

Since graphene's rise to fame low dimensional materials have represented a strongly growing area of materials science. Other layered materials have also shown a substantial change in properties when exfoliated into nanosheets. For example MoS_2 in the bulk state is a semiconductor with an indirect band gap of 1.2 eV.[33] After exfoliation, a single layer has a direct band gap of 1.8 eV.[34, 35] This has been utilised in sensing applications[34] and as transistors.[35] Graphene and MoS_2 are just two examples of a wide range of layered nanomaterials. Given there are hundreds of layered materials known it is clear that 2D chemistry and physics represents a vast area of scientific discovery.

1.1.3 Carbon nitrides

Amongst potential 2D materials, carbon nitrides are emerging as an exciting family of semiconductor. They have received significant interest in recent years because of their potential for photocatalytic and water splitting applications.[36, 37] This potential derives from carbon nitrides being semiconductors with band gaps ranging between 1.7 and 2.7 eV. [38-41] They are composed of carbon, nitrogen, hydrogen. They can be synthesised from cheap starting materials and are metal free, which is highly desirable for many applications.[37] They are defined by a high nitrogen to carbon ratio (N to C ratio >1). Many reports have investigated exfoliation of these materials,[42-45] though these have typically focussed on amorphous varieties of carbon nitrides, while the crystalline, layered versions have received less attention. Further development of these materials requires more in-depth structural characterisation in relation to their properties as to optimise them for various applications. This thesis will focus on the synthesis and development of two classes of crystalline carbon nitrides.

1.2 Classification of carbon nitrides

1.2.1 Typical terminology of carbon nitrides

The family of carbon nitrides that are dealt with in this thesis are typically synthesised via the thermolysis of nitrogen rich CNH containing precursors such as melamine and DCDA (Figure 1.3a,b) . The $–NH_2$/–NH– terminations of these monomers react together to form larger chains or sheets linked by –NH–/$N(-C)_3$ releasing NH_3 during the condensation reaction.[46] These materials are all related by their composition of carbon, nitrogen and hydrogen, and can be represented on ternary diagram (Figure 1.1). As the CNH precursors react they release NH_3, moving them along the tie-line shown in red until they formed more condensed phases such as melon or polytriazine imide. The theoretical endpoint for this condensation reaction would be a material containing only carbon and nitrogen, with the stoichiometry C_3N_4.

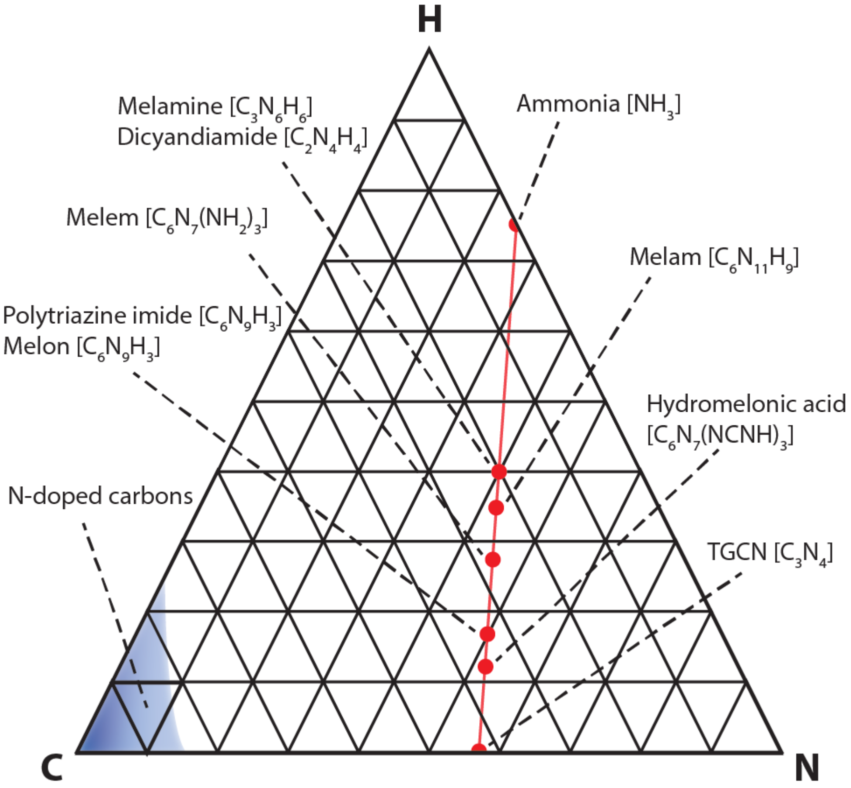
H
Melamine [$C_3N_6H_6$]
Dicyandiamide [$C_2N_4H_4$]
Ammonia [NH_3]
Melem [$C_6N_7(NH_2)_3$]
Melam [$C_6N_{11}H_9$]
Polytriazine imide [$C_6N_9H_3$]
Melon [$C_6N_9H_3$]
Hydromelonic acid
[$C_6N_7(NCNH)_3$]
N-doped carbons
TGCN [C_3N_4]
C
N

Figure 1.1 Ternary diagram showing the C/N/H compositions of various carbon nitride structures plotted with a red tie-line indicating the path a material will take if it losses only NH_3 components, also indicated is N-doped carbons.

There is a great deal of confusion in the literature as to the definition of carbon nitride materials. I will follow the lead of Miller *et al.*[47] in trying to rigorously define various types of carbon nitrides to assist in future discussions. It has become commonplace to describe materials formed through the thermolysis of precursors such as melamine/dicyandiamide(DCDA)/urea as graphitic carbon nitrides, abbreviated as g-C_3N_4 or gCN.[48-50] However the name 'g-C_3N_4' suggests incorrectly that these materials have that strict stoichiometry and are layered. While this could be considered just a naming convention, these reports are accompanied by diagrams showing pristine C_3N_4 layers with no evidence to support this. Furthermore a quick look at the IR spectra of the majority of these reports with C_3N_4 or g-C_3N_4 in the title clearly shows the presence of significant numbers of N-H bonds, which is mutually exclusive with a true C_3N_4 structure.

Here we separate carbon nitrides into three main groups as shown in Figure 1.2. These include C_xN_y materials, $C_xN_yH_z$ materials and N-doped carbon, all of which will be explored in more detail.

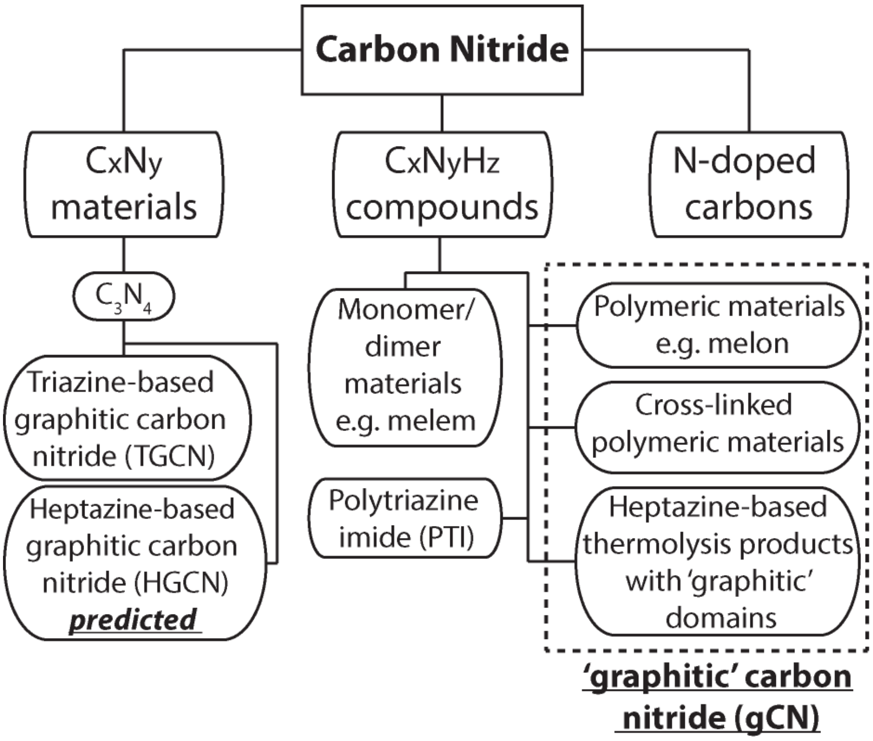
Carbon Nitride
CxNy materials
CxNyHz compounds
N-doped carbons
C3N4
Triazine-based graphitic carbon nitride (TGCN)
Heptazine-based graphitic carbon nitride (HGCN) predicted
Monomer/dimer materials e.g. melem
Polytriazine imide (PTI)
Polymeric materials e.g. melon
Cross-linked polymeric materials
Heptazine-based thermolysis products with 'graphitic' domains
'graphitic' carbon nitride (gCN)

Figure 1.2. Diagram showing the relationship of different carbon nitride materials and how they are commonly referred to in the literature.

1.2.2 C_xN_y materials

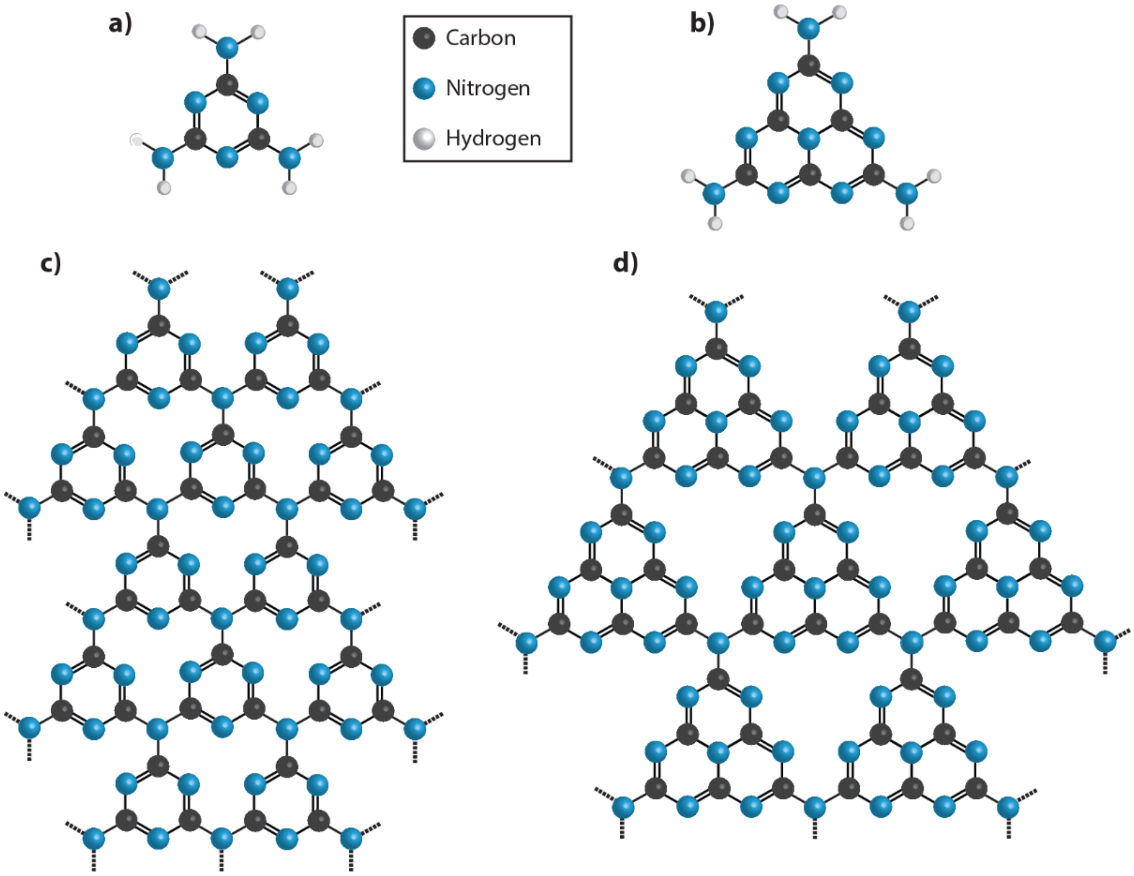

Figure 1.3. Molecular structures of idealised carbon nitride materials. a) Melamine. b) Melem. c) Triazine based C_3N_4. d) Heptazine based g-C_3N_4.

C_xN_y materials (Figure 1.3c,d) i.e. containing only carbon and nitrogen, have only been reported and shown to be as such by Kouvetakis *et al.*[51, 52] and possibly in a paper by Algara-Siller *et al.*[41] Layered C_3N_4 can theoretically be formed from either heptazine (C_6N_7) (Figure 1.3d) or triazine (C_3N_3) (Figure 1.3c) units. Melem (Figure 1.2b) is the basic heptazine molecule and melamine (Figure 1.2a) is the basic triazine molecule, both are terminated by N(-H)$_2$ bonds. While the heptazine g-C_3N_4 structure has been predicted to be the most stable only the triazine g-C_3N_4 structure has been shown experimentally.*[46, 51-53]*

1.2.3 $C_xN_yH_z$ materials

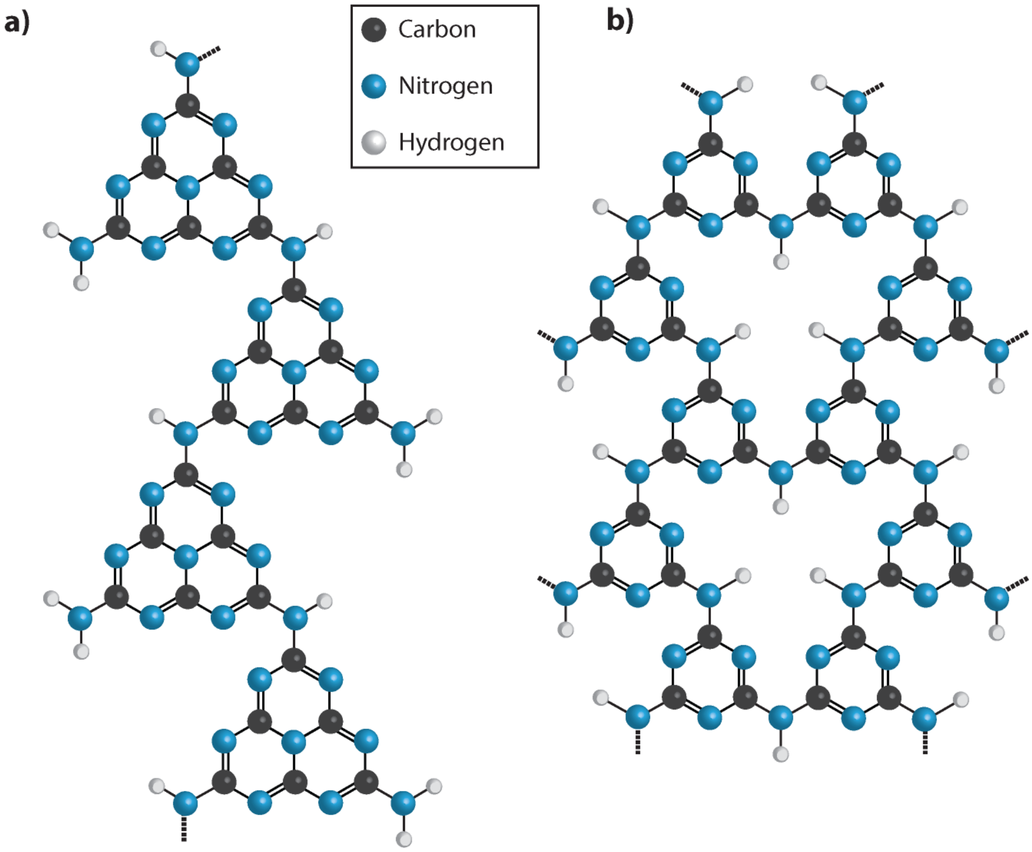

Figure 1.4. Molecular structure of several hydrogen containing carbon nitride materials. a) Melon. b) Polytriazine imide.

$C_xN_yH_z$ materials (Figure 1.4) contain a significant contribution of hydrogen within the structure. This is as a result of incomplete condensation of the CNH containing precursors resulting in a hydrogen terminations throughout the structure. They are typically referred to as layered though this is only true for some of these materials such as polytriazine imides (PTI) (Figure 1.4b).[54-56] PTI is the best understood layered $C_xN_yH_z$ substructure mostly due to its crystalline nature, this makes characterisation significantly easier compared to the disordered carbon nitride materials. However the most common $C_xN_yH_z$ material reported in the literature is referred to as 'g-C_3N_4' or 'gCN'. Which is formed through thermolysis of CNH containing precursors and has a varied stoichiometry. [57, 58] In 2007 Lotsch *et al.*[59] a range of characterization techniques investigated the structure of melon (Figure 1.4a), finding a structure that consisted of polymeric chains of melem units crosslinked by hydrogen bonding in a 'planar' fashion. They also note the melon is often reported as 'g-C_3N_4' in the literature. In 2015 Fina *et al.*[60] through an extensive x-ray and neutron diffraction study of 'g-C_3N_4' materials found that they had near identical structure to that reported for melon with slightly small differences in inter-chain distances. From this they suggest that the carbon nitrides synthesized through the condensation of CNH containing precursors such as melamine were in fact polymeric melonic chains not layered C_3N_4 materials. It is clear then what is typically referred to as 'g-C_3N_4' or gCN is structurally similar to melon (Figure 1.4a) not a true layered C_3N_4 material (Figure 1.3d) and therefore is misleading and incorrect. Melon has a significant hydrogen content and is non-crystalline. One aspect that is not clear is if there is any degree of C-N bonding crosslinking between melon chains, I therefore define gCN as a $C_xN_yH_z$ material including melon and crosslinked polymeric carbon nitride materials including those with small more condensed domains.

1.2.4 N-doped carbons

In addition to the above, materials formed by treatment of graphite or graphene with NH_3 or N_2 plasma are sometimes referred to carbon nitrides.[30] These N-doped carbons (Figure 1.2) typically have a small nitrogen content as shown in Figure 1.1 (around 0.1-5 wt%) although some examples of higher nitrogen doping up to 20 wt% nitrogen has been reported.[61-63] These nitrogen doped carbons are still conductive sheets of carbon with a small nitrogen content introduced to create 'activated regions' e.g. as a position for a metal particle to bind or to act as reaction centres for oxygen reduction reactions (ORR).[30, 64] Due to the nature of the doping the nitrogen environments and locations are not controlled and hence a variety of nitrogen environments are found within these materials.[30]

1.3 Potential applications of carbon nitride materials

On Web of Science there are over 18,000 papers with carbon nitride in the title or abstract. A significant number of these papers describe potential applications of these materials. However many of those reporting on gCN don't include significant structural characterisation due to its amorphous nature. The next section will look at the reported applications of both gCN and PTI.

1.3.1 Current applications of gCN

Thomas *et al.*[37] reviewed the use of gCN and, in particular, a mesoporous carbon nitride material as a metal free catalyst for Friedel-Crafts alkylation of benzene. They reported that these wide band gap semiconductors offered improved catalytic performance for cyclotrimerisations reactions.[65] This is especially interesting as carbon nitride are resistant harsh chemical environments. In addition to catalytic applications, the stability of carbon nitrides and its band gap of 2.7 eV makes it a potential material for water splitting.[66, 67] A multitude of papers has investigated its potential use for water splitting by itself or as part of a heterojunction[3, 43, 68-74], typically it has been paired with platinum or various metal oxides TiO_2,[75-89] AgCl,[90-92] WO_3[93-98] to name a few. Recently Liu *et al.*[71] have successfully shown a two stage water splitting reaction with gCN mixed with carbon quantum dots. This report is particularly interesting as no metal catalyst is required for this reaction making it potentially more commercially viable and environmentally sound. In addition gCN has been shown to be an improvement on carbon materials as catalyst support in a direct methanol fuel cell[99, 100]. Carbon nitride synthesised with a high carbon containing precursors has also been used in photocatalytic water splitting[36, 101, 102] and in biological applications due to its bio-compatibility[45], for example as a label for cell membranes, as a fluorescence sensor for DNA[103] and was found to photocatalytically break down the bio-marker Rhodamine B.[104]

1.3.2 Potential applications of PTI

PTI materials have been explored for similar applications as gCN, however due to the more difficult synthetic procedure they have been less widely explored. Ham *et al.*[105] and H. Zhang *et al.*[106] reported that PTI.LiCl showed the potential for hydrogen evolution. Bhunia *et al.*[107, 108] and Schwinghammer *et al.*[109] published several papers in which carbon doping of the nitrogen sites in PTI.LiCl was explored for hydrogen evolution reactions and appeared to be more effective than non-doped PTI.LiCl. Lee *et al.*[110] reported on the formation of a ‘crystalline PTI’ or ‘cPTI’, however there is some concern with the validity of defining this material as PTI given the reported XRD patterns and TEM images. Even so, the synthetic products were shown to be useful as counter electrodes in dye sensitised solar cells. Zhang *et al.*[111] reported using PTI as photocatalyst for the selective oxidation of cyclohexane. Wang *et al.*[112] found using DFT calculations that single layer PTI could act as a membrane that filters CO_2 from a CO_2/N_2 mix. It was reported that a single PTI layer with no intercalated ions would act as a gateway selectively allowing N_2 through the sheet.

1.4 Exfoliation of layered materials

As briefly discussed in Section 1.1.2 taking a material, and isolating a low dimensional analogue can potentially allow access to enhanced properties and higher surface area. If stable in solution then this provides a scalable processing route. As such, exfoliation is a key technique in the toolbox of chemists and physicists, however it is often achieved through the use of sonication or highly oxidising environments which can damage the nanomaterial leading to changes in properties and structure.[113-115]

1.4.1 General exfoliation methods

The formation of nanosheets requires the exfoliation of bulk materials such as graphite. To separate these 3-D materials into 2-D layers exfoliation techniques have been described that fall into several categories: mechanical exfoliation,[27, 41] chemical exfoliation,[113, 116, 117] intercalation[118, 119] and solvent specific exfoliation.[120, 121]

The classic mechanical exfoliation is the ‘Scotch tape’ exfoliation where layers are peeled off of the surface of a layered material using adhesive tape then exposed to acetone to remove the tape. Using this technique nanosheets down to single layer thicknesses have been reported.[27, 41]

Chemical exfoliation involves the introduction of functional groups onto a layered material, this functionality allows the material to dissolve and exfoliate in an appropriate solvents.[113, 116, 117] One of the most well-known examples is Hummer’s method for making graphene oxide from graphite.**[122]** These exfoliation techniques typically involve prolonged periods of reflux in acid or sonication which can damage the material. Chemical exfoliation is known to introduce defects into the material which can inhibit performance if pristine nanosheets are required.[117]

The intercalation of molecules and ions between the layers of a material weakens the inter-layer forces, allowing them to exfoliate in a suitable solvent.[123] Alternately the introduction of intercalants can transfer charge to the layers so that when they are exposed to a suitable solvent they ‘spontaneously exfoliate’.[118, 119] Some charged nanomaterials are very reactive and can be air sensitive which can complicate the handling of these materials compared to more conventional techniques.

Ultrasonication also provides a powerful method of exfoliation. For example Coleman *et al.*[124, 125] have reported that sonicating nanotubes or layered materials such as MoS_2 or boron nitride in dipolar solvents such as N-methyl-2-pyrrolidone (NMP) or Iso-propyl alcohol (IPA) can result in their exfoliation. They reported that the mass of material suspended depended on the solvent properties such as surface tension. By matching the nanomaterial with a particular solvent nanosheets can be stabilised in solution. However the reported concentrations of solutions achieved in this method are typically quite low.

Liquid exfoliation techniques yields nanosheet solutions and suspensions. These can be easily used for the assembly of devices or composite materials.[124, 126] However it is desirable to form true solutions of nanomaterials where the layers are stable in solution and that will not form sediment, as opposed to suspensions which tend to ‘crash out’ of solution over time. To form ‘true’ solutions, the nanomaterials must be stabilised in solution by favourable interaction with the solvent.

Chapter 2 – Methods

2.1 Characterisation techniques

2.1.1 Scanning electron microscopy (SEM)

Field emission scanning electron microscope (FE-SEM) images were taken using a JEOL JSM-6700F system, the sample were placed on conductive carbon tape and gold coated before imaging.

2.1.2 Transmission electron microscopy (TEM)

TEM images were taken using a JEOL JEM-2100 TEM (accelerating voltage: 200 kV) and HRTEM images were collected using a FEI Titan 60–300 (accelerating voltage: 80 kV). Sample from aqueous solutions were prepared by dropping the solution onto holey carbon TEM grids (Cu 300 mesh, Elektron technology UK ltd) which were placed in a drying furnace overnight (80 °C, Gallenkamp hot box oven). Samples from all other solutions were dropped on holey carbon TEM grids (Cu 300 mesh, Elektron technology UK ltd) which were then heated to 80°C on a hot plate for several minutes to evaporate the majority of the solvent and then placed under reduced pressure (10^{-6} mbar) for 12 hours for further drying. It should be noted that the PTI nanosheets quickly experienced electron beam induced damage on both high and low resolution TEM. Filtered images were produced by application of Gaussian kernel filter methods with sigma=1 and typical background subtraction algorithms. HRTEM image simulations were performed with Jems software by collaborator at the École polytechnique fédérale de Lausanne; Dr Vasiliki Tileli. A histogram of the bulk PTI·LiBr crystallite diameter (from two parallel edges across the hexagonal plane) was created by manual measurement from TEM images of >370 individual crystallites.

TEM studies of TGCN samples were prepared by sonication in methanol followed by dropping the resultant suspension onto 300 mesh gold TEM grids with a holey carbon film were carried out using a JEOL JEM-2100 instrument (accelerating voltage: 200 kV).

2.1.3 Microbeam FTIR

Fourier transformed infra-red (FTIR) spectra samples were taken on a Bruker IRscope in transmittance mode. Attenuated total reflective FTIR (ATR-FTIR) spectra were taken on a Bruker Alfa FTIR spectrometer.

2.1.4 Elemental analysis

Samples were sent to the elemental analysis service at the University of Sheffield for CNH elemental analysis. Elemental analysis was carried out at the using a Vario MICRO cube elemental analyzer (Elementar). TGA was run on a Netszch TGA instrument. The material was loaded into an alumina crucible (~5 mg), which was heated under He at 5 ˚C/min from room temperature to 750˚C.

2.1.5 X-ray photoelectric spectroscopy (XPS)

X-ray photoelectron spectroscopy (XPS) samples were then run on a K-Alpha XPS system. Samples were mounted on conductive carbon tape and a charge compensating flood-gun was applied to avoid charging effects. Experiments were carried out both on as-prepared samples and following erosion of potential contaminant species from the surface layer using an Ar^+ beam.

2.1.6 UV-Vis

Ultraviolet-visible spectroscopy (UV-vis) of liquid samples were run on a Shimadzu UV-2401 PC in transmission mode, the solutions were added to quartz cuvettes which were background subtracted. UV-vis of solid samples were measured by optical diffuse-reflectance on a PerkinElmer Fourier transform lambda 950 UV-vis spectrophotometer equipped with an integrating sphere between 200 – 800 nm with a 1 nm step size.

2.1.7 Raman Microscopy

Unpolarised microbeam Raman spectra were taken using a Renishaw InVia spectrometer using a 325 nm (He-Cd), a 514.5 nm (Ar^+) and a 785 nm (Diode laser) excitation wavelengths. Samples were deposited onto CaF_2 slide which was placed onto a common glass slide.

2.1.8 X-ray diffraction (XRD)

PXRD patterns were taken using a Stoe Stad-P (Cu) diffractometer using $K\alpha1$ radiation source. The sample were loaded into 0.5 mm glass capillary tubes (capillary tube supplies ltd), a background of the capillary tubes was taken and removed from each data set.

Individual TGCN flakes mounted with their largest dimension normal to the X-ray beam in a Stoe Stadip diffractometer were rotated by +/-5° about the incident beam axis to introduce orientation averaging into the pattern. Additional patterns were also obtained using Cu K_α radiation with a Philips X-Pert diffractometer in reflection geometry with the scattering vector aligned parallel to the c-axis of the crystallites.

2.1.9 Zeta potential and DLS

Zeta potential and DLS measurements were run at room temperature on a Zetasizer Nano ZS ZEN3600 and a Malvern universal dip cell ZEN1002.

2.1.10 Thermogravimetric analysis (TGA)

TGA was run on a Perkin Elmer & Hiden Pyris 1 TGA-MS. For liquid samples ~20 ml of solutions was loaded into a platinum pan, which was heated under N2 at 2 ˚C/min from room temperature to 950˚C. For solid samples ~20 mg of powder was loaded into a platinum pan, which was heated under N2 at 2 ˚C/min from room temperature to 950˚C.

2.1.11 Fluorescence

Photoluminescence (PL) and photoluminescence excitation (PLE) spectra were collected using a Horiba Fluoromax spectrophotometer and a 10 mm quartz cuvette. The excitation wavelength was varied between 260 and 330 nm, all fluorescence measurements were run by collaborators in Imperial College London; Dr Andrew Telford and Prof Jenny Nelson.

2.2 High speed atomic force microscopy (AFM)

HS-AFM images were acquired using a custom-built contact-mode HS-AFM with a Laser Doppler Vibrometer (LDV) (Polytec OFV-534 with DD900 Displacement Decoder), allowing direct measurement of the topography sensed by the silicon nitride tip on the microcantilever (Bruker MSNL, tip radius 2 nm nominal, 12 nm max). This equipment was built, operated and samples ran by collaborators at Interface Analysis Centre, H. H. Wills Physics Laboratory, University of Bristol by Dr Loren Picco, Dr Oliver D.Payton and Mr Freddie Fussell-Pavier. Samples were prepared by dropping the DMF based solution onto freshly cleaved mica, which was heated to 80 °C on a hot plate in order to evaporate the majority of the solvent and then placed under reduced pressure (10^{-6} mbar) for 12 hours for further drying. Custom data analysis software (written in LabVIEW, National Instruments) was used to automatically detect the individual PTI nanosheets and calculate their respective heights. The analysis was refined from the method of automatic step height measurement reported previously[127] and increases the performance of the automatic nanosheet detection. Nanosheets were identified via edge detection and local thresholding algorithms in order to separate them from the mica substrate. Local flattening algorithms were then used on each isolated nanosheet to separate the Gaussian distributions of mica pixel heights from nanosheet pixel heights using the assumption that the mica and nanosheet are represented by parallel but offset planes.[128] The width of the nanosheet pixel height distribution were used to determine if the nanosheet was part of a larger aggregate. Any clusters or contaminated sheets were discarded. The height of isolated nanosheets was then calculated by subtracting the mean mica pixel height from the mean nanosheet pixel height.

2.3 Synthetic method

2.3.1 Swagelok setup

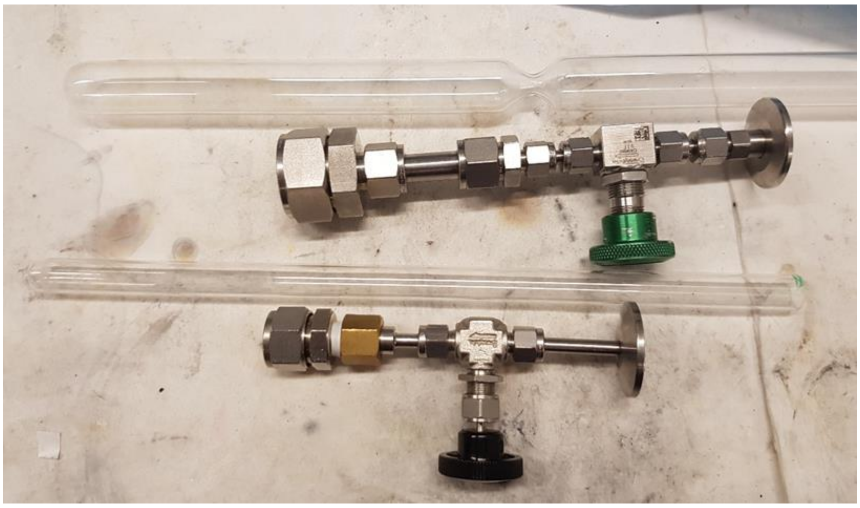

Figure 2.1. Picture showing the Swagelok setup and quartz ampoule for both the larger and smaller tubes

The larger and smaller tubes (Figure 2.1) were used depending on the desired mass of product, including their respective Swagelok setup (Large tubes: Robson Scientific, Φouter = 23 mm, Φinner = 20 mm, length = 15 cm, Small tube: Multilab, Φouter = 16 mm, Φinner = 13 mm, length = 15 cm). The ampoule are inserted into the O-ring adaptor and a single O ring is used to form a seal, care is taken not to overtighten the bolt. The Swagelok directly connects onto the turbo pump, with the valve closed the turbo pump is turned on, when it has reached 10^{-6} mbar the valve is very slowly opened as not to put too much air through the pump too quickly. The ampoule is left on the pump for an hour after the pressure has reached 10^{-6} mbar, the valve is then closed and the ampoule sealed. The larger ampoule were sealed using with a CH_4/O_2 flame by the in-house glassblowing service, while the smaller tubes were sealed with a CH_4/O_2 flame. Care is taken when sealing the tubes to form a strong seal, as ammonia gas pressure in the tubes can lead to them rupturing during the reaction.

Chapter 3 – Structural characterisation of polytriazine imide (PTI)

This chapter introduces the structural chemistry of the layered crystalline carbon nitride material polytriazine imide (PTI). It details the structure of the two main forms of PTI, PTI.LiBr and PTI.LiCl. These materials are characterised in detail to give a clear structural understanding as they are a central part of this thesis will be used in Chapter 4,5 and 6.

3.1 The structure of PTI

3.1.1 Initial syntheses of PTI materials

Zhang *et al.*[129] developed a high pressure synthesis of a carbon nitride material that would later be named PTI, for this, melamine and cyanuric chlorine were reacted together under high pressure and temperature (1 GPa, 500°C). The recovered material was found to be crystalline by XRD and electron diffraction and the reported stoichiometry was $C_6N_9H_5Cl$.[129] It was suggested that the chloride content was too high for unreacted cyanuric chloride, and that it was therefore intrinsic to the structure. The proposed structure (Figure 3.1b) was related to that suggested by Kouvetakis *et al.* (Figure 1.2e). The main difference is one of the triazine units has been removed, this results in hydrogens being attached the bridging amines to maintain the valency (Figure 3.1a). Like many carbon nitrides materials this structure has regular structural voids due to the valency difference between carbon and nitride. These larger voids are occupied by chloride anions which sit in the plane of 'graphitic' sheet (Figure 3.1b). The counter ion to this anion is a proton which was proposed to protonated the nitrogen lone pairs on one of the triazine rings (Figure 3.1b). This structure could be considered as the carbon nitride framework shown in Figure 3.1a, but with intercalated HCl. The layers are stacked in an AB motif where the chlorine atom resides in a void directly below and above the triazine ring of the adjacent layers.

The material was initially named using its idealised stoichiometry, $C_6N_9H_3HCl_x$. Later, this family of carbon nitrides was named 'polytriazine imide' (PTI) by Wirnhier *et al.*[56] due to the bridging amines between the triazine rings. PTI can be defined as any material with the carbon, nitrogen and hydrogen framework structure shown in figure 3.1a and is an overarching terms to describe all the materials with different intercalants. The individual intercalated PTI materials are named by the intercalants such as PTI.HCl for the material reported by Zhang *et al.*[129] (Figure 3.1b)

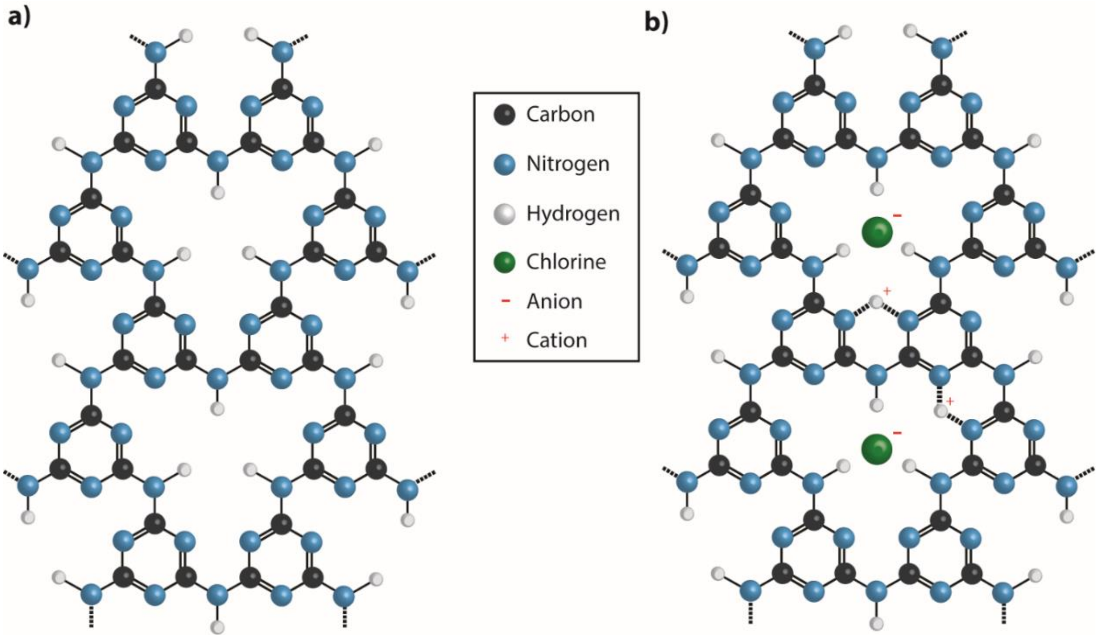

Figure 3.1. Diagrams of triazine based layered crystalline carbon nitrides. (a) The polytriazine imide ‘backbone’ structure. (b) The polytriazine imide structure reported by Zhang *et al.*[129] H^+ and Cl^- ions are intercalated into the material as shown above.

Later work on the topic by McMillan *et al.*[130] reproduced this synthesis, noting that the x-ray diffractograms showed both narrow and broad peaks. It was suggested that the structure is somewhat disordered causing broadening in some of the peaks. As was mentioned before, the proton from the PTI.HCl protonates one of the nitrogens on the triazine ring. However within the void occupied by the chloride ion there are 3 adjacent triazine rings, and hence six identical nitrogen positions that could be target of the protonation. Each would cause a slightly different position for the chloride anion. Since the H^+ ion can protonate any of these locations equally this was suggested to cause disorder within the layers. Raman studies of this material showed significant peak broadening, which would not be expected for a material that has shown to be crystalline.

In 2008 Bojdys *et al.*[131] attempted to make a fully condensed carbon nitride structure (Figure 1.2f) via a low pressure method. It was suggested that the kinetic of the reaction were limiting the synthesis of C_3N_4 materials stopping the reaction from proceeding to a fully condensed structure and that using a suitable solvent would solve this. They proposed the use of eutectic salt mixes, as most common solvents cannot withstand the temperatures required for the condensation reaction. Dicyandiamide (DCDA) was ground together with a eutectic mix of LiCl and KCl which acted as a solvent in the high temperature reaction (600˚C), this was then was heated under reduced pressure in a sealed environment. This process formed a crystalline product, however a residual lithium and chlorine content was noted in the material after washing which was not explained. The bulk XRD pattern showed a series of sharp peaks for a phase that could not be identified within this paper. TEM images reported prisms of 50 - 200 nm hexagonal crystallites stacked on top of each other, selected area electron diffraction (SAED) patterns of these showed a single crystalline phase. This paper also reports a series of FTIR spectra taken at different synthesis temperatures ranging from 380 - 600^{o}C, these clearly indicate that the crystalline carbon nitride material was formed only after heating at 500<T<600^{o}C. It was concluded, incorrectly, that this material was based on C_3N_4 layers of linked heptazine units (Figure 1.2f) as this was proposed as the most stable planar carbon nitride by Kroke *et al.*[46]

3.1.2 Identification of PTI.LiCl

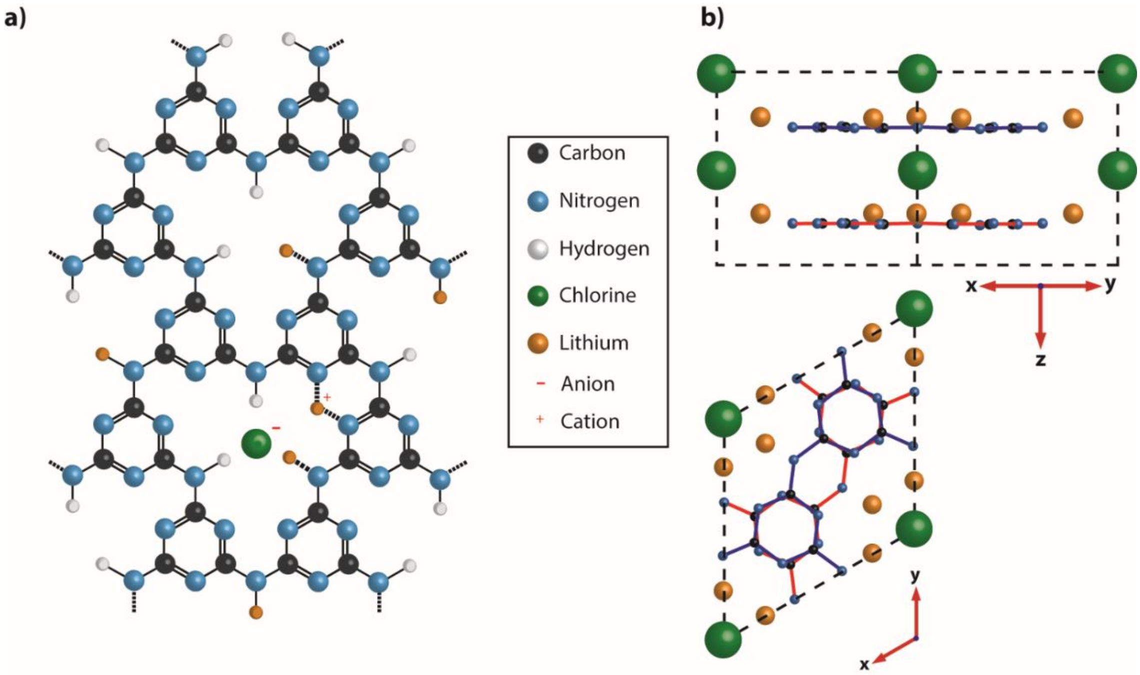

Figure 3.2. Diagram showing the structure of PTI.LiCl. a) A charge balanced structure of PTI.LiCl showing the position of the chloride anion and the assumed position of the lithium cations. The lithium can either act as the counter ion to the chloride or it can replace the hydrogen on the bridging imide. Typically each void would have one chlorine, two hydrogens and two lithiums. It is possible that some of the voids are unoccupied. b) A diagram of PTI.LiCl showing the stacking and the intercalated chlorine between the layers.

In 2011 Wirnhier *et al.*[56] repeated the molten salt crystalline carbon nitride synthesis procedure of Bojdys *et al.*[131] and characterised the product in more detail than previously. Importantly they concluded the structure to be based on triazine units rather than being one formed from heptazine units as was reported previously. Chlorine and lithium content was observed within the material, similar to the Zhang *et al.* structure, which could not be attributed to excess salt. This new material was termed PTI.LiCl. The structure of which is formed of triazine rings bridged with amine groups, (Figure 3.2) PTI.LiCl has intercalated lithium and chloride ions within and between the layers (Figure 3.1b). The chloride anion in the PTI.LiCl does not lie in the plane of the material as in the Zhang *et al.* structure but between the graphitic layers. The chloride now positions itself directly below and above the voids of the adjacent layers, with channels of anions forming across the length of the crystallite stack. The triazine rings are therefore also arranged directly above and below each other. This stacking motif is called AA' due to the identical structure layer to layer apart from the alternating position of the amine bridges (Figure 3.2b). The exact positions of lithium ions was not reported here due to its low sensitively from XRD. It was also noted that there was an excess of lithium over chloride and that there was less hydrogen than would be expected from the number of amine groups. To charge balance the structure it was suggested that some lithium acts as the counter ion to the chloride while the rest displaces some of the hydrogen on the bridging amines. Assuming the lithium first acts as the counter ion for the chloride they concluded from the elemental analysis that 1/3 of the amine bridges are bound to lithium instead of hydrogen.

3.1.3 Identification of PTI.LiBr

In 2013 Chong *et al.*[54] found that by changing the procedure of Bojdys *et al.*[131] and Wirnhier *et al.*[56] and using eutectic mix of LiBr/KBr they formed PTI.LiBr as determined by XRD and elemental analysis. It was reported that changing the halide in between the layers of the PTI had a noticeable effect on the gallery height of the material, which was observed via PXRD. The amount of halide per unit cell is noticeably lower for the PTI.LiBr compared to the PTI.LiCl. They also reported a partial ion exchange of the bromide for fluorides, by stirring the PTI.LiBr in ammonium fluoride solution. This resulted in a mix of bromine and fluorine ions within the material, the structure of which was not fully resolved.

3.1.4 Further reports on the structure of PTI materials

Apart from those reported by Chong *et al.*[54] and Wirnhier *et al.*[56] there have been several other reported syntheses of PTI materials.

In 2013 Ham *et al.*[105] reported a different PTI.LiCl synthesis method, in which DCDA and the chlorine salt are added to a crucible with a lid instead of a sealed glass ampoule. While they report a crystalline PXRD pattern they observed evidence for nitrile bonding in the IR spectra which does not feature in any reported spectra of PTI. The colour of the recovered powder was reported to be yellow, PTI.LiCl materials reported by Chong *et al.*[54] and Wirnhier *et al.*[56] were reported to be brown, while amorphous gCN is reported as yellow. This possibly indicates a structural difference between this reported PTI and those reported by Wirnhier *et al.*[56] and Chong *et al.*[54]

H. Zhang *et al.*[106] and Y. Zhang *et al.*[111] reported on open crucible reaction, though differed on the salt mixes used. H. Zhang *et al.* used a KCl and ZnCl mix, the PXRD of the resultant material did not match with previous reports of PTI and was significantly broader. Y.Zhang *et al.* used a combination of LiCl and KCl which appeared to have a crystalline PTI pattern though it was not directly compared against previous reports.

Fettkenhauer *et al.*[132] explored using a variety of eutectic salt mixes to synthesise PTI materials. Overall they found significant variation in crystallite morphology and structure due to different heating temperature, rates, times and precursors to salt ratio. They reported that a $ZnCl_2$ eutectic salt mix can be used as a molten salt successfully even in a closed crucible synthesis.

Bhunia *et al.*[107, 108] and Schwinghammer *et al.*[109] published several papers reporting on the synthesis of doped PTI.LiCl by reacting melamine and more carbon rich precursors. While the doped materials had improved water splitting performance the recovered material was found to be significantly less crystalline than Wirnhier *et al.*[56]

Lee *et al.*[110] reported on the formation of a ‘crystalline PTI’ or ‘cPTI’ through synthesis of melamine and cyanuric acid at 550˚C in an open container. While the XRD pattern does show sharp features that do broadly match with those expected for PTI.LiCl there are some large additional peaks that are not commented on in the paper. In addition TEM images of these ‘cPTI’ materials do not show the sharp hexagonal crystallites that are observed for these materials. It is not clear if the reported material is identical to that shown by Wirnhier *et al.*[56] and Chong *et al.*[54]

It is clear that several different synthetic methods have been reported for PTI. While some appear to be crystalline, most lack the in-depth structural understanding that Chong *et al.*[54] and Wirnhier *et al.*[56] have reported. It appears that the most crystalline PTI materials were observed by PXRD and TEM are by Bojdys’ *et al.*,[131] Wirnhier *et al.*[56] and Chong *et al.*[54] As such I will follow their reported syntheses.

3.2 Synthesis of PTI materials in this thesis

As this report focuses on PTI materials and they represent the key components to two chapters, it is necessary to fully understand these materials. To that end the rest of this chapter will be dedicated to characterisation and discussion of PTI.LiBr and PTI.LiCl materials.

3.2.1 Synthetic method for PTI.LiBr and PTI.LiCl

The synthesis of PTI.LiBr and PTI.LiCl share the same two stage synthesis, heating steps and washing procedures, they only differ by the salt ratio required to form the eutectic mixture. Lithium bromide (LiBr, Aldrich) and potassium bromide (KBr, Alfa Aesar) eutectic mixture (52:48 wt%, Tm=329 ˚C).[54] Lithium chloride (LiCl, Aldrich) and potassium chloride (KCl, Aldrich) eutectic mixture (45:55 wt%, Tm=353 ˚C).[131] DCDA (Sigma-Aldrich, 2g) was ground together thoroughly with the appropriate eutectic mixture (10g) in a glove box under N_2 atmosphere. All the precurors were heated to 150 ˚C under reduced pressure to remove absorbed water before being transferred to a glovebox, these are stored under a nitrogen atmosphere to stop water absorption. The reaction mixture was placed in an alumina crucible, moved from the glovebox into a tube furnace (Carbolite, MTF 12/38/250) where it was heated at 10 ˚C min^{-1} ramp rate to 400 ˚C for 6 h under N_2. After natural cooling to room temperature while still under nitrogen flow, the resultant material was quickly transferred back to the glovebox, where the hard salt block was ground down to a fine yellow powder. This precursor mix of eutectic salt and partially condensed carbon nitrides was loaded under nitrogen into a dried thick-walled quartz glass ampoule (~ 11g for larger tubes, ~3.5g for smaller tubes). (Large tubes: Robson Scientific, Φ_{outer} = 23 mm, Φ_{inner} = 20 mm, length = 15 cm, Small tube: Φ_{outer} = 16 mm, Φ_{inner} = 13 mm, length = 15 cm) This was attached to an airtight Swagelok valve system (Figure 2.1). The ampoule was then evacuated to 10^{-6} mbar using a turbo pump (Leybold vaccum systems, PT70G compact) without exposing the reagents to air. This ampoule was then sealed to form a static vacuum using an CH_4/O_2 flame, placed vertically in a chamber furnace (Carbolite, CWF11/13). The furnace was heated to 600 ˚C at 10 ˚C min^{-1} for 12 hours, before cooling to room temperature at ramp rate of 10 ˚C min^{-1}. The ampoule was carefully broken open, and the PTI.LiX was recovered by placing solidified salt block in a centrifuge tube then adding distilled water and shaking for 5 minutes. The tube is then centrifuged at 4500 rpm for 5 minutes, and the supernatant was then filtered off. This was repeated with distilled water for two more washes, followed by two ethanol (Millipore) washes. Any residual ethanol was removed by using a rotary evaporator (Buchi Rotavapour R-3, Vacuum pump V-700) to yield PTI as dark brown powder. XRD patterns and IR spectra were taken of each batch of the synthesised materials for comparison and to confirm the desired synthesis has taken place.

Synthesis of the material is possible using a one-step method, however the two-step method used here allows for release of a significant amount of the ammonia gas in the first step so more material can be made in one ampoule without risk of rupturing with no observable difference in the recovered material.

3.2.2 Deuterated PTI.LiCl

Deuterated DCDA was formed by placing DCDA (Sigma-Aldrich) in D_2O (Sigma Aldrich) for several days followed by recrystallization of the DCDA. This was repeated several times to form *d*-DCDA. The synthetic steps for PTI.LiCl above were repeated apart from replacing the DCDA with the *d*-DCDA and washing the resultant material with only D_2O to remove the residual salt.

3.3 Characterisation of PTI materials

3.3.1 PXRD and Occupancy of PTI materials

Wirnhier *et al.*[56] originally reported PTI.LiCl as having a hexagonal unit cell with a $P6_3cm$ space group, however this did not take account of the lithium positions. Using a combination of NMR, electron diffraction and XRD Mesch *et al.*[55] investigated the structure PTI.LiCl, in particular they focused on the position and arrangements of the intercalated lithium. They reported that each void in the PTI structure has exactly one chlorine, two hydrogens and two lithiums. This results in the structure change symmetry and going from space group $P6_3cm$ to $P2_12_12_1$, causing splitting in some of the XRD peaks.

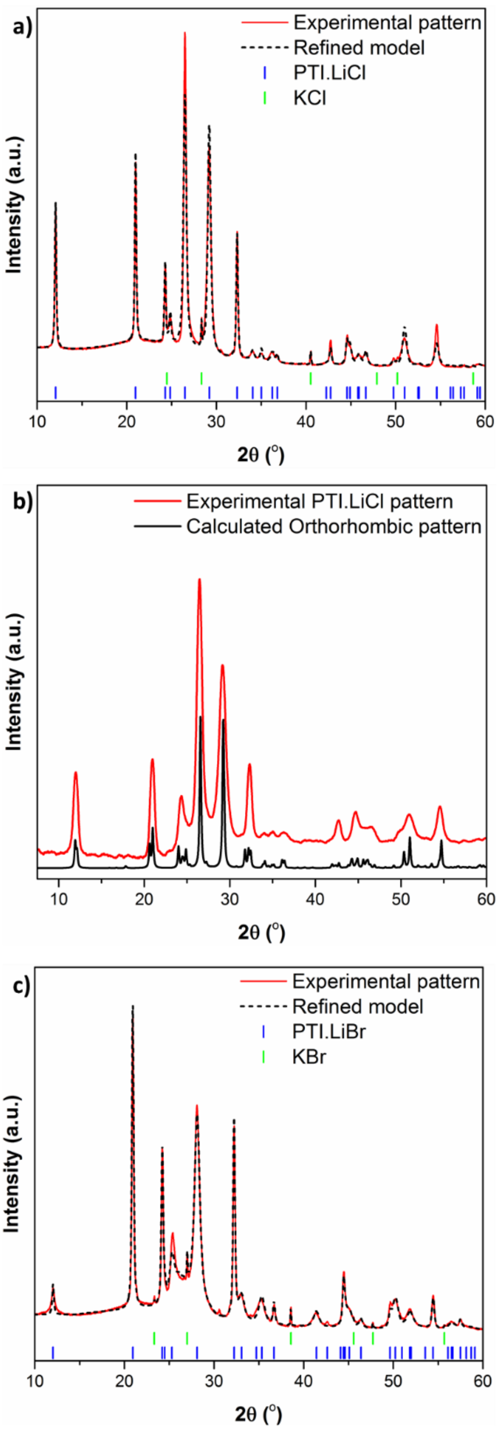

Figure 3.3. a) Experimental and refined PXRD patterns of PTI.LiCl with a hexagonal unit cell. b) Experimental and predicted PXRD patterns of PTI.LiCl with an orthorhombic unit cell. c) Experimental and refined PXRD patterns of PTI.LiBr with a hexagonal unit cell.

The XRD patterns of PTI.LiCl and PTI.LiBr (Figure 3.3) show a series of sharp peaks with many higher order features, indicative of a crystalline material. Predicted XRD patterns were calculated using the software package Mercury (Version 3.5.1[133, 134]) and the refinements were performmed using Rietica by collaborator Dr Jeremy Cockcroft. The hexagonal unit cell was proposed by Wirnhier *et al.*[56] and Chong *et al.*[54] for the PTI.LiCl and PTI.LiBr respectively. The peak positions and intensity of hexagonal PTI.LiCl and PTI.LiBr match well with the refined patterns, all peaks are either due to the expected structure or to residual KCl/KBr. There are no unexplained peaks and no discernible differences in refined peak positions compared to those reported in the literature. This suggests that the expected PTI.LiBr and PTI.LiCl structures have been formed.[56, 131] However an orthorhombic unit cell for PTI.LiCl was proposed by Mesch *et al.*[55] Figure 3.3 c shows the experimental PXRD patterns of PTI.LiCl compared against the calculated orthorhombic unit cell pattern. While the main peak positions seem to be in the right positions the loss of symmetry from the $P6_3cm$ to $P2_12_12_1$ and the larger size unit cell has caused the splitting of the *100*, *110* , *200* and *120* (as defined from the hexagonal unit cell). However I do not observe any indication for the splitting or see the additional peaks. When the refinement of the orthorhombic PTI·LiCl structure was performed, to compare with that of the hexagonal structure, the refined structure was found to be equivalent to the hexagonal model. From this I suggest that the higher order symmetry is a better fit for these materials and from now on I will being using the hexagonal for future analysis.

The gallery height (defined as the distance between two carbon nitride layers) can be extracted through analysis of the *002* peak.[135] This peak shifts significantly from 26.5° 2θ (3.36 Å) in the PTI.LiCl to 25.2° 2θ (3.52 Å) in the PTI.LiBr, this represents an increase in the interlayer spacing of 0.16 Å. The ionic radius of Cl^- is 1.81 Å,[136] for Br^- it is 1.96 Å,[136] a difference of 0.15 Å , very close to the difference in the interlayer spacing. The increase in gallery height is due to the size of the intercalated bromine compared to the chlorine as reported by Chong *et al.*[54] An additional observation is that compared to those with *hk*0 reflections ones with a non-zero *l* component have a higher degree of broadening for both PTI·LiCl and PTI·LiBr, this can be attributed to the layered structure of the materials.[135, 137]

The occupancy of the halide and lithium intercalants changes the relative intensity of the peaks, as the XRD patterns are dominated by the intercalated heavy halides arrangement. This also causes the relative intensities of the refined XRD patterns to not be an exact fit to the experimental data.[135, 137]

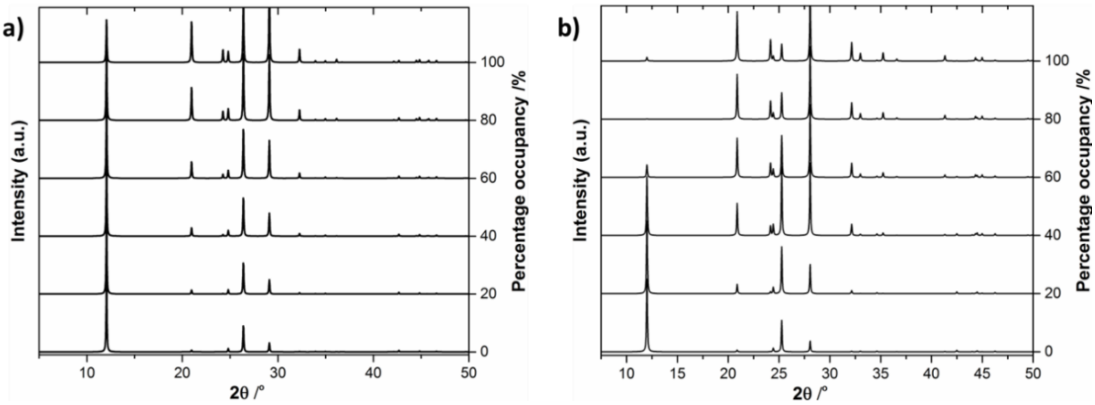

Figure 3.4. The calculated XRD pattern as a function of halide percentage occupancy of two types of PTI materials. (a) PTI.LiCl. (b) PTI.LiBr.

Figure 3.4 a,b shows the relative intensity of the peaks changes significantly as percentage occupancy (as defined as one halide per layer void or 2 per unit cell) decreases. In both the PTI.LiCl and PTI.LiBr the *100* and the *002* becomes the most intense peak as the occupancy drops to 0%, while the *110* and *102* are the most intense at 100% occupancy. Direct comparison between the calculated patterns at different percentage occupancies and the experimental data is difficult due to the asymmetric peak broadening. Comparing the relative intensity of the *110* and *102* peaks from the experimental pattern and comparing them against the calculated pattern suggests the occupancies above 40% for PTI.LiBr and above 60% for PTI.LiCl.

The elemental stoichiometry of different as-synthesised PTI materials have previously been reported as $C_{12}N_{17.5}H_{6.3}Cl_{1.5}Li_{3.2}$ and $C_{12}N_{17.8}H_{4.3}Br_{0.2}Li_{1.0}$,[54, 56] which equates to a halide occupancy of 10% Br and for 75% Cl. In our materials XPS analysis (Figure 3.6, 3.7), indicate halide occupancies of 48% for the PTI.LiBr and 95% for the PTI.LiCl. Bulk elemental analysis by combustion was also performed for these materials. The compositions were found to be $C_{12}H_{10.2}N_{16.6}Br_{1.3}$ and $C_{12}H_{7.7}N_{17.9}Cl_{1.7}$ for PTI.LiBr and PTI.LiCl respectively, indicating 65% bromine occupancy and 85% chlorine occupancy. These carbon, nitride, halide occupancy results match well with that found by XPS. I note that the hydrogen content found from combustions analysis was significantly higher than expected, it is unclear where this content originates. A washing procedure is used during the synthesis of PTI.LiX to remove the excess salt. Residual LiX/KX salts could explain these higher values, however only small contributions of these salts was found in XRD patterns. In Section 4.1 details how washing of the PTI materials can result in the removal of the intercalants. During the synthesis particular care was taken to not over wash the PTI.LiX. Given that our reported occupancies are in line with the calculated XRD patterns I suggest that the lower halide occupancy reported in the literature for PTI.LiBr is due to excessive washing of the PTI materials.

3.3.2 XPS of PTI materials

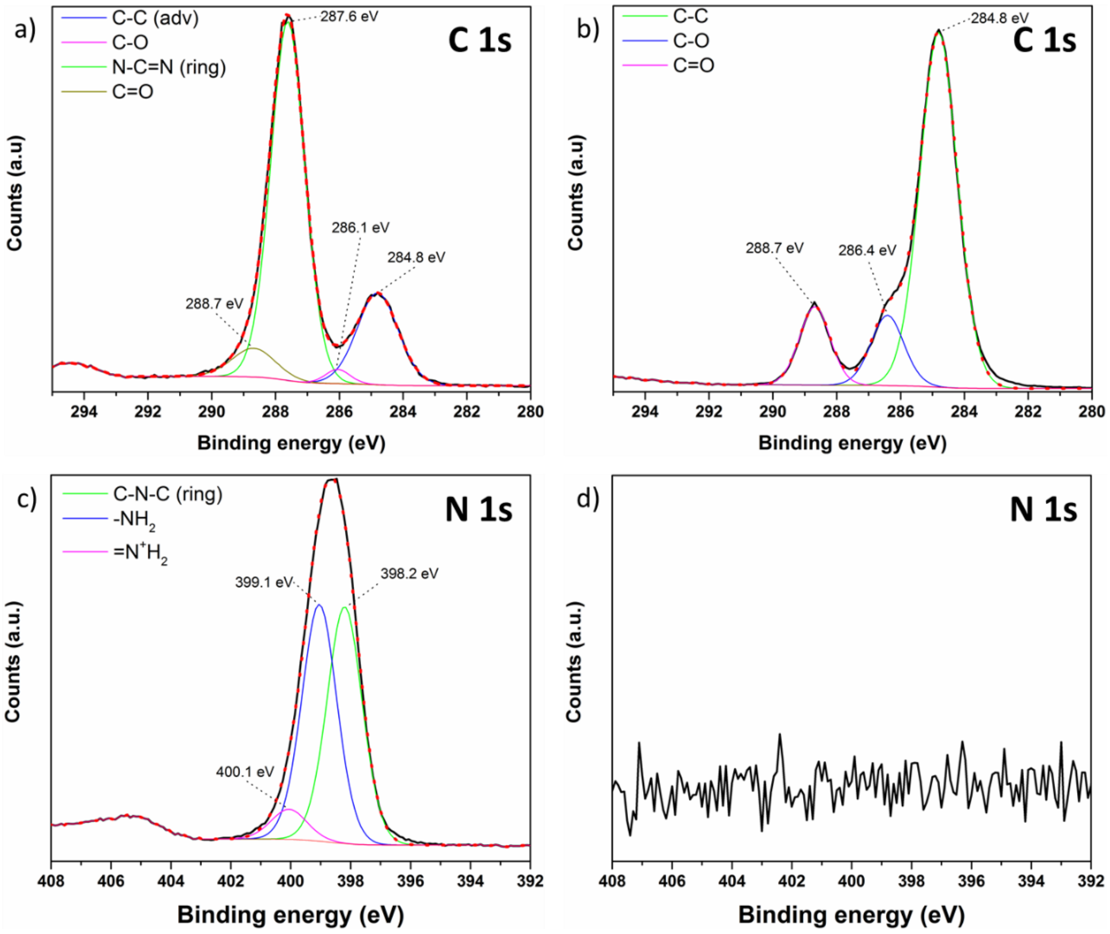

Figure 3.5. C1s and N1s XPS spectra of melamine and carbon tape. a) Carbon 1s spectrum of melamine. b) Carbon 1s spectrum of carbon tape. c) Nitrogen 1s spectrum of melamine. d) Nitrogen 1s spectrum of carbon tape.

XPS is a key characterisation technique for chemical analysis, for which the solid powder samples are typically mounted onto carbon tape. However the carbon tape has its own distinct XPS spectra and may appear in the sample spectra if the applied sample is not a consistent film. In addition, a C1s XPS spectrum typically has a peak from carbonaceous species referred to as ‘adventitious carbon’ that originate from sample handling and atmospheric exposure, though the intensity varies from sample to sample. Since our work focuses on carbon nitrides a good baseline is needed for these carbon signals. Binding energy values can vary from sample to sample due to the charging of semiconductor materials, however the adventitious carbon peak can be used as a guide as relative binding energies do not change as a result of charging. XPS spectra of carbon tape and melamine were taken to guide the understanding of the XPS of PTI materials (Figure 3.6). The C1s of the carbon tape (Figure 3.5b) is fitted with three environments, the first and largest is at 284.8 eV (C-C), the second at 285.4

eV (C-O) bonding and the last is at 288.7 eV (C=O). No nitrogen environments are observed (Figure 3.5d).[47]

Melamine ($C_3N_6H_6$) is the simplest triazine based carbon nitride material, the structure of which is well known, a single C_3N_3 triazine ring with NH_2 groups attached to the three carbons. The C1s spectra (Figure 3.5a) has a main feature at 287.6 eV which can be assigned to the in-ring carbon environments. There are several additional peaks, the 288.7 eV and 284.8 eV environments overlap with those seen in the carbon tape while third peak is slightly shifted from 286.4 eV to 286.1 eV. Given only the small shift and the same intensities I suggest that these additional peaks are due to the same environments seen in the spectra of carbon tape.

The N1s spectra (Figure 3.5c) shows a broad main feature which can be solved by one environment at 398.2 eV and one at 399.1 eV which are assigned to the in-ring nitrogen and the NH_2 environment respectively due to the relative binding energy. However an additional peak was found during fitting at 400.1 eV, this peak is unusually at an even higher binding than found for the NH_2 environment. Dementjev *et al*[138] have reported a peak at a similar position and intensity in the XPS spectra of melamine. This peak was suggested to be assigned to $=N^+H_2$ group in a resonant form of melamine similar to that suggested for aniline.[138]

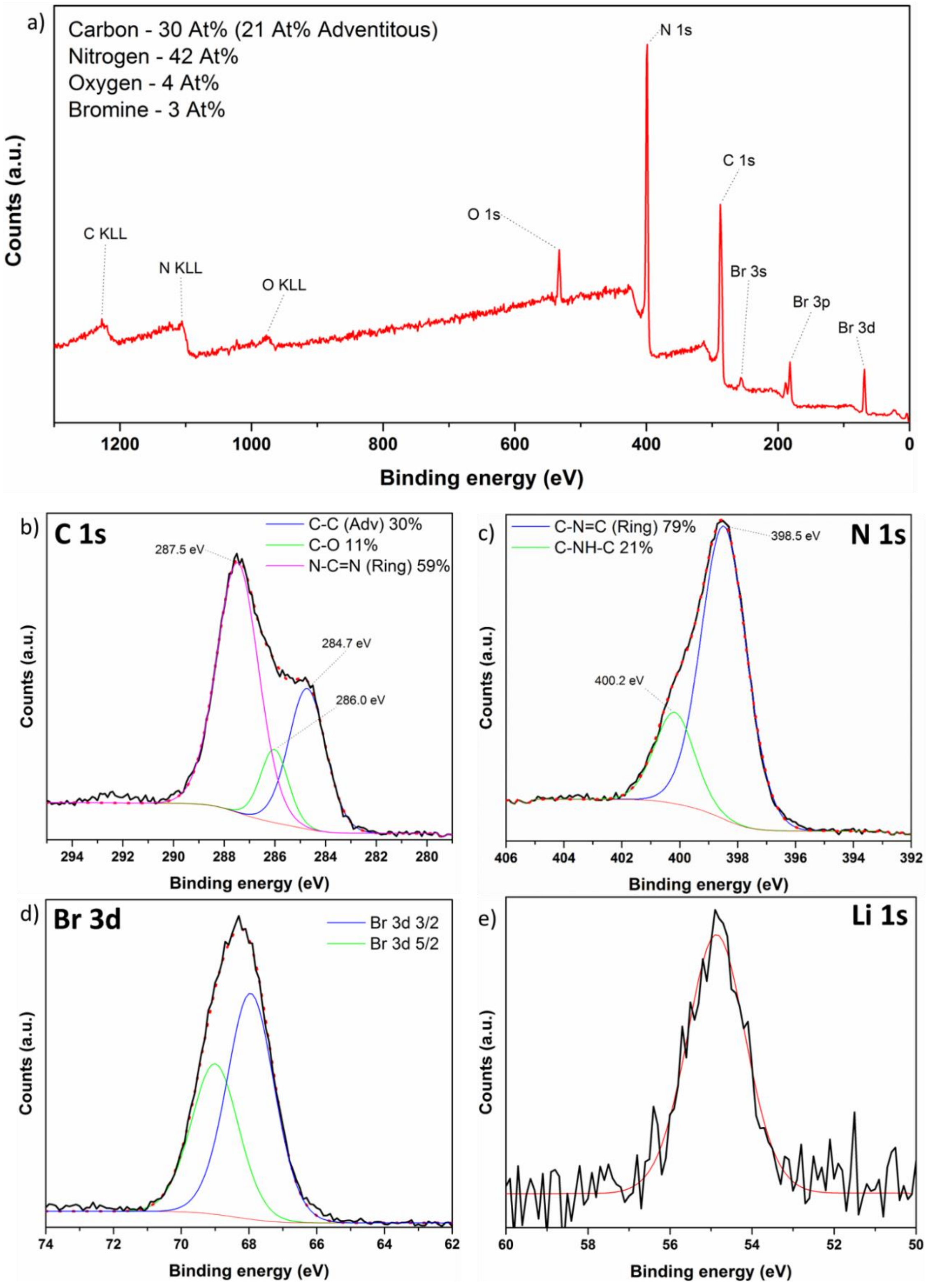

Figure 3.6. XPS Spectra of PTI.LiBr. (a) Survey spectrum. (b) Carbon 1s spectrum. (c) Nitrogen 1s spectrum. (d) Bromine 3d spectrum. (e) Lithium 1s spectrum.

The XPS Survey spectra of PTI.LiBr (Figure 3.6a) shows significant carbon, nitrogen, oxygen and bromine content. Atomic percentages of different elements are shown, the carbon content from the carbon nitride is shown while that just from the adventitious component is shown in the brackets. From this the calculated C:N ratio is 1 to 1.4, this is very close to the expected PTI stoichiometry 1 to 1.5.

All the spectra were fitted with Gaussian or Gaussian-Lorentzian (GL) functions. The C1s spectrum (Figure 3.6b) appears to have three distinct carbon environments. The peak at 284.7 eV appears in the same region as the main carbon tape peak and can be assigned to adventitious carbon. The largest peak at 287.5 eV is in the same position as carbon in the triazine ring in melamine so it can be assigned to in-ring C-N-C bonding.[41] The third environment at 286.0 eV is at a similar position to that observed for a related carbon nitride structure TGCN as reported by Algara-Siller *et al.*[41] as nitrile bonding, however no nitrile peaks are observed in the IR (Figure 3.8). This peak can also be assigned to C-O bonding as this region is associated with C-O as seen in the carbon tape. This may also suggest a degree of C-O bonding is occurring in the PTI.LiBr, most likely as a small degree of structural defects.

The N1s region also shows two distinct environments (Figure 3.6c), the peak at 398.5 eV is similar in position to that in melamine so is can be assigned to the nitrogen environment inside the triazine ring. The N1s of melamine (Figure 3.5) shows that higher binding energy peaks are associated with C-N(-H)$_2$ environments. Due to higher binding energy of the peak at 400.2 eV (Figure 3.6c) it can be assigned to the nitrogen bridging environments of the PTI. The area of the peak at 398.5 eV is ~3.6 times more than the peak at 400.2 eV this is close to the expected 3:1 ratio.

Two strong peaks with an area ratio of 2:3 are observed in the bromine 3d spectra (Figure 3.6d) these are due to one bromine environment, as expected to spin orbit splitting. XPS is less sensitive to light elements[139] hence the weak but distinct lithium peak (Figure 3.6e) however due to background noise it is not possible to identify the number of environments. Although I can clearly state that there is lithium within the structure an accurate atomic % calculation is difficult. The absence of any peak that could be associated with potassium is a clear indication that only lithium is intercalating into the structure, likely due to the size difference between the two cations.

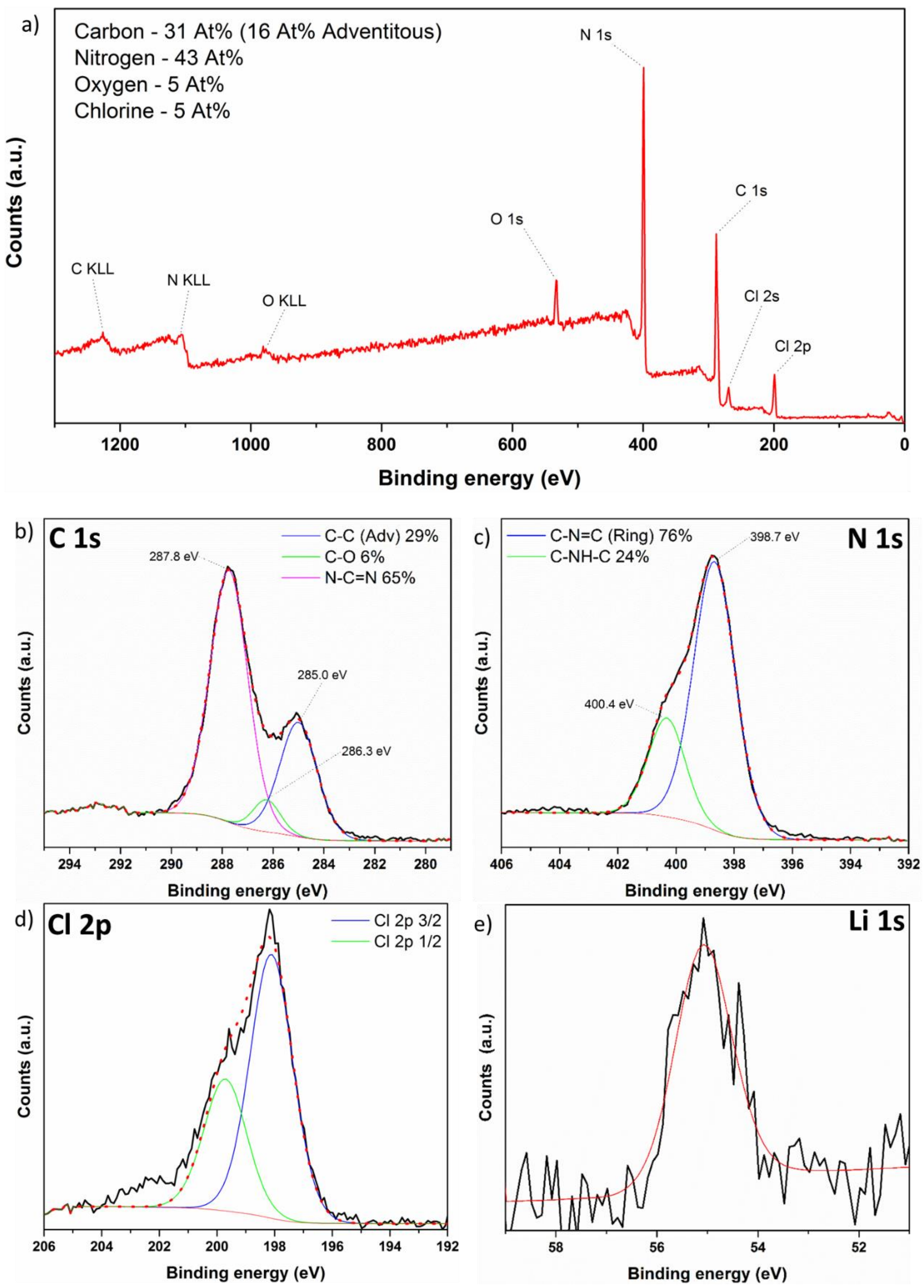

Figure 3.7. XPS Spectra of PTI.LiCl. (a) Survey spectrum. (b) Carbon 1s spectrum. (c) Nitrogen 1s spectrum. (d) Chlorine 2p spectrum. (e) Lithium 1s spectrum.

The survey spectra of PTI.LiCl (Figure 3.7a) is very similar to the PTI.LiBr (Figure 3.6a) apart from the change of halide from bromine to chlorine. Atomic percentages of different elements are shown, the carbon content from the carbon nitride is shown while that just from the adventitious component is shown in the brackets. The C to N ratio is calculated to be 1 to 1.4, this is again very close to the expected PTI stoichiometry and to that of the PTI.LiBr showing that the carbon nitride framework is identical in each PTI material.

The peak intensities and relative positions of the carbon 1s spectra of PTI.LiCl (Figure 3.7b) are very similar as those seen in PTI.LiBr, and since no change in the halide is expected to change the carbon environments the assignments are the same as in the PTI.LiBr. The peak at 285.0 eV can again be assigned to adventitious carbon. The largest peak at 287.8 eV can be assigned to the in-ring C-N-C bonding.[41] The third environment at 286.3 can again be assigned to C-O from defects in the structure. Given the identical C to N ratio and relative peak positions and areas it is clear that the carbon nitride backbone of PTI.LiCl and PTI.LiBr are near identical, showing changing the halide has little effect on the CN framework.

As with the PTI.LiBr the N1s region has two distinct environments (Figure 3.7c), the peak at 398.7 eV can be assigned to the nitrogen environment inside the triazine ring, while the peak at 400.4 eV can be assigned to the nitrogen bridging environments. The area of the peak at 398.7 eV is ~3.1 times more than the peak at 400.4 eV which as with the PTI.LiBr is close to the expected 3:1 ratio.

Two strong peaks with an area ratio of 1:2 are observed in the chlorine 2p spectra (Figure 3.7d) these are due to one chlorine environment. I again only observe a weak but distinct lithium peak. (Figure 3.7e)

A stoichiometry of $C_{12}N_{16.8}Br_{1.0}$ and $C_{12}N_{16.8}Cl_{1.9}$ was found for PTI.LiBr and PTI.LiCl respectively. A comparison of the halide content of PTI.LiBr (Figure 3.6d) and PTI.LiCl (Figure 3.7d) shows roughly twice there is twice as much chlorine in PTI.LiCl (95 %) as bromine in PTI.LiBr (50 %). It is not clear why there is so much variation in occupancy between the different halides. Wirnhier *et al.*[56] and Chong *et al.*[54] reported on the PTI.LiCl and PTI.LiBr respectively, also showing a lower halide occupancy in the bromine material.

3.3.3 Vibrational spectroscopy of PTI materials

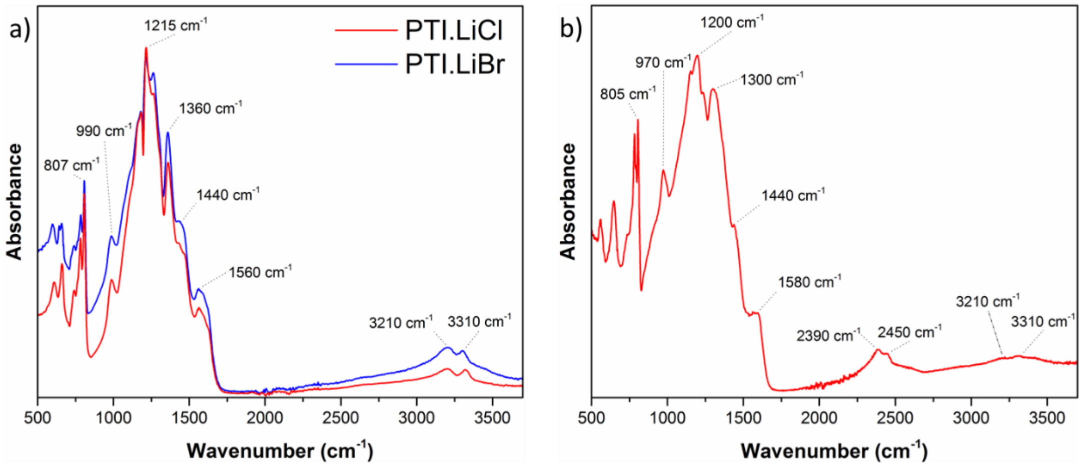

Figure 3.8. ATR FTIR spectra of PTI materials. a) Normalised IR spectra of PTI.LiCl and PTI.LiBr. b) Spectrum of deuterated PTI.LiBr.

Infrared spectroscopy is frequently used to investigate carbon nitride material. Ferrari *et al.*[140, 141] report three different bands in which the IR spectra of amorphous carbon nitrides occur. The first is the N-H/O-H region at ~3300 cm^{-1}, the second is the nitrile region at 2400 cm^{-1} and the third is the C-N stretching region at 1200 - 1600 cm^{-1}. Typically heptazine and triazine carbon nitrides have broad N-H/O-H peaks, a series of C-N bonding at 900 – 1600 cm^{-1} and small amounts of nitrile bonding. A sharp strong peak at 800 cm^{-1} is usually attributed to the 6 membered C_3N_3 ring out-of-plane bending vibration.[47, 59, 142]

IR spectra of the reported PTI materials show a distinct repeatable profile as compared to typical carbon nitride materials.[54, 56, 131] Our experimental spectra of PTI.LiBr and PTI.LiCl (Figure 3.8a) show a direct overlap of peak positions with a small variation in intensities. These match well with IR spectra of PTI materials that has been previously reported. [54, 56, 131] The region between 1600 and 990 cm^{-1} is commonly associated with C-N stretching.[59] The characteristic peak at 810 cm^{-1} is observed,[54, 56, 59] this can be from a triazine ring or a component of the heptazine system. No nitrile bonding is observed. Two clear peaks are observed at 3320 and 3200 cm^{-1} due to their wavenumber and peak shape they are assigned to N-H bonding. The assignment of this region has not been unanimously agreed upon in the literature, Chong *et al.*[54] reported that these two peaks are caused by primary and secondary amines, however the ‘perfect’ structure of the PTI material should contain no primary amines. Wirnhier *et al.*[56] suggested that the partial replacement of hydrogen on the bridging amines by lithium splits the primary amine peak resulting in the observation of two distinct peaks.

A deuterated PTI.LiBr material was synthesising by using deuterated DCDA as a precursor, this synthesised was developed as part of a neutron diffraction investigation of PTI. The ATR-IR spectrum of (Figure 3.8b) shows the peaks have shifted from 3320 and 3200 cm^{-1} to 2450 and 2390 cm^{-1}, this clearly indicates that both peaks are due to N-H/D bonding. Previous studies of other carbon nitride materials report vibrations due to C-NH-C bonding in the 1300-1600 cm^{-1} range.[59, 140, 143-145] However I do not observe any significant shift in this region due to the deuteration, which would be expected from C-NH-C bonding vibration, hence we do not observe indications of C-NH-C vibrations in the PTI.

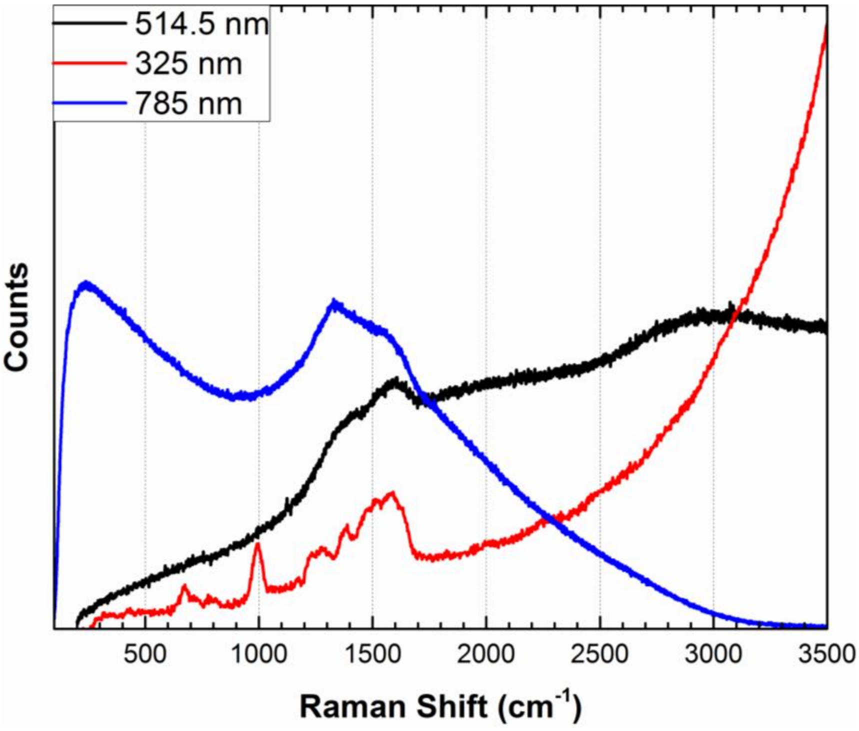

Figure 3.9. Raman spectra of PTI.LiBr at several different excitation wavelengths, 325 nm is shown in red, 514.5 nm is shown in black and 785 nm is shown blue.

Raman spectroscopy is widely used for investigating carbon nitrides, typically, two main peaks are observed at ~1400 and 1600 cm^{-1} Raman shift. These are referred to as the ‘G’ and ‘D’ peaks due to the similarities with the ‘G’ and ‘D’ peaks in graphite.[140, 146] Ferrari *et al.* have shown that Raman spectra of carbon nitrides have significant excitation wavelength dependence. They also report resonance enchantment of several peaks, including the nitrile peak at ~2400 cm^{-1} under UV exiction.[140, 146]

I obtained microbeam Raman data for our PTI.LiBr samples using a range of excitation wavelength from UV (325 nm) to visible (514.5 nm) and IR (785 nm) (Figure 3.9). A series of peaks is observed from 1200 – 1700 cm^{-1} under the UV laser excitation, these overlap with the C-N vibrations in the IR. These are the two main ‘G’ and ‘D’ peaks with maxima at 1340 and 1560 cm^{-1}. These peaks broaden significantly as the laser wavelength moves from the UV into the visible and near IR. As with the IR spectra no nitrile bonding is observed at any excitation wavelength. A broad peak at 2600 - 3200 cm^{-1} with a maxima around 2900 cm^{-1} is observed in the 514.5 nm excitation spectra. No functional groups associated with the PTI have peaks at this position, and no peaks are observed in the Raman UV/IR wavelength excitation or the IR spectra I suggest that this is an overtone (2G/2D) of the main ‘G’ and/or ‘D’ peaks. These overtones are a feature often seen for graphitic materials, it has also been reported for carbon nitrides at 514.5 nm excitation.[140, 146, 147] However it is not clear if any overtone in the UV excitation is masked by the rising fluorescent background or is just not observed. Strong N-H peaks are observed in the IR spectra, in addition the elemental analysis, XPS and proposed crystal structure suggest the presence of N-H bonding. However no peaks that could be attributed to N-H stretching are observed at any of these three excitation wavelengths. It is possible that the fluorescence in the 325 nm excitation may be concealing the expected N-H stretching, or these vibrations could be very weak. No N-H stretching peaks have been observed in the Raman spectra of other carbon nitrides.[130, 140, 146, 147]

Some excitation dependent resonance effects are observed such as for the peak at 1000 cm^{-1} which is only observed when using UV excitation and not observed with the visible or near-IR laser. This peak is reported for many other triazine and heptazine based carbon nitrides at certain excitation wavelengths and is commonly associated with C_3N_3 ring breathing mode.[130, 147] Significant broadening is observed in the Raman spectra as a function of laser wavelength, an effect commonly seen in carbonaceous materials including graphitic carbon nitrides.[141, 146-148] When comparing different laser wavelength, excitations by the 785 nm laser results in transitions to lower energy levels. Low energy states tend to be a result of vibrations with a large spatial extend. While UV wavelength excitations induce more localised vibrations. In a structure which is crystalline but with small degrees of disorder the phonon lifetimes significantly decrease over larger lengths compared to short lengths. The laser wavelength moves from UV excitations into the visible and near IR it accesses different sets of energy levels, caused by vibrations of different spatial extends, resulting in different levels of broadening across different excitation wavelengths.

3.3.4 SEM and TEM images of PTI materials

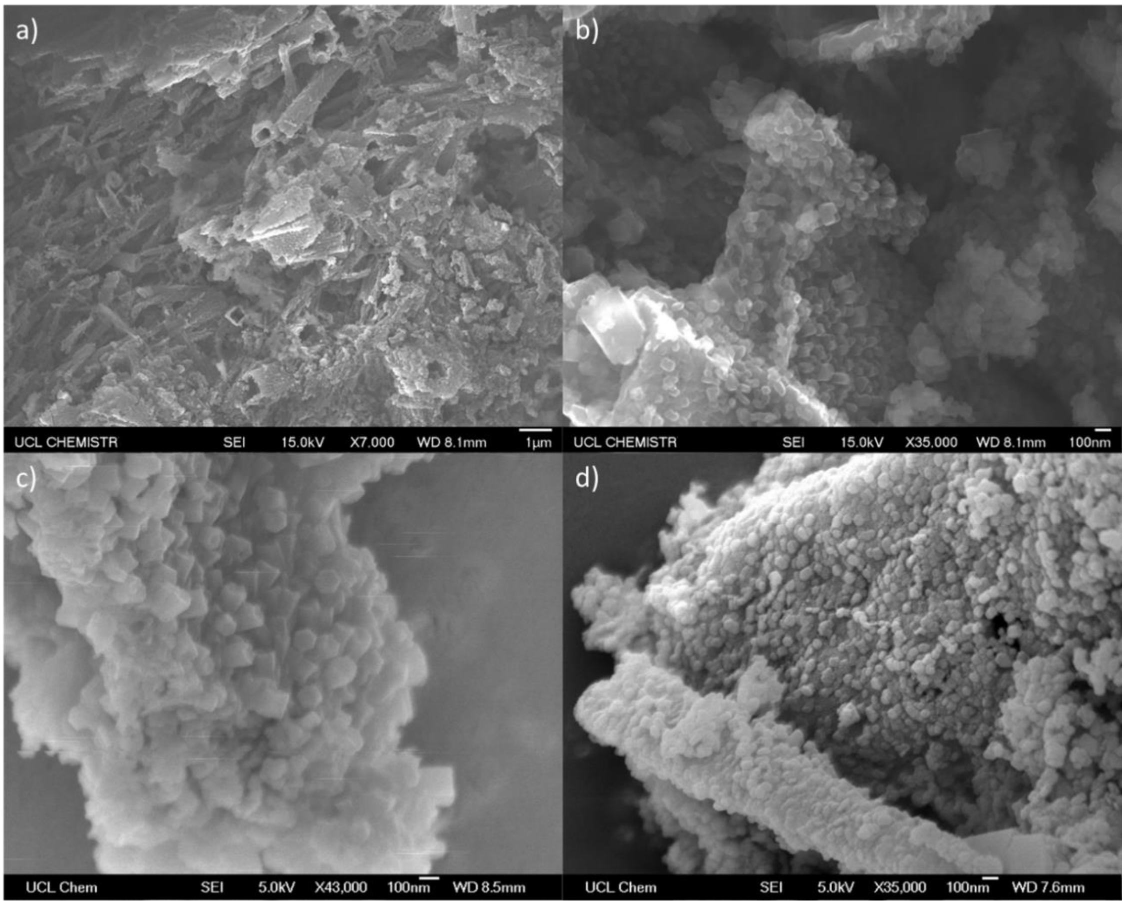
a)
UCL CHEMISTR SEI 15.0kV X7,000 WD 8.1mm 1μm
b)
UCL CHEMISTR SEI 15.0kV X35,000 WD 8.1mm 100nm
c)
UCL Chem SEI 5.0kV X43,000 100nm WD 8.5mm
d)
UCL Chem SEI 5.0kV X35,000 100nm WD 7.6mm

Figure 3.10. SEM images of bulk PTI materials. a) Image of PTI.LiBr showing large areas of hollow tubes. b) Image of PTI.LiBr showing hexagonal crystallites growing on the side of hollow tubes. c) Image of PTI.LiCl showing hexagonal crystallites face up as well on stacks on the side. d) Image of PTI.LiBr showing the hexagonal crystallites attached to the side of the hollow tubes as well as growing as a large block.

Scanning electron microscopy (SEM) is often used to investigated the crystal morphology of PTI.LiBr and PTI.LiCl, which has been reported as both small hexagonal crystallites[56, 131] or as large micron sized sheets.[149] SEM images of our recovered PTI.LiBr and PTI.LiCl (Figure 3.10) clearly show that the bulk is formed by prisms of hexagonal crystallites which are 40 to 160 nm across. These prisms of hexagons have very clear straight edges and form unaligned on the surface of hollow square tubes, these were also noted by Wirnhier *et al.*[56] The height of these columns varies but are commonly observed up to ~150 nm tall, which is roughly 400 layers thick. The crystallites shown here appear very similar to those reported by Bojdys *et al.*[131] and Wirnhier *et al.*[56] in their synthesis of the PTI.LiCl materials. I suggest that the large micron sized sheets reported by Bojdys *et al.*[149] may not be PTI.LiBr but another carbon nitride material, triazine based graphitic carbon nitride (TGCN) that is synthesised in the same reaction conditions and is reported as micron sized flakes (See Chapter 7 for more details).[41] Our SEM images of the different PTI structures (Figure 3.10) suggest that changing the intercalated halides has little effect on the diameter, shape or growth of the crystallites.

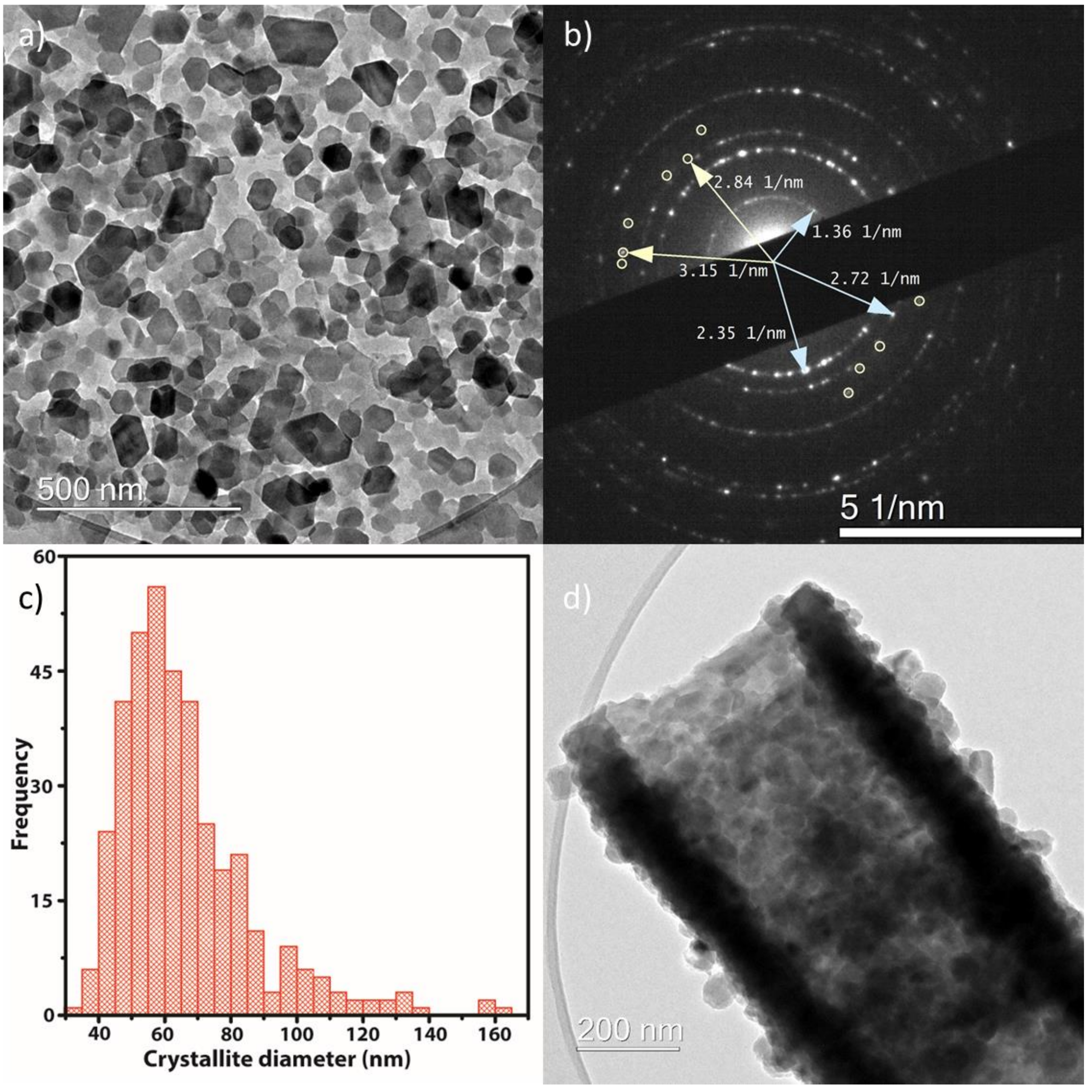
a)
500 nm
b)
2.84 1/nm
1.36 1/nm
3.15 1/nm
2.72 1/nm
2.35 1/nm
5 1/nm
c)
Frequency
0
15
30
45
60
Crystallite diameter (nm)
40
60
80
100
120
140
160
d)
200 nm

Figure 3.11. TEM images and SAED pattern of bulk PTI.LiBr. a) TEM image of various unaligned PTI crystallites. b) SAED of bulk PTI.LiBr showing the distances of the first three rings. c) Histogram of crystallite sizes counted from (a). d) TEM image of a tubular structure of PTI.LiBr crystallites.

To investigate the solid PTI material with TEM the powder was sonicated in a small volume of ethanol, as not to exfoliate PTI but to suspend small stacks in solution. This is then dropped on a holey carbon covered copper grid TEM grid and dried. Figure 3.11 clearly shows the same 40 to 160 nm straight edge crystallites observed in the SEM images of PTI.LiBr (Figure 3.10) and with the reported literature.[54, 56, 131] Manual counting of crystallites size shows a frequency distribution (Figure 3.11c) with a maxima around ~60 nm across. Typically crystallites are between 30-160 nm across, though most are between 40 – 100 nm across.

In-plane reflections (In blue)			Out-of-plane reflections (In yellow)		
Reciprocal distance	Real length	Reflection	Reciprocal distance	Real length	Reflection
1.36 nm^{-1}	8.5 Å	*100*	2.84 nm^{-1}	3.5 Å	*002*
2.35 nm^{-1}	4.9 Å	*110*	3.15 nm^{-1}	3.7 Å	*111*
2.72 nm^{-1}	4.3 Å	*200*			

Table 3.1. Table showing the measured characteristic distances from SAED.

Selected area electron diffraction (SAED) shows rings of distinct bright spots, a single crystal would be expected to give only set of reflections. These rings are due to many of the same crystallites orientated in different directions. The distance of the first three rings from the centre was measured (Figure 3.11b, in blue) as 1.36 nm^{-1}, 2.35 nm^{-1} and 2.72 nm^{-1}. The real lengths were calculated to be 8.5 Å, 4.9 Å and 4.3 Å respectively. These calculated values match exactly with the expected spacing of the *100*, *110* and *200* reflections of the proposed PTI.LiBr unit cell (Table 3.1). It is clear since most of the observed points can be labelled *hk0* that the vast majority of the crystallites are stacked with the planar *ab* axis parallel to the TEM grid. There are several spots that do not fit into the above distances, (Figure 3.11b in yellow) there are only a few of these unaccounted for reflections but they have distinct distances of 2.84 nm^{-1} and 3.15 nm^{-1}. These distances correspond to the *002* and *111* respectively, these reflections are due to a small quantity of prisms of PTI lying on their side allowing the observation of the out of plane reflections (Table 3.1). Unit cell parameters calculated from these reflections are in agreement with the proposed structure of PTI.LiBr and the PXRD patterns.

3.3.5 TGA analysis

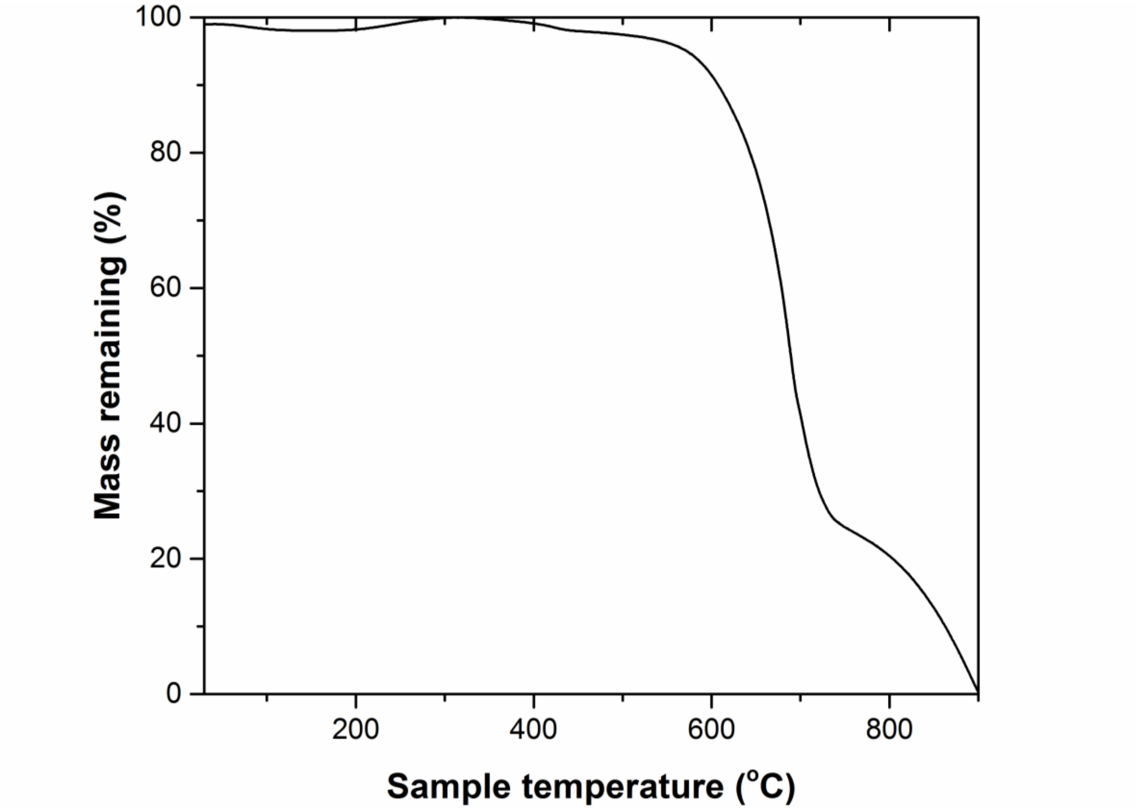

Figure 3.12. TGA of PTI.LiBr showing the mass change of the sample as it is heated to 900°C at 20°C min^{-1}.

Thermogravimetric analysis (TGA) analysis of PTI.LiBr (Figure 3.12). I also observe a slight decrease then increase in mass remaining between 25 and 450°C, this does not represent a significant mass loss but it is not clear what is causing this small event. This has been previously observed for PTI.LiCl.[150] After 560 °C 70% of the recorded mass is lost over the next 160°C, a temperature range associated with the decomposition of carbon nitride materials.[151, 152] A non-typical second mass loss event for carbon nitride materials[151, 152] is observed at 740°C in conjunction with the main event at ~600°C. At 900 °C the mass lost is 100%. The onset temperature of the main mass loss event is the same for PTI as other carbon nitrides suggesting that the CN framework is breaking down. [151, 152] The second mass-loss event is not typical of carbon nitrides, this atypical behaviour could be due to the presence of the intercalated ions. This observation is consistent by the lack of a second mass loss event in the TGA of intercalant free PTI (see section 4.1). However it is not clear how as the intercalants are causing the PTI framework to breakdown at a higher temperature.

Chapter 4 – De-intercalation and re-intercalation of PTI compounds

The characterisation of PTI materials has been discussed in the previous chapter. Here I focus on de-intercalation and re-intercalation procedures to manipulate the intercalated ions within the structure. This could lead to controllable ion exchange and properties tuning, to create new materials for future applications. Bojdys' *et al.*[149] exposed PTI.LiBr to potassium vapour to intercalate the material as an initial step to exfoliation (see Section 5.2). The intermediate step of potassium intercalation was not investigated. Chong *et al.*[54] stirred PTI.LiBr in aqueous ammonium fluoride with the aim of exchanging the intercalated halides. Reported XRD patterns suggest a partial exchange of bromine with fluorine. Elemental analysis shows a significant bromine content remaining in addition to loss of some lithium and nitrogen, raising unanswered questions as to the balance of charges in this new structure. McDermott *et al.*[38] reported that PTI.LiCl washed over several days caused the removal of the intercalated chlorine and most of the lithium. A combination of DFT calculations, XES, XAS and EELS was used to investigate the electronic structure of PTI.LiCl before and after washing, showing that intercalated ions independently play a significant role in determining the bandgap due to the splitting of nitrogen states. This study clearly showed the utility of ion exchange, but structural characterisation of the washed PTI.LiCl material was not reported. While these three reports have shown that manipulation of the ions within the PTI structures is possible, characterisation of the resultant materials is lacking. In this Chapter the PTI intercalation chemistry is investigated in detail. First, an intercalant free PTI was prepared and its structure was investigated. Then this compound was explored as a host material for a series of intercalation experiments forming new PTI materials. This work has shown the potential of PTI to act as a host to a wide variety of intercalants, providing a wide degree of tunability to the properties.

4.1 Synthesis and characterisation of intercalant free PTI (IF-PTI)

4.1.1 Background and context

This section develops the characterisation of the intercalant free PTI (IF-PTI), formed by a synthetic procedure similar to that reported by McDermott *et al.*[38]

4.1.2 IF-PTI synthesis

PTI.LiBr/PTI.LiCl was deionised via Sohxlet extraction.[38] In each extraction ~1.5 g of PTI was loaded into a cellulose thimble (Whatman Cellulose extraction thimbles, OD 27 mm, ID 25 mm, length 80 mm) and washed for >20 days with hot distilled water. The IF-PTI was recovered by placing the wet PTI in a centrifuge tube then adding ethanol (Millipore), shaking the tube for several minutes then centrifuging at 4500 rpm. The supernatant was then poured off, and the procedure repeated once more before being dried at 150 ˚C at 10^{-2} mBar and stored under an inert atmosphere. During the intercalation extraction procedure, the pH of the water reservoir changed from a starting value ~6 to close to 10. PTI.LiCl is reported to have two protons, two lithium and one halide within each void of the structure. The extensive washing of the material is expected to remove the LiCl component via dissolution of the salt. The additional Li is expected to exchange with a proton from the water, resulting in an increase in OH^- content within the aqueous medium.[153] The resulting material would therefore be expected to be purely containing carbon, nitrogen and hydrogen. The same mechanism of ion removal is expected to occur for PTI.LiBr, however less salt would be dissolved due to the low occupancy of the halide compared to the PTI.LiCl.

4.1.3 X-ray photoelectron spectra and analysis

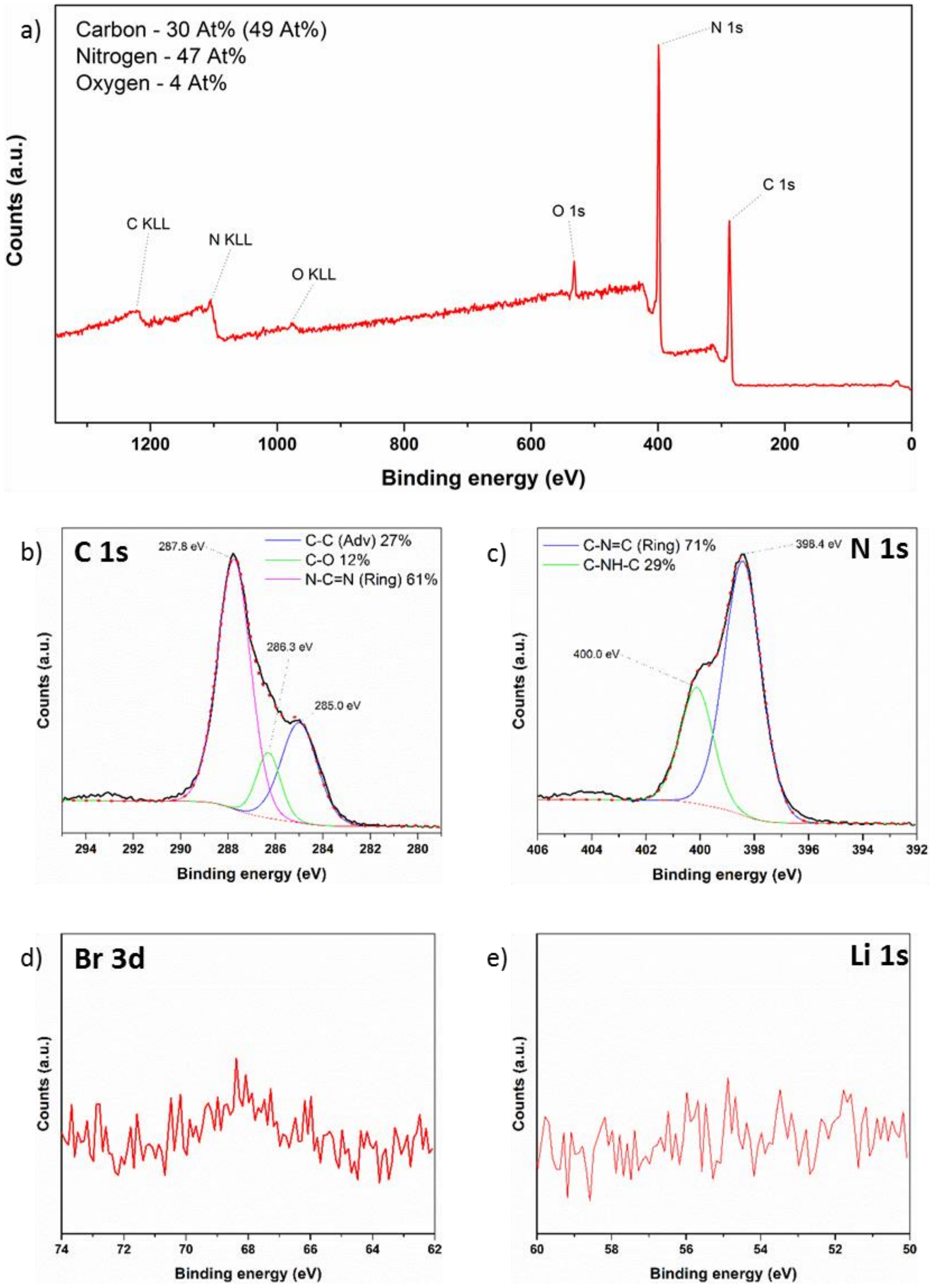

Figure 4.1. XPS Spectra of IF-PTI. (a) Survey spectrum. (b) Carbon 1s spectrum. (c) Nitrogen 1s spectrum. (d) Bromine 3p spectrum. (e) Lithium 1s spectrum.

The XPS survey spectra of IF-PTI (Figure 4.1a) show significant carbon, nitrogen, oxygen content. Compared to PTI.LiBr and PTI.LiCl the percentage of oxygen present is higher. While this might be taken as an indication that the carbon nitride backbone has been functionalised with oxygen containing groups, evidence that this is not the case is discussed in more detail later (Section 4.1.7). Atomic percentages of different elements are shown. For the carbon content, the number in brackets is that including the adventitious component. Excluding adventitious carbon the C to N ratio was found to be 1 to 1.57, close to the expected PTI stoichiometry (1 to 1.5). Which indicates retention of a PTI structure though it slightly higher than observed for PTI.LiBr and PTI.LiCl.

As with PTI.LiBr and PTI.LiCl (Figure 3.6, 3.7) after peak fitting there are three distinct carbon environments that can be observed (Figure 4.1b). The peak at 285.0 eV is assigned to adventitious carbon, a peak assigned to C-O bonding occurs at 286.3 eV and the peak at 287.8 eV assigned to the in-ring C-N-C bonding.[41] The N1s region also shows two distinct environments (Figure 4.1c), the peak at 398.4 eV is assigned to the nitrogen environment inside the triazine ring, while the peak at 400.2 eV is assigned to the nitrogen bridging environments. The area of the peak at 398.5 eV is ~2.5 times more than the peak at 400.2 eV, close to the expected 1:3 ratio.

No peaks are observed above the noise level for the bromine 3d (Figure 4.1d) or for lithium 1s (Figure 4.1e). While the signal to noise ratio for lithium is low, it is clear that both it and the bromine content have significantly decreased.

The relative peak positions and areas are almost identical to those seen in the C1s and N1s spectra of PTI.LiBr and PTI.LiCl (Figure 3.6, 3.7). This is an indication that the washing procedure used to remove the intercalated ions has not resulted in any functionalisation of the carbon nitride backbone but only removed the intercalated lithium and bromine. PTI.LiBr and PTI.LiCl have lithium taking the place of hydrogen on the bridging N-H groups. As the PTI is washed the intercalated LiBr is simply dissolved into the water, and the N-Li groups reacts with the water to form the N-H bonds and LiOH. This results in the pH of the water reservoir of the Soxhlet extractor changing from ~6.5 to 10 after the washing procedure has taken place.

4.1.4 NMR and elemental analysis

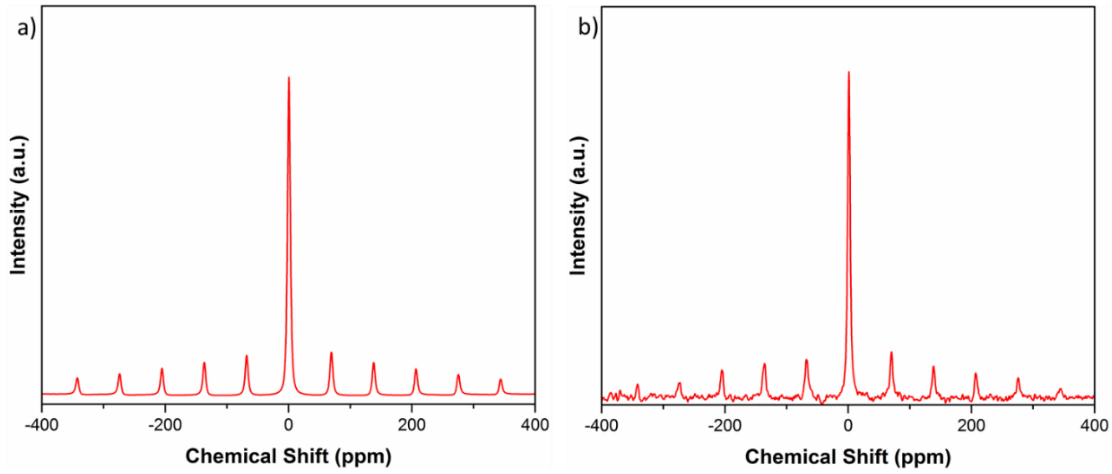

Figure 4.2. Solid state ^{7}Li MASS NMR of two different PTI materials. a) PTI.LiBr. b) IF-PTI.

Given the low sensitivity of lithium from XPS solid state NMR was used to compare the lithium contents in PTI.LiBr (Figure 4.2a) and IF-PTI (Figure 4.2b). The amount of Li^+ in IF-PTI was found to be reduced by 99 +/- 0.1% compared with the as-synthesised PTI.LiBr.

Bulk CNHBr elemental analysis of PTI.LiBr and IF-PTI were found to give composition of $C_{12}H_{9.8}N_{16.7}Br_{1.3}$ and $C_{12}H_{13.2}N_{16.2}Br_{0.05}$, respectively. This shows only a small change in the C/N ratios while significant loss of bromine from 65% to 2.5% occupancy and growth of hydrogen content most likely due to the replacement of lithium with hydrogen, along with water intercalation into the structure. This last point is discussed in detail in Section 4.1.7.

4.1.5 TEM and SEM images

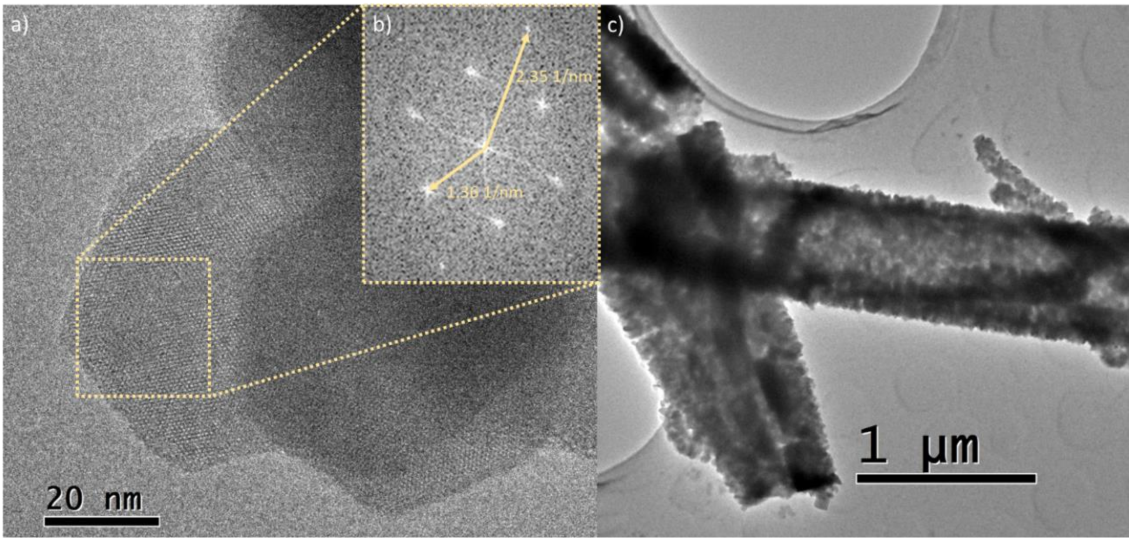

Figure 4.3. TEM images of IF-PTI. a) TEM image showing crystalline IF-PTI hexagons. b) Fourier transformed of the selected area shown in (a). c) TEM image showing large tube formed from PTI crystallites.

In order to obtain TEM images, the IF-PTI sample was sonicated in methanol, and the suspension was then dropped onto a TEM grid and the solvent was allowed to evaporate. TEM experiments were carried out using the TITAN FEI 80/300 instrument at Imperial College London in collaboration with Dr Vasiliki Tileli. The resultant images show (Figure 4.3a) show the same straight edged hexagonal crystallites as observed previously for PTI.LiBr and PTI.LiCl (Figure 3.10). Importantly I observe no notable increase in defect density in the crystallites following washing and extraction of the intercalated ions. Direct observation under TEM resulted in the degradation of the sample by the electron beam after several minutes. This effect was more significant when taking SAED images. Fourier transforms of the high resolution images were used as an alternative to SAED due to this problem. The distances between bright spots on the Fourier transformed image (Figure 4.3b) were measured as 1.36 nm^{-1} and 2.35 nm^{-1}, identical to those observed in the SAED of PTI.LiBr for the *100* and *110* reflections, showing that the in-plane lattice parameter has remained the same after the washing procedure. No out-of-plane reflections could be observed. IF-PTI shows the same average crystallite size and shape (Figure 4.3c) as observed in both PTI materials. Indicating that the removal of intercalated ions is a relatively gentle procedure that occurs without significant disruption of the bulk PTI structure. These images, combined with the XPS data, show that the de-intercalation procedure has removed the lithium and halide intercalants without causing significant structural damage to the covalently bonded PTI framework.

4.1.6 PXRD patterns and analysis

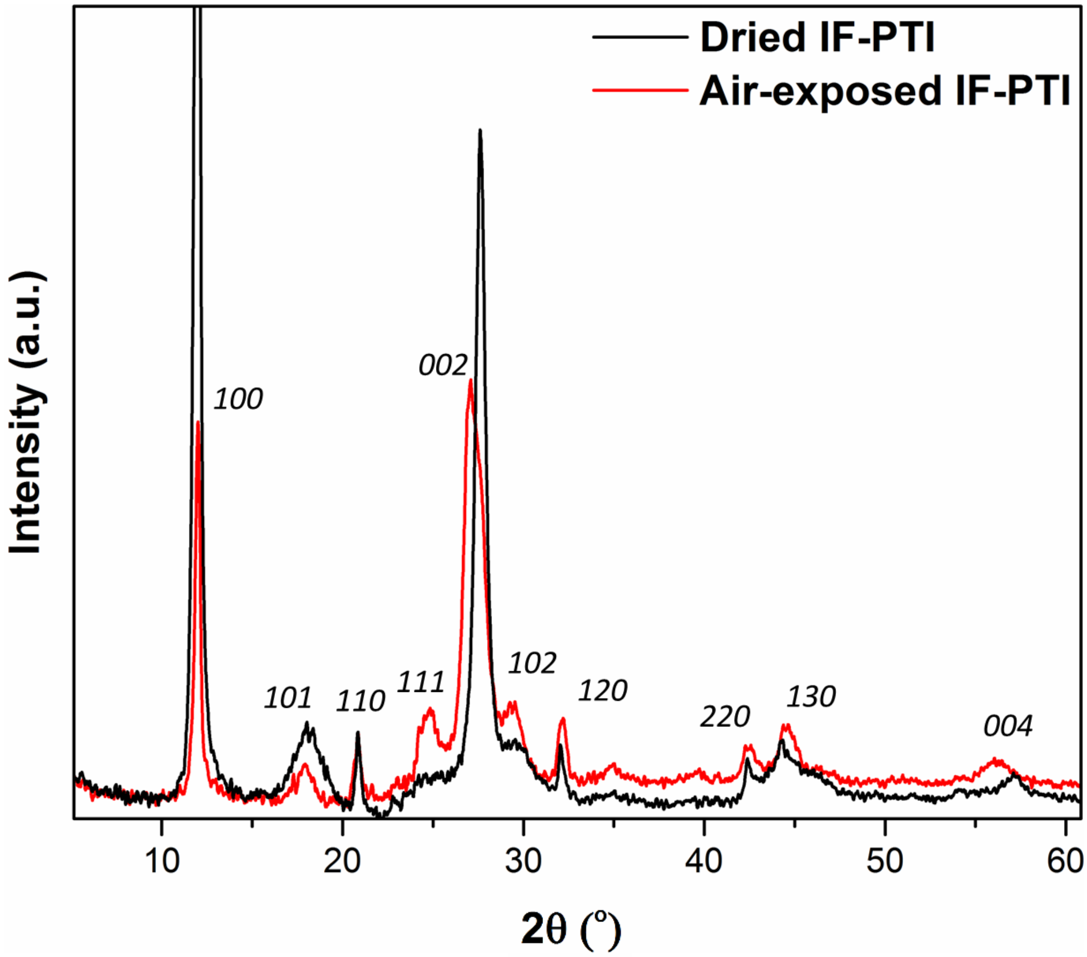

Figure 4.4. PXRD pattern of dried IF-PTI before and after exposure to air.

The PXRD patterns of dried IF-PTI (Figure 4.4) can be fit using the same in-plane lattice parameters as those used for PTI.LiBr (Figure 3.3). Significantly, all peaks with an out of plane component have broadened and shifted to higher values of 2θ compared to PTI.LiX, showing the interlayer distance for this material has been substantially reduced from 3.52Å to 3.22Å, as explained by the deintercalation of the large halide ions. The base gallery height of the IF-PTI is therefore 0.13Å smaller than even that of graphite (3.35Å),[154] meaning that the PTI layers are stacked closer together.[40] [3737]In the XRD pattern of IF-PTI I also observe the appearance of a peak near 18˚ 2θ which can be assigned to *101* planes in the hexagonal unit cell, which are not observed for PTI.LiBr and PTI.LiCl. The appearance of this peak is likely due to a change in symmetry as the stacking moves from AA' where the voids 'line-up' along the c axis to AB where a triazine ring is located directly above and below each void. In addition reflections with an *l* component have significantly broadened such as the broad *002*. Peaks due only to *hk0* reflections are sharp, this asymmetric peak broadening was also observed for PTI.LiCl and PTI.LiBr.. During our experiments I observed that samples of the IF-PTI material showed a dramatic change after exposure to air (Figure 4.4), while the in-plane *hk0* peaks do not shift in position there is a clear change in any peak with an *l* component, such as the *002* which shifts from 3.23Å to 3.29Å after exposure. There is also a large shift in the relative intensity of the different peaks, leading to the ‘emergence’ of peaks that were previously buried in the background. Given the hexagonal arrangement has remained intact it is clear that exposing the IF-PTI to air has resulted in an increase in the inter-layer spacing. FTIR measurements indicate this is most likely due to spontaneous absorption of H_2O from the surrounding atmosphere (Figure 4.5).

4.1.7 IR spectra and analysis

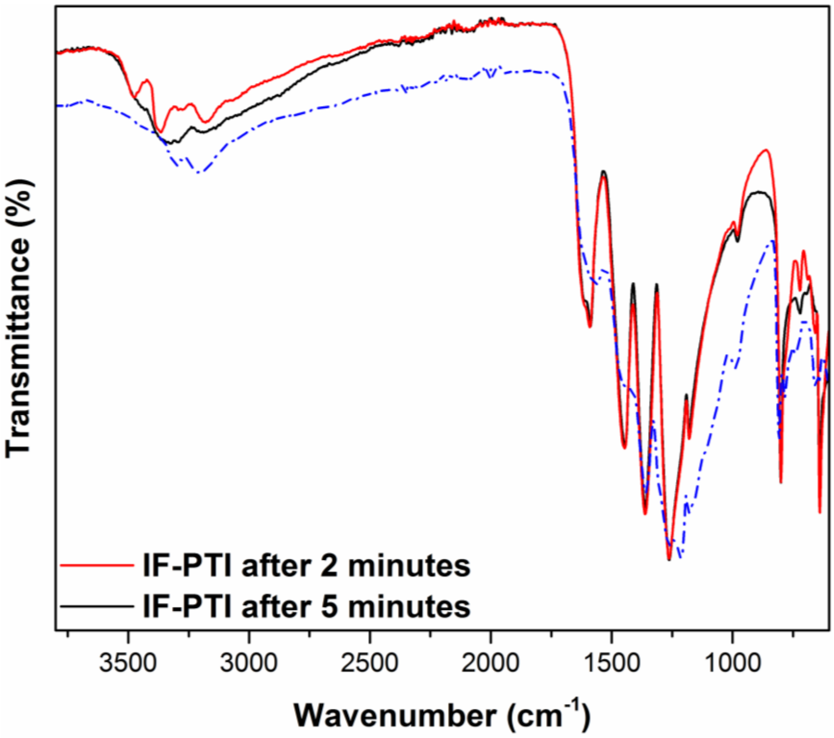

Figure 4.5. ATR-IR spectra of IF-PTI showing the comparison between PTI.LiBr and IF-PTI, also shown is the difference between IF-PTI after exposure to air for 2 minute and after 5 minutes.

The ATR-IR spectra of IF-PTI shows the same C-N bonding peaks in the 1100-1700 cm^{-1} region as seen in the PTI.LiX (where X = Cl, Br) compounds, however the peaks have significantly narrowed. In addition the peak at 810 cm^{-1} seen in PTI.LiX associated with out of plane bending of six membered ring[54, 56, 59] is also observed. More interestingly however is the dramatic change in the high wavenumber region after only a few minutes as IF-PTI was exposed to ambient atmospheric conditions (Figure 4.5). Peaks seen in this area broaden considerably after several minutes exposure most likely due to an increase in the hydrogen bonding, these changes occurred rapidly, on a timescale of a few minutes. These peaks are typically assigned to N-H stretching vibrations of the PTI materials.[55, 56, 129, 130] An initial interpretation could be that these changes in the IR spectra might indicate some disordering associated with the N-H positions. However analysis by TGA suggest that the changes actually reflect intercalated H_2O molecules hydrogen bonding to the bridging N-H groups (Figure 4.6).

4.1.8 TGA and estimation of the absorbed water content

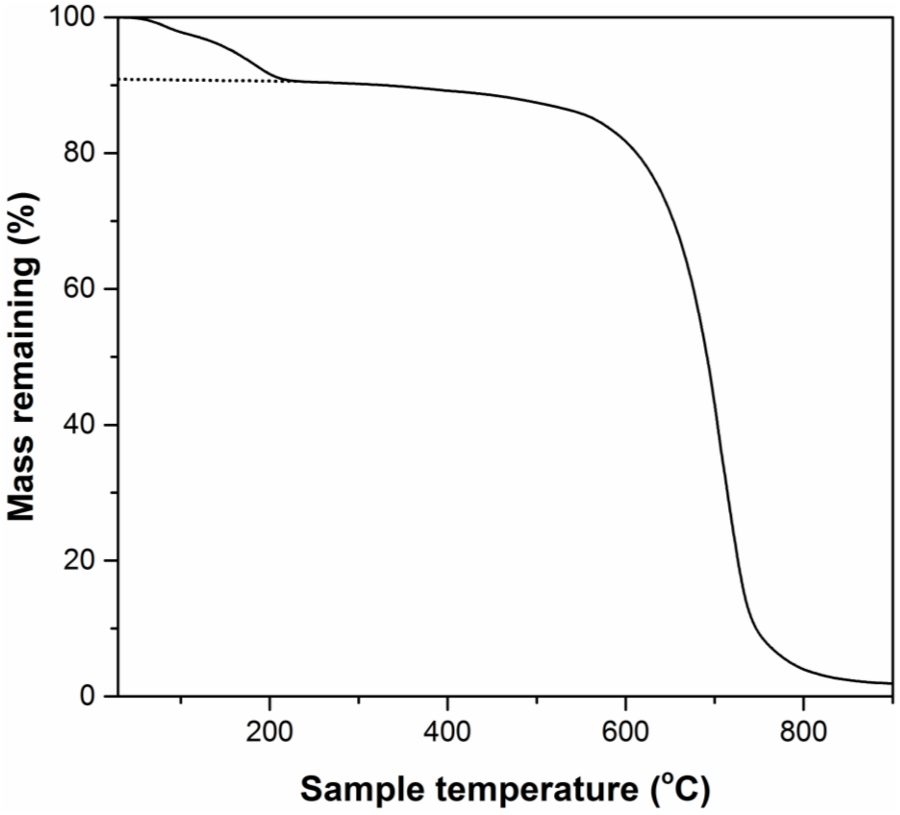

Figure 4.6. TGA of wet IF-PTI showing only two mass loss events one associated with carbon nitride and the other with the removal of the intercalants, the sample was heated to 900˚C at 20˚C min^{-1}.

It is clear from the IR and XRD data that upon exposure, a component of the air is intercalating in the PTI Layered structure causing the expansion of the gallery height. It is also found that heating the air exposed IF-PTI under vacuum at 200˚C resulted in the removal of the intercalants species Given that the intercalants are reversibly removed at 200 ˚C and appear to induce a significant change in the N-H or O-H stretching region I suggest that the intercalant is water. To test this IF-PTI was submitted for TGA

(Figure 4.6). This showed that 9% of the mass was lost between 0 and 200˚C which is suggestive of water loss due to the temperature range. If all of this lost mass was due to intercalated water residing in the pores that would result in a stoichiometry of $C_{12}N_{18}H_{10}O_2$ for wet IF-PTI assuming an idealised $C_{12}N_{18}H_6$ composition for dry IF-PTI. The main mass loss event occurs between 600 ˚C to ~800 ˚C, similar to that for other carbon nitrides including PTI.LiBr. However unlike PTI.LiBr a second mass loss event is not observed at 700 ˚C in conjunction with the main event (Figure 3.12). Given that all the characterisation techniques I have used have shown the only change from the washing procedure to be the loss of the intercalated lithium and halide components it is clear that the intercalated ions are responsible for this second event.

4.1.9 Summary

From TEM, XPS and IR results it is clear that the washing procedure to form IF-PTI has not damaged the PTI carbon nitride backbone. The fact that the crystalline layered structure has remained intact demonstrates the gentle nature of the de-intercalation method. However a washing time of several weeks was required for complete removal of the intercalants indicating the relative stability of the intercalated structure, along with slow kinetics of the de-intercalation process. When the intercalants were removed the PTI backbone is not disrupted, but does change gallery height to account for the loss of the large halide ions. However when exposed to air for only several minutes the sheets re-expand to accommodate water into the empty voids, an effect not observed when the PTI sheets area already intercalated with lithium halides. In addition the absorbed water molecules can be removed by heating under reduced pressure without damage. This suggests the PTI backbone will ‘pull-in’ intercalants to form a more stable structure if it can. To test the degree to which this holds true I exposed IF-PTI to a variety of intercalants to see what it would intercalate.

4.2 Reintercalation of PTI.LiBr and PTI.LiCl

4.2.1 Context and synthesis

I have shown that IF-PTI has the capacity to reversibly intercalate water into its carbon nitride layered structure. From the synthesis of PTI.LiCl and PTI.LiBr it is clear that lithium halide can intercalate into the structure. It is not clear if his initial intercalation is a result of the ions being trapped within the structure during the synthesis or if they preferentially intercalate into the framework. The residual salts have been removed to form IF-PTI, hence we can expose the empty PTI structure to the relevant molten salt to re-intercalated the lithium halide.

IF-PTI (180mg) was added to a eutectic mix of either (KBr Alfa Aesar 0.96g: 1.04g LiBr Aldrich) or (KCl Aldrich 1.1g : 0.9g LiCl Aldrich). These were ground together and sealed inside a quartz ampoule and under static >10^{-6} mbar pressure. This was then heated 600˚C and held for a period of time (up to 12 hours). The recovered block was then washed multiple times with water (Millipore), then ethanol and dried.

In these syntheses when IF-PTI formed from PTI.LiBr was exposed to molten chloride salts, the recovered material was show to be re-intercalated PTI.LiCl (Ri-PTI.LiCl). For IF-PTI formed from PTI.LiCl then exposed to molten bromide salts formed Ri-PTILiBr.

4.2.2 PXRD patterns and analysis

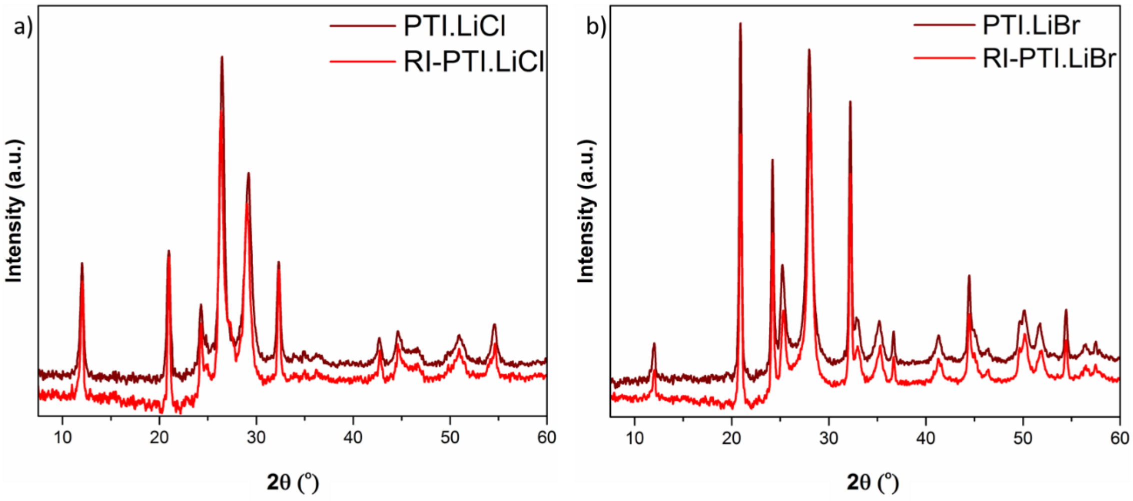

Figure 4.7. PXRD patterns showing as synthesised PTI compared against the washed and re-intercalated material. a) PTI.LiCl and Ri-PTI.LiCl. b) PTI.LiBr and Ri-PTI.LiBr.

The PXRD patterns of Ri-PTI.LiCl and Ri-PTI.LiBr (Figure 4.7) are compared with those of PTI.LiCl and PTI.LiBr respectively, and no significant differences in peak positions or relative intensity were noted. This suggests that the re-intercalation procedure has resulted in the synthesis of the original PTI.LiBr and PTI.LiCl, not only showing that the re-intercalation process works but that the carbon nitride layers remain unaffected by this process.

4.2.3 XPS spectra and analysis

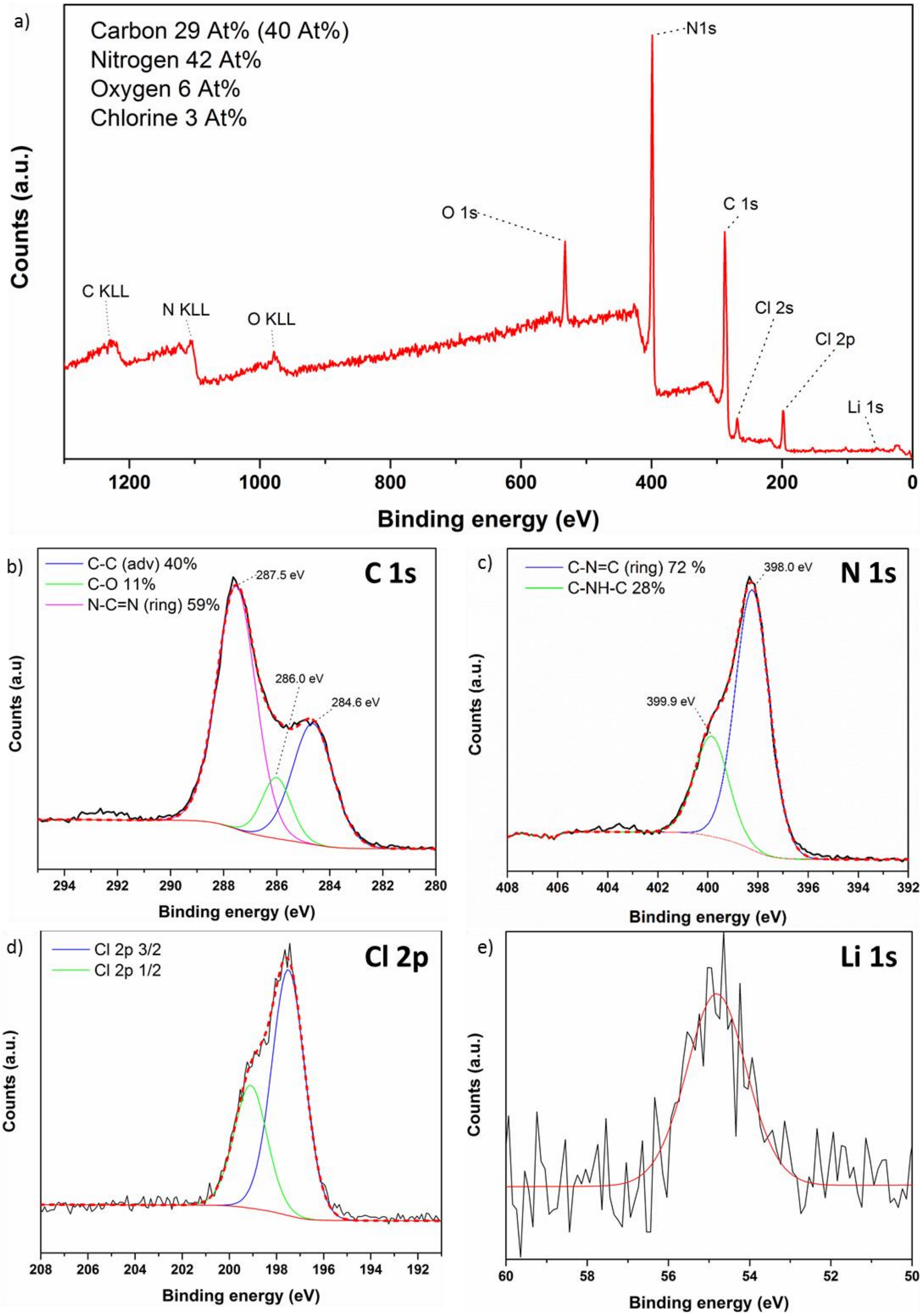

Figure 4.8. XPS Spectra of Ri-PTI.LiCl (a) Survey spectrum. (b) Carbon 1s spectrum. (c) Nitrogen 1s spectrum. (d) Chlorine 2p spectrum. (e) Lithium 1s spectrum.

The XPS survey spectra of Ri-PTI.LiCl (Figure 4.8a) shows significant carbon, nitrogen, oxygen and chlorine content. Atomic percentages of different elements are shown, for the carbon content the number in brackets is the carbon content including the adventitious component. Excluding adventitious carbon the C to N ratio was found to be 1 to 1.5, which is the expected PTI stoichiometry.

After peak fitting of the C1s spectrum (Figure 4.8b) it is clear that the profile is the same as seen for PTI.LiCl (Figure 3.7a) with the same three distinct carbon environments with the same relative peak positions and areas. The adventitious carbon peak appears at 284.6 eV, the in-ring C-N-C bonding at 287.5 eV and the C-O bonding peak at 286.0 eV.

As with all the PTI N1s region was composed of two distinct environments (Figure 4.8c), the peak at 398.0 eV associated with nitrogen environment inside the triazine ring and the peak at 399.9 eV which is assigned to the nitrogen bridging environments. The area of the peak at 398.0 eV is ~2.6 times more than the peak at 399.9 eV this is close to the expected 3:1 ratio.

Two strong peaks are observed for the single chlorine 2p environment (Figure 4.8d), no bromine peaks are observed. A significant lithium peak (Figure 4.8d) is observed, identical to that observed for the Li 1s spectra in PTI.LiCl (Figure 3.7e).

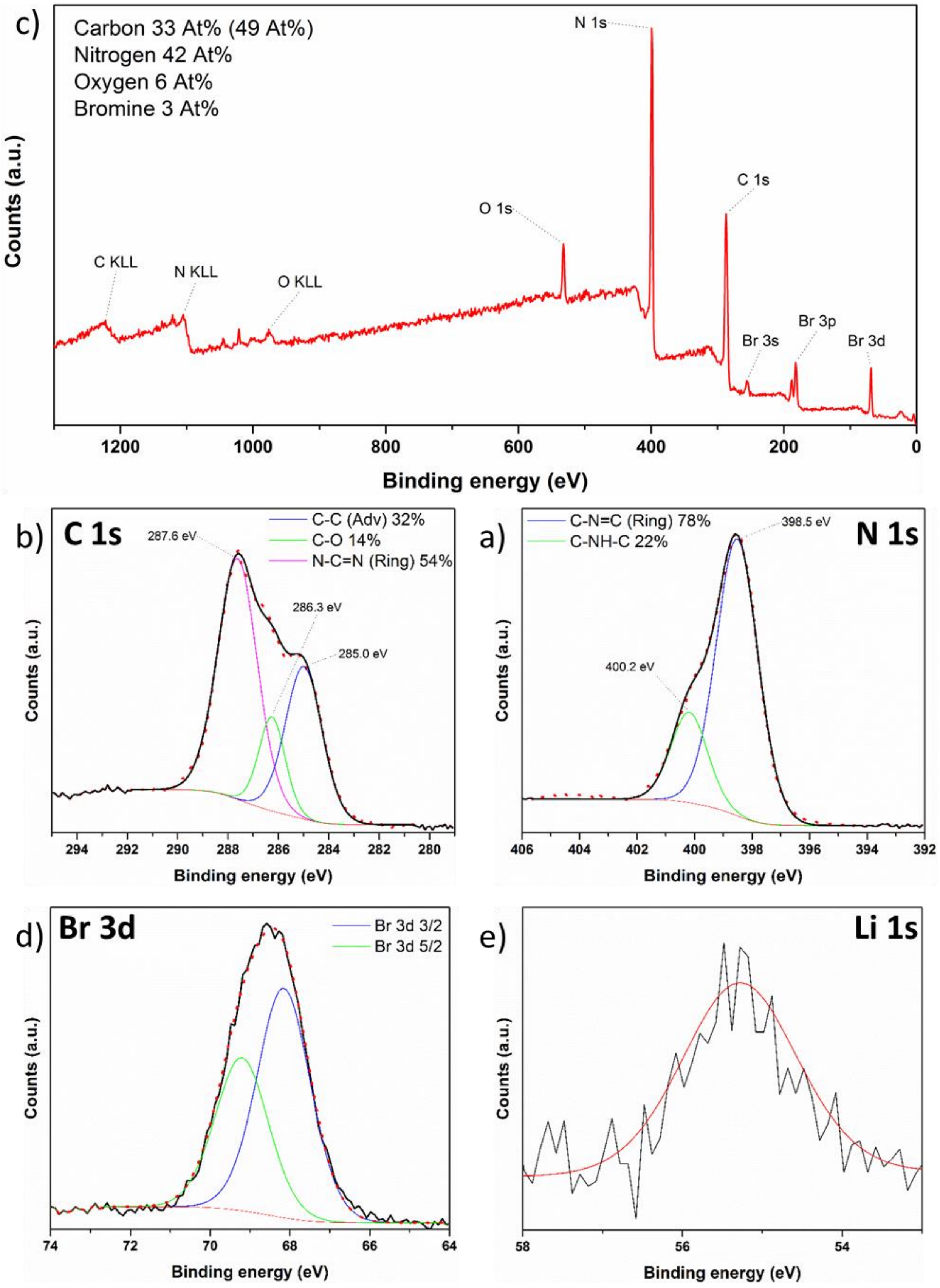

Figure 4.9. XPS Spectra of Ri-PTI.LiBr. (a) Survey spectrum. (b) Carbon 1s spectrum. (c) Nitrogen 1s spectrum. (d) Bromine 2p spectrum. (e) Lithium 1s spectrum.

The XPS survey spectra of Ri-PTI.LiCl (Figure 4.9a) shows significant carbon, nitrogen, oxygen and chlorine content. Atomic percentages of different elements are shown, for the carbon content the number in brackets is the carbon content including the adventitious component. Excluding the adventitious component the C to N ratio was calculated to be 1 to 1.58, which is close to the expected PTI stoichiometry.

After peak fitting of the C1s spectrum (Figure 4.9b) it is clear that the profile is that seen for PTI.LiBr (Figure 3.6a) with the same three distinct carbon environments with the same relative peak areas. An adventitious peak at 285.0 eV appears, the in-ring C-N-C bonding at 287.6 eV and the C-O bonding peak at 286.3 eV.

As with all the PTI materials the N1s region was fitted with two distinct environments (Figure 4.9c), the peak at 398.5 eV associated with nitrogen environment inside the triazine ring and the peak at 400.2 eV which is assigned to the nitrogen bridging environments. The area of the peak at 398.5 eV is ~2.6 times more than the peak at 400.2 eV this is close to the expected 3:1 ratio.

Two strong peaks are observed for the one bromine 3d environment (Figure 4.9d), no chlorine environments are observed. A significant lithium peak (Figure 4.9e) is observed. It is clear from comparing the Li 1s spectra from PTI.LiCl (Figure 3.7e), IF-PTI (Figure 4.1e), Ri-PTI.LiCl (Figure 4.8e) and Ri-PTI.LiBr (Figure 4.9e) that the lithium content was almost completely removed by the washing procedure, exposing the empty PTI framework to molten salt melt has resulted in the re-intercalation of lithium. The bromine content observed in Ri-PTI.LiBr is higher than that observed for PTI.LiBr, with 65 % and 48 % respectively. It is clear in both re-intercalated materials lithium and the relevant halide anion have been re-introduced into the carbon nitride framework. The re-intercalated material appears almost identical to the bulk synthesised PTI.LiBr and PTI.LiCl, however Ri-PTI.LiBr has a higher occupancy halide while Ri-PTI.LiCl has a lower halide occupancy compared to before washing. It is not clear why the occupancy of the re-intercalated material has varied between samples.

4.2.4 IR spectra and analysis

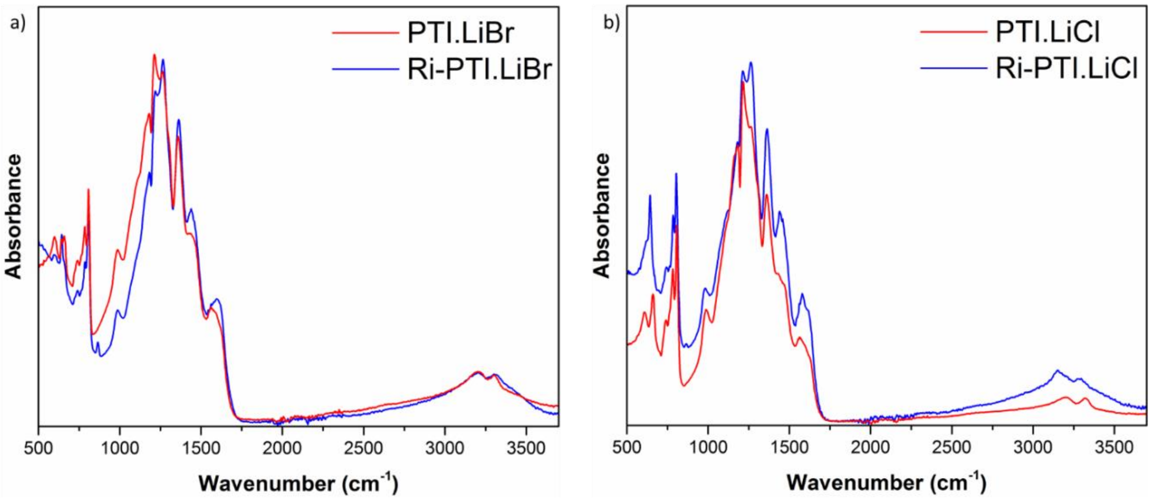

Figure 4.10. ATR-IR spectra showing the prewashed and re-intercalated PTI materials. a) PTI.LiBr and Ri-PTI.LiBr. b) PTI.LiCl and Ri-PTI.LiCl.

The IR spectra of Ri-PTI.LiBr and Ri-PTI.LiCl are compared with PTI.LiBr and PTI.LiCl (Figure 4.10), no additional or absent peaks are observed in either re-intercalated spectra. Some intensity differences such as in the higher absorbance N-H peaks in the chlorine based sample are observed. Also of note is that the broadened vibrations have reappeared compared to IF-PTI.

4.2.5 Summary

I have succesfully re-intercalated lithium halides back into the empty carbon nitride framework of IF-PTI. Which was shown that the washing procedure followed by reintercaled with a different halide is effectively indistiguishable from those synthesised via DCDA and a halide salt mix. These experiments have confirmed that PTI is carbon nitride framework with lithium halide intercalated into the structure which can be removed and re-intercalated without damaging the carbon nitride framework.

4.3 Synthesis and characterisation of PTI.HCl

4.3.1 Context and synthesis

PTI.HCl was previously synthesised by Zhang *et al.*[129] via a high pressure (0.5 - 1 GPa) solvothermal synthesis from melamine and cyanuric chloride at 500˚C. The material was characterised by IR, XRD and EELS which was used to show significant chlorine component. Further characterisation including Raman spectroscopy and DFT calculations was reported by McMillan *et al.*[130] This material was shown to have a PTI based framework with HCl intercalated into the voids. Unlike the other PTI materials the Cl^- ions sits within the carbon nitride layer, with the counter hydrogen protonating an in-ring nitrogen. This compound has recently been predicted by McDermott *et al.* to show improved photocatalytic hydrogen evolution under UV-visible illumination due to its optimised band gap.[38]

The structure of the PTI.HCl material can be seen as a PTI framework with intercalated HCl. Section 4.1 and 4.2 have shown the intercalants in PTI can be removed and re-intercalated without damaging the PTI framework. This section details a new synthesis route to form PTI.HCl via the re-intercalation of HCl into IF-PTI. This method is distinctly different to that reported by Zhang *et al.*[129] and represents the first room pressure synthesis of PTI.HCl.

IF-PTI (100mg) was added to 5 Molar HCl solution (75ml, Sigma Aldrich) which then refluxed for 4 days. The resulting powder was recovered by filtration and then washed several times with distilled water (Millipore) and then ethanol, before being dried at 150 ˚C at 10^{-1} mBar and stored under an inert atmosphere.

4.3.2 XPS spectra and analysis

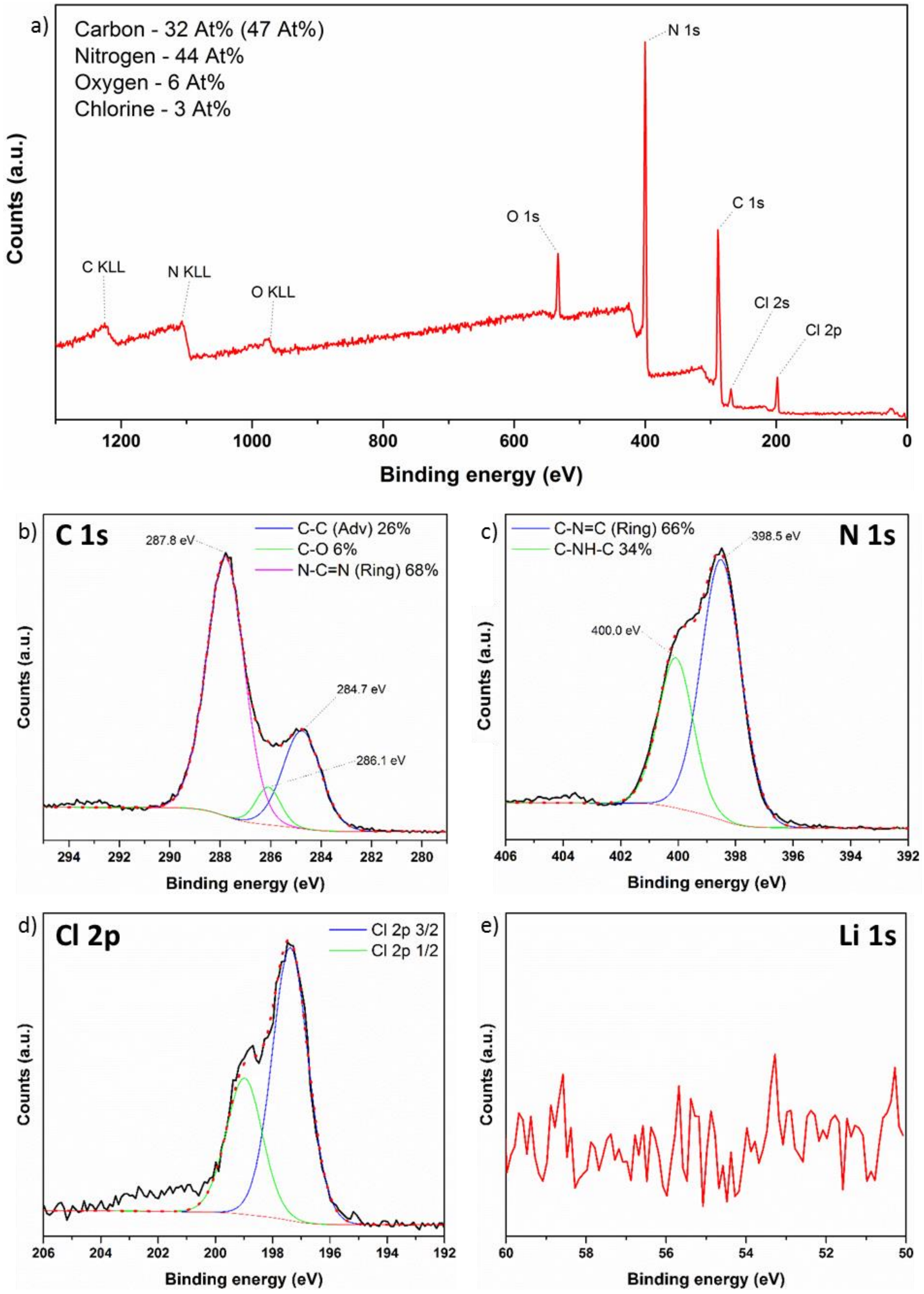

Figure 4.11. XPS Spectra of PTI.HCl. (a) Survey spectrum. (b) Carbon 1s spectrum. (c) Nitrogen 1s spectrum. (d) Chlorine 2p spectrum. (e) Lithium 1s spectrum.

The XPS survey spectra of PTI.HCl (Figure 4.11a) shows significant carbon, nitrogen, oxygen and chlorine content. Atomic percentages of different elements are shown, for the carbon content the number in brackets is the carbon content including the adventitious component. Excluding the adventitious carbon component the C to N ratio was calculated to be 1 to 1.4, which is the expected PTI stoichiometry.

After peak fitting the C1s spectrum (Figure 4.11b) the same three distinct carbon environments with the same relative peak areas as observed for other PTI materials. The peak at 284.7 eV is assigned to adventitious carbon, while the in-ring C-N-C bonding is assigned to the peak at 287.8 eV and the C-O bonding peak to the peak at 286.1 eV.

As with all the PTI that this thesis has dealt with the N1s region shows two distinct environments (Figure 4.11c), the peak at 398.5 eV is associated with nitrogen environment inside the triazine ring and the peak at 400.0 eV which is assigned to the nitrogen bridging environments. The area of the peak at 398.5 eV is ~2 times greater than the peak at 400.0 eV which is further away from the 3:1 ratio than the other PTI structures explored in this thesis. Zhang *et al.*[129] and McMillan *et al.*[130] reported in their high pressure synthesis of PTI.HCl that the additional hydrogen from the halide preferentially protonates a nitrogen in the triazine ring. Given the relatively high occupancy of chlorine significant protonation of nitrogen is likely to occur. It would be expected that these C-N(-H)-C would shift the position of these environments to a higher binding energy, resulting in a relatively larger peak at 400.0 eV and a lower ratio compared to other PTI materials.

Two strong peaks are observed for the single chlorine 2p environment (Figure 4.11d), most interesting no lithium environments are observed (Figure 4.11e). Previous re-intercalation materials have always used a lithium halide. This shows that it isn’t necessary for the intercalation to be successful. Given the intercalated chlorine and the lack of any lithium this strongly indicates the formation of PTI.HCl. The chlorine content observed in our synthesised PTI.HCl is lower than that reported for Zhang *et al.,* with chlorine occupancies of 55 % and 100 % respectively.

4.3.3 PXRD pattern and literature comparison

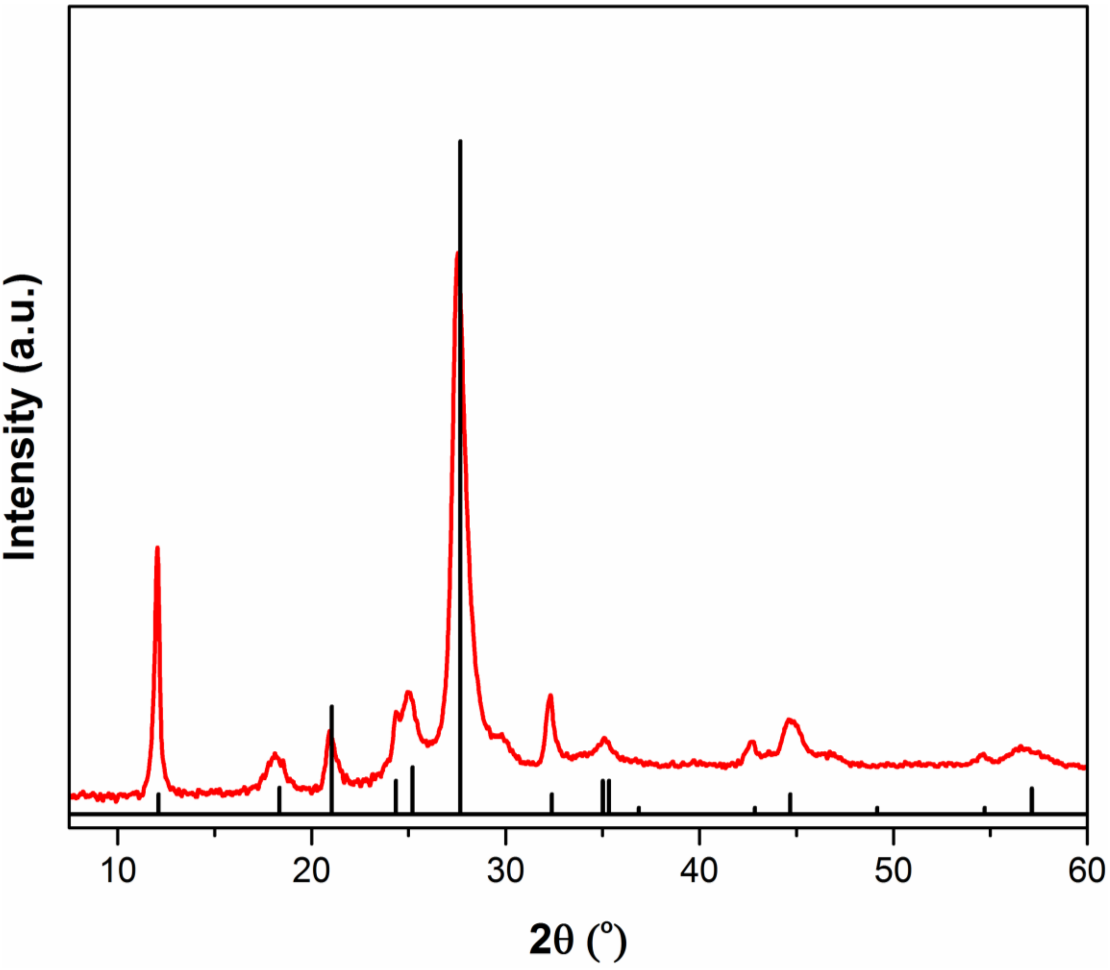

Figure 4.12. Experimental PXRD of PTI.HCl showing a close match when compared with peak positions reported by Zhang *et al.*[129]

The peak positions of the experimental XRD pattern of our recovered material (Figure 4.12) closely resemble that reported by Zhang *et al.*[129] However a difference in the intensity is observed such as in the *100*, *110* and *210* reflections. McMillan *et al.* compared the experimental and calculated XRD pattern of PTI.HCl synthesised by high pressure at different chlorine occupancies.[130] These showed that as the chlorine occupancy drops the *100* reflections became significantly more intense. Given that the peak positions remain the consistent with the literature it is likely that the variation in intensity is due to differences in chlorine occupancy as seen in the XPS. A peak at ~18˚ 2θ is observed similar to that seen in IF-PTI (Figure 4.4) which is assigned to the *101* reflection, the presence of this reflection is due to the layers no longer being AA’ stacked but rather AB. The presence of the AB stacking suggests that the chlorine ion is occupying a position within the plane of the void, this is in contrast to the where the halide sits in between the layers and forcing AA' stacking to occur. The same asymmetric broadening effects as seen in the other PTI materials are observed.

4.3.4 IR spectra and analysis

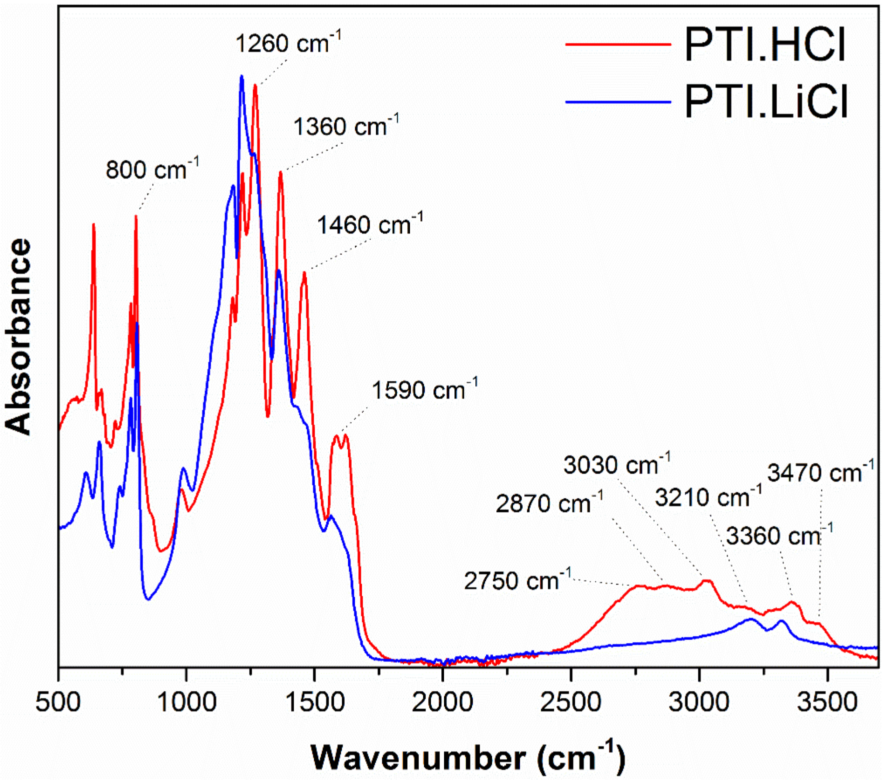

Figure 4.13. ATR-IR spectra of PTI.HCl compared with PTI.LiCl showing a very similar C-N bonding profile but additional vibrations in the 2700 – 3000 cm^{-1} region.

The ATR-IR spectrum of PTI.HCl (Figure 4.13) shows a very similar profile in the C-N region (1000 - 1600 cm^{-1}) compared with that of PTI.LiCl. The peak positions are similar with only small variations, however there is some variation in peak intensity and sharpness as also seen for IF-PTI (Figure 4.5). This is a clear indication that the C-N PTI framework has not been significantly damaged or disrupted. However there is a significant difference in the N-H bonding region from other PTI materials. New peaks are observed at 2750, 2880, 3030 and 3470 cm^{-1} along with peaks at 3210 and 3360 cm^{-1} which are associated with PTI.LiCl. The positions of these new peaks match very well with those reported for the high pressure synthesis of PTI.HCl.[129, 130] These are assigned to different N-H vibrations from several the bridging N-H group and the protonation of the in-ring nitrogen. A hydrogen bonding interaction is possible between this in-ring N-H site and the Cl$^-$ ion, suggested to be the cause of the vibration at 3030

cm^{-1}.[129] The peaks at 2700 – 2900 cm^{-1} are typically too low to be associated with N-H stretching. Zhang *et al.*[129] ruled out that these peak being associated with C-H vibrations using ^{13}C CP/MAS NMR. With a high degree of hydrogen bonding it is possible that these vibrations are due to N-H stretches, with the hydrogen possibly being associated with the nitrogen lone pairs on two adjacent rings.[129] Zhang *et al.*[129] and McMillan *et al.*[130] also report several smaller peaks at ~3030 cm^{-1} though the intensity appears lowers than in Figure 4.13.

4.3.5 Summary

Section 4.2 showed that the IF-PTI could intercalate LiBr and LiCl. This section has shown that the IF-PTI framework is also able to intercalate HCl. This is particularly interestingly as it resulted in the first low pressure synthesis route of a PTI.HCl. This has shown that through a short series of simple synthetic steps that a PTI materials can be modified and then intercalated with different species to form different structures which may not be easily synthesised directly. I suggest that method could be expanded to a wide range of intercalants allowing for the formation of a family of materials all based on the PTI framework though with different structures.

4.5 UV spectra of the different intercalated PTI materials

4.4.1 UV spectra and analysis

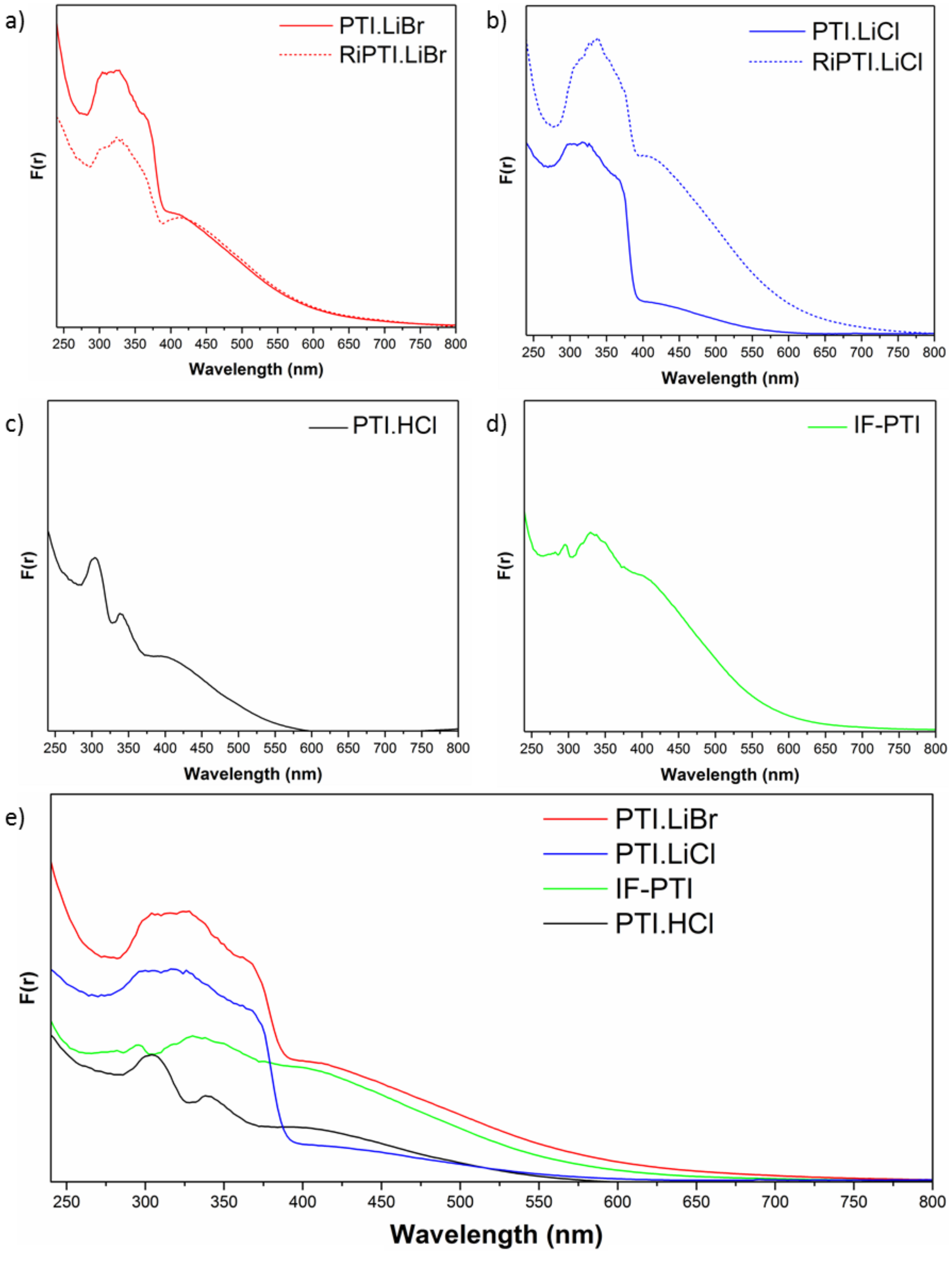

Figure 4.14. UV spectra calculated using the Kubelka-Munk function of different PTI materials. a) PTI.LiBr and Ri-PTI.LiBr. b) PTI.LiCl and Ri-PTI.LiCl. c) PTI.HCl. d) IF-PTI. e) Comparison of PTI.LiBr, PTI.LiCl, IF-PTI and PTI.HCl.

The UV-Vis profiles of PTI.LiBr and PTI.LiCl (Figure 4.14a,b) appear almost identical with a long onset starting at 650 nm with a maxima at 420 which has previously been assigned to n to π* transitions in other carbon nitride based material.[40, 155] A second larger peak with a much steeper onset is observed, this broad peak appears to have two maxima, one at 370 nm and the other at 320 nm. Broad features at this wavelength has been assigned to π to π* transitions for related carbon nitride materials.[40, 155] The n to π* transitions involve the lone pairs located on nitrogens in the triazine rings,[40] these transitions are forbidden for perfectly planar and symmetrical layers.[36, 40] DFT calculations suggests buckling and loss of symmetry result in a distortion of the perfect carbon nitride structure, which allows the n to π* transitions occur more frequently.[40] The identical peak positions and onsets for the PTI.LiBr and PTI.LiCl indicating that the halide does not play a significant role even though the chlorine 2p electrons are expected to occupy the highest energy level of the valence band,[38, 40] this likely due to the intercalated halides being spatially isolated from the rest of the carbon nitride structure and therefore not able to play a significantly role in photoabsorption as previously suggested by McDermott *et al.*[38] The UV-vis spectra shown for PTI.LiBr and PTI.LiCl are similar to those previously reported for PTI materials by Schwinghammer *et al.[153]* and Bojdys *et al.*[149] However these reports only extend as far as 350/400 nm and show the broad n to π* transitions and the onset of the π to π* transitions so direct comparison is difficult.

The Ri-PTI.LiCl and Ri-PTI.LiBr show the same broad π to π* transitions feature, but they both show a more pronounced n to π* transitions compared to PTI.LiCl and PTI.LiBr. This could be due to the re-intercalation process not reintroducing the intercalants and in particular the lithiums identically. The re-intercalation method is exposing the IF-PTI to molten LiX/KX, however it is unclear if this re-introduces both lithium position or only that associated with the lithium halide. A degree of inhomogeneity of the lithium content across the layers may result in some disruption and asymmetry of the carbon nitride layers of the Ri-PTI.LiX.

The UV-vis spectra of PTI.HCl (Figure 4.14c) shows some similarities to but is distinctly different from those of PTI.LiCl and PTI.LiBr, the n to π* transitions are observed at the same wavelength however instead of a broad peak the π to π* transitions in PTI.HCl have two clear maxima at 300 and 340 nm. In the PTI.LiCl electronic structure paper by McDermott *et al.* it is reported that the intercalated lithium is causing splitting of the nitrogen valence band maximum states. This is due to partial replacement of hydrogen with lithium on the imide links, which in turn causes increased hybridisation with the chlorine 2p orbitals.[38] This splitting has the effect of increasing the band gap, however I suggest that the broadness of the π to π* transitions in PTI.LiCl and PTI.LiBr is due to these overlapping split orbital causing a broad superposition with several maxima. In the UV-vis spectra of PTI.HCl two sharp peaks are observed in the same part of the UV region as the PTI.LiCl π to π* transitions, since there is no intercalated lithium there is no splitting of the nitrogen valence band states, hence the relative sharpness of the observed peaks in PTI.HCl compared to PTI.LiCl.

The UV-vis spectra of IF-PTI (Figure 4.14d) shows a strong n to π* transition peak, two broad weak features are observed with maxima at 340 and 290 nm, these are relatively weaker than those observed for all other PTI materials. The maxima of the two peaks in IF-PTI are shifted to a lower wavelength compared to PTI.LiCl suggesting the π to π* transitions are occurring at a higher energy. This is in agreement with McDermott *et al.*[38] who reported that a PTI material without the intercalated ions would have a 0.6 eV larger band gap than PTI.LiCl. However IF-PTI has been shown to have intercalated water which was not taken into account by structure modelled by McDermott *et al.* so direct comparison between the two is difficult.

4.6 Conclusions

Within this chapter it has been demonstrated that the carbon nitride framework of PTI is robust enough to allow removal and re-intercalation of a variety of different. This is clear from the extensive PXRD and XPS investigations that the washing and intercalation procedures occur without damage to the PTI framework. Interestingly the structure of PTI seems to act as a molecular sponge and absorbs water from the air up to 9 % of its weight. This remarkable absorption is entirely reversible when heated under reduced pressure, the dry IF-PTI can be reformed with any notable change to the crystal structure or carbon/nitrogen environments. The first low pressure synthesis of PTI.HCl was performed by intercalating the IF-PTI with HCl. This was only possible due to the removal of the previous intercalants. Using this method it is possible a large number of different PTI based materials with different intercalants could be synthesised. The intercalates have a significant effect on the structure and properties of the layered carbon nitrides, this allows for significant tuning of the electronic properties, which is highly beneficial as carbon nitrides are explored as a potential photocatalyst. This methodology may facilitate the fine-tuning and optimisation of carbon nitrides for a number of applications.

Chapter 5 – Exfoliation of PTI in aprotic polar solvents

5.1 Introduction

Exfoliation followed by dissolution or suspension of layered bulk crystalline phases is key to preparing and manipulating the layered nanomaterials in the laboratory and industrial scale. Techniques leading to liquid phase exfoliation typically involve either chemical functionalisation or sonication processes, both of which can introduce defects and cause damage to a crystalline structure. These methods also often result in suspensions of damaged particles of various sizes that are usually removed and sorted by successive ultracentrifugation steps.[156-161] If an exfoliation method allows a crystalline layered material to be exfoliated into solution without suffering any damage, then it could easily be used to design nanomaterial with tuneable properties and allow their preparation on an industrial scale. This process could then be used to print films of this materials as well as be combined with other solutions to assemble composite membranes or films that could be of great use in a various applications.[162, 163] Methods avoiding ultracentrifugation steps would be highly beneficial for scalability. The overriding aim of this section was to explore exfoliation and dissolution routes to obtain undamaged layers of PTI materials. This chapter showed that PTI spontaneously dissolves in polar organic solvents to form few layer stacks of crystalline nanosheets.

5.1.1 Exfoliation of PTI materials

The first reported exfoliation of PTI was in 2013 by Bojdys *et al.*[149] who reported a method based on intercalation by potassium followed by exposure to water. The intercalated potassium was reported to react with the water forming KOH and hydrogen. The evolved gas then pushed apart the layers, causing them to exfoliate into water. This method of exfoliation following alkali metal intercalation has been widely applied to other layered nanomaterials.[127, 164, 165]

The only other PTI exfoliation was reported by Schwinghammer *et al.*[153] who sonicated PTI in water for 15 hours. The resulting suspension was centrifuged in several steps to remove unexfoliated PTI in and deposit the nanosheets. AFM and TEM images of materials deposited from the supernatant showed several nanosheets of PTI grouped together with heights of ~3 nm.

5.2 Exfoliation of PTI.LiBr via alkali metal intercalation

5.2.1 Vapour intercalation of potassium followed by exfoliation in water

I repeated the experiment of Bojyds *et al.*[149] to further investigate the resultant ‘exfoliated’ sample. PTI.LiBr (104 mg) was heated to 150˚C under reduced pressure to remove any absorbed water or oxygen, this was then placed under inert atmosphere. The PTI.LiBr was then loaded into a quartz glass ampoule with solid potassium (101 mg) under inert atmosphere, this was then evacuated to 10^{-6} mbar with a turbo pump. The valve between the ampoule and turbo pump was closed to form a static vacuum in the ampoule, this was then heated to 200 ˚C overnight. The mass of potassium I used was significantly reduced (though still in excess) compared to that reported by Bojyds *et al.*[149] since 3g of potassium was considered dangerous and unnecessary to have that high of a ratio of potassium to PTI.LiBr.

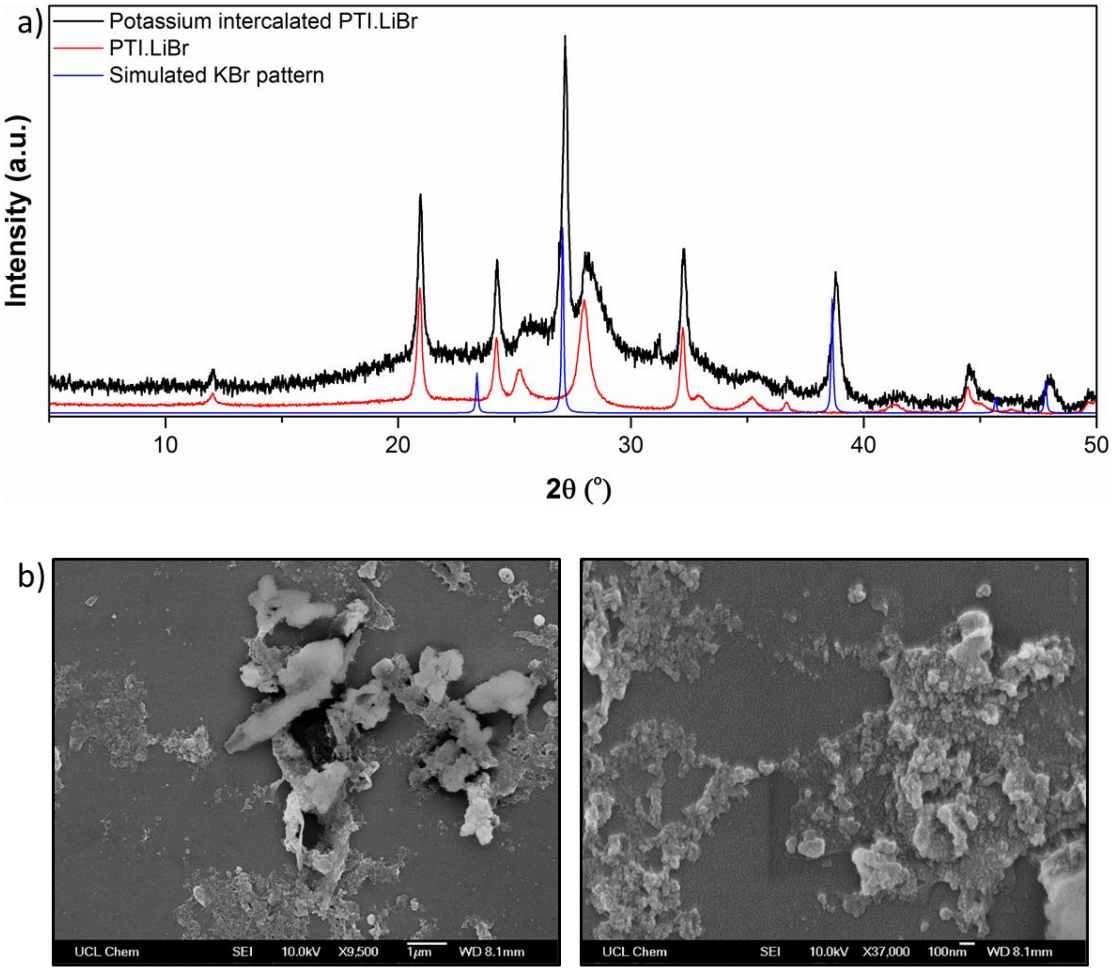

Figure 5.1. PXRD patterns and SEM images of potassium intercalated PTI.LiBr. a) PXRD pattern of potassium intercalated PTI.LiBr compared with PTI.LiBr and simulated KBr. b) SEM images of 'exfoliated' potassium intercalated PTI.LiBr.

Following intercalation of potassium a slight colour change in the PTI.LiBr was observed to a lighter brown colour. In addition some of the ingots of unreacted solid potassium were clearly visible. XRD patterns of the potassium intercalated PTI.LiBr were taken without exposing the material to air (Figure 5.1a). These clearly match well with the PXRD pattern of PTI.LiBr (Figure 3.3). The weak additional peaks can be assigned to KBr salt,[116, 147] though the position of these appear to have shifted to a slightly higher 2θ and the expected peak at ~24˚ 2θ is not observed. PXRD patterns of bulk PTI.LiBr showed significant amounts of residual KBr, and from this it is clear that the potassium vapour intercalated into the PTI layers and reacted with the halide to form KBr.

The potassium intercalated PTI.LiBr was added to distilled water, and evolution of gas was observed. Several drops of the resulting suspension was placed on a glass slide and dried at 80ºC on a hotplate, and observed with SEM (Figure 5.1b). The SEM images clearly resemble those shown in the bulk structure material (Figure 3.10). However it would appear that while some of the micron sized blocks and needles have been broken up, the majority of the material is still in clusters and have not formed individualised crystallites. Given the small size of the observed PTI.LiBr flakes in the bulk (Figure 3.10) any nanosheets may not be observable by SEM. So while it is possible that this method has resulted in the formation of some nanosheets most of the material has remained largely unaffected. This harsh attempted exfoliation method left a light brown suspension of PTI material in water, after several weeks solid material precipitated and the dispersion became clear but with a pale yellow colour.

The reported TEM and SEM images of Bojyds *et al.*[149] show large micron sized flakes of 'PTI.LiBr' and 'exfoliated PTI'. Given that all previous reports of PTI materials have reported 50 – 200 nm crystallites, it is unclear why these micron sized flakes are observed. These reported images are notably similar to those reported by Algara-Siller *et al.*[41] a year later for a related carbon nitride material called TGCN, that can be synthesised in small quantities in conjunction with PTI. It is possible that these images show the reported TGCN material not PTI.LiBr.

5.2.2 Lithium metal intercalation via liquid ammonia and exfoliation in organic solvents

It is clear that while the vapour intercalation of potassium method of exfoliation is a relatively simple synthetic method and is capable of breaking up the larger PTI structures to the some extent. It is not capable of truly exfoliation PTI down to a few layers thickness. The formation of KBr during the synthesis shows that alkali metal and halide ions are capable moving between the layers.

After the negative result of the previous section the methods developed by Fogden *et al.,*[118] Cullen *et al.*[127] and others[118, 119, 127] were employed. These authors' first intercalated nanotube assemblies with alkali metal ions dissolved in liquid ammonia, resulting in the transfer of charge onto these carbon materials, forming 'nanotubide' anions. When they are exposed to organic solvents in an inert atmosphere these charged materials dissolve, resulting in stable solutions of charged nanomaterials. Cullen *et al.*[127] extended this process to charge and exfoliate dichalcogenides into organic solutions. The process occurred spontaneously with no required mixing or sonication steps. I attempted to apply this method to our PTI materials with the aim of forming nanomaterials deposited in solution.

5.2.3 Experimental method and initial observations

PTI.LiBr (150mg) was heated to 150˚C under reduced pressure to remove any absorbed water or oxygen, this was then placed under inert atmosphere and transferred to a glovebox. Solid lithium metal (6.6 mg) was added to the dried PTI.LiBr in a pre-baked quartz ampoule which was placed under a 10^{-6} vacuum on a turbo pump for several hours. This was then cooled to -63˚C and ammonia was condensed into the tube. This was left for several hours until the colour of the ammonia had changed from dark blue to brown. The ammonia was then condensed back into the storage bottle and the resultant material was placed back into the glove box. Aliquots of this material were separated into several vials and several different solvents were carefully dripped onto the samples. Solvents included including dimethylformamide (DMF), N-methyl-2-pyrrolidone (NMP), dimethyl sulfoxide (DMSO) and tetrahydrofuran (THF).

In parallel with this synthesis a control procedure was carried out using PTI.LiBr powder that had not been exposed to the alkali metal/liquid ammonia solution was placed in contact with the same solvents in the same inert atmosphere. It was hypothesised that given the intrinsic intercalation of the PTI.LiBr it could potentially dissolve as is. The solutions were left undisturbed within a glovebox for two weeks. Remarkably both the liquid ammonia route and the control procedure showed a distinct colour change in DMF, NMP and DMSO, with DMSO having the most intense colour. Even more remarkably, it was found that the solution in the control experiment showed a much stronger colour change over the same time period. Since the colour change was much more significant and the method was significantly easier decided to continue our dissolution-exfoliation studies via the ‘control’ route, that simply uses bulk PTI.LiBr in contact with the solvent. These experiments are discussed in detail later. Interestingly, the control solutions showed the same colour change in the organic solvents in air as in inert atmosphere, suggesting that this dissolution may not follow the same layer charging mechanism as reported by Cullen *et al.* which crashed out in air.

I then investigated two different methods that were used in the dissolution studies of PTI, the first was attempting to exfoliate PTI with a sonic probe and the second was following the spontaneous exfoliation as mentioned above. Both of these methods occurred in the same polar organic solvents and were compared to the see if either method was superior to the other.

5.3 Dissolution of PTI.LiBr via sonication in aprotic polar solvents

A commonly used technique for the exfoliation layered materials is ultrasonication. This is argued to exfoliate via generation and collapse of cavitation bubbles force the layers apart.[113] This has been shown by Schwinghammer *et al.*[153] to exfoliate to some degree the PTI material in water. Coleman *et al.*[125] have shown that when sonicated in certain solvents such as NMP layered materials such as transition metal dichalcogenides can be exfoliated. The layered carbon nitride backbone structure of PTI.LiBr is roughly analogous to the other layered materials that have shown to be exfoliated using these aprotic polar solvents, I decided to test if I could form PTI solutions in aprotic polar solvents via sonication.

5.3.1 Experimental methods and observations

Dried PTI.LiBr (~20 mg) was added to anhydrous NMP, DMF and DMSO (~10 ml), these were sonicated using sonic probe at 40 % power for 15 minutes. Sonication induced an immediate change forming a dark brown suspension in all solvents, these slowly changed to a light yellow colour after the suspended powder was left to settle. The suspensions were centrifuged at 4500 rpm for 10 minutes and then at 13000 rpm for 10 minutes to remove large aggregates that had not already settled out. A clear light yellow dispersion was recovered for DMF, NMP and DMSO, compared to the non-sonicated samples all the solutions had less intense colour. I also observed that NMP rather than DMSO was the most intensely coloured of the sonicated solutions (Figure 5.2).

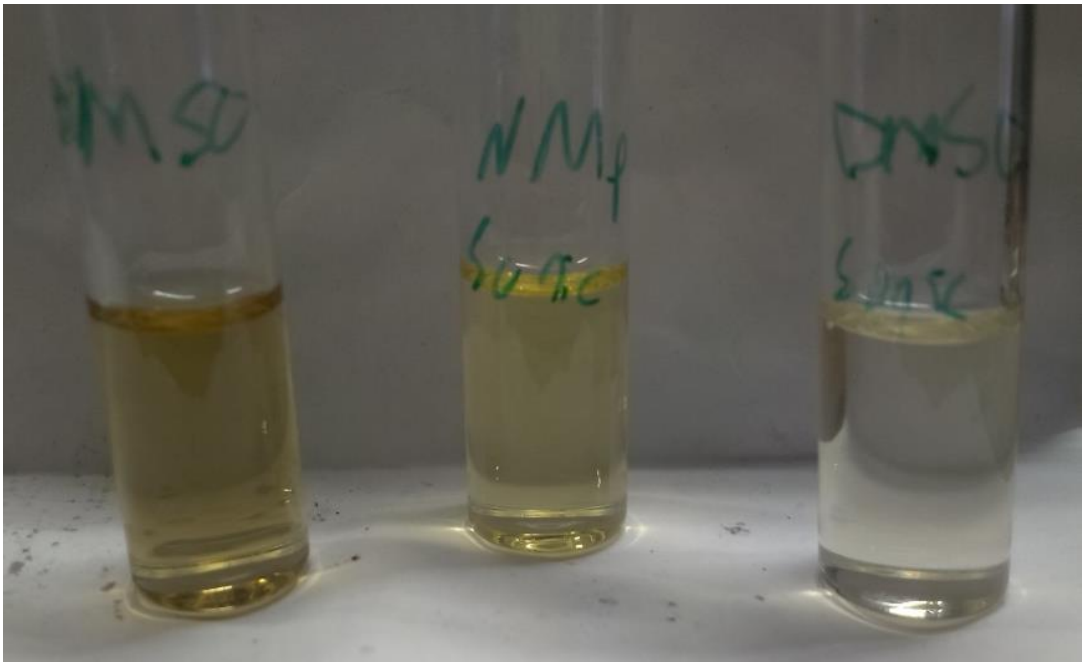

Figure 5.2. Photograph of PTI.LiBr solutions, Left: Non-sonicated DMSO solution, Middle: Sonicated NMP solution, Right: Sonicated DMSO solution.

5.3.2 Characterisation of deposited nanosheets

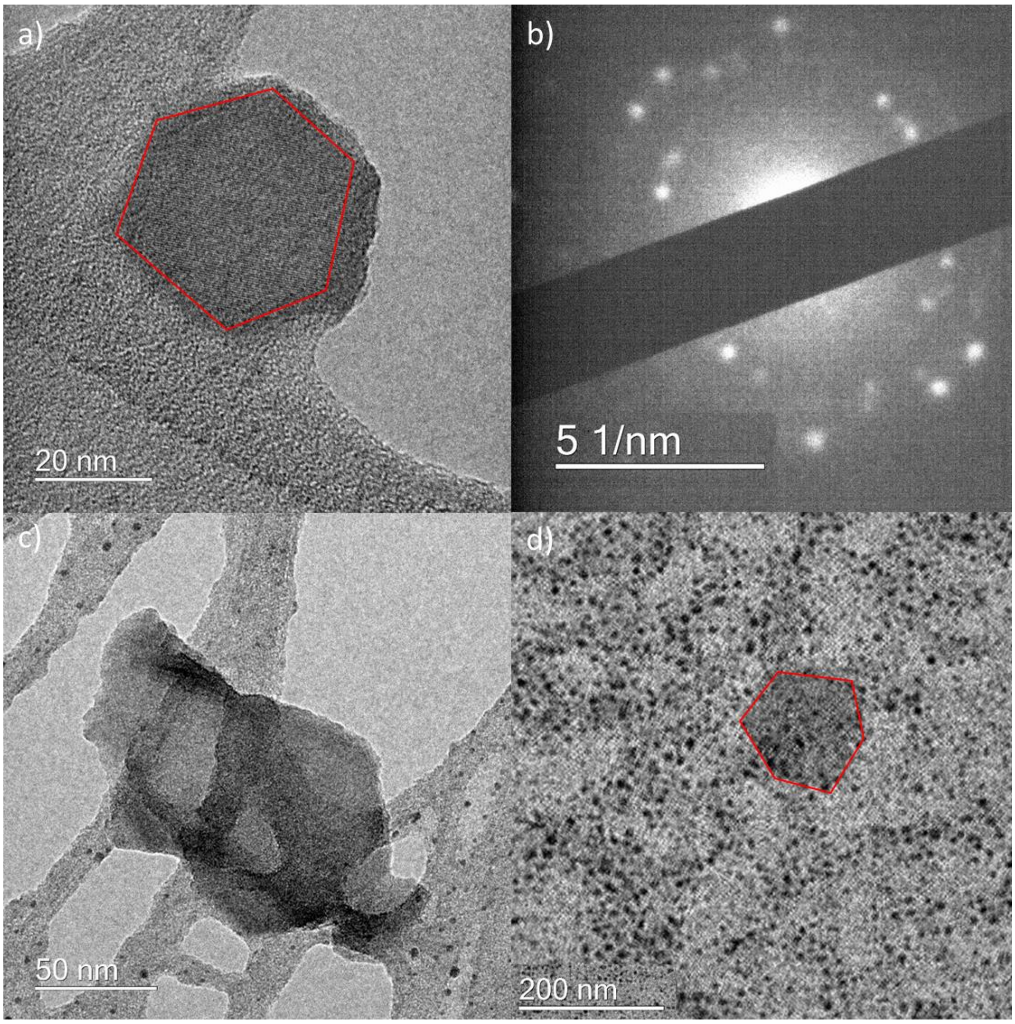

Figure 5.3. TEM and SAED images of sonicated PTI.LiBr dispersion after being dried onto a TEM grid. a) TEM image of PTI.LiBr flake from a DMF dispersion. b) SAED image of the PTI.LiBr flake from a DMF dispersion. c) TEM image of PTI.LiBr flakes from a NMP dispersion. d) TEM image of PTI.LiBr flake and some debris from the NMP dispersion.

A few drops of the centrifuged suspensions were dried onto TEM grids. With these high boiling solvents this was achieved by placing the TEM grid on a glass slide on top of a hotplate. When the hotplate reached 80 ˚C several drops of the solution were dropped onto the grid. The samples were imaged on a JEOL JEM-2100 200 kV TEM (Figure 5.3a,c,d), clearly showing a thin isolated hexagonal crystallite. These 50-150 nm hexagonal crystallites are identical to those observed in the SEM images of the bulk

PTI.LiBr (Figure 3.10). SAED of this area (Figure 5.3b) shows two series of bright diffraction spots that appear to be from the same type of unit cell but slightly misaligned. This suggests that while the stack of flakes in figure 3.5d appears to be a single hexagonal prism it is likely formed from two different crystallites with slightly different orientations. Figure 5.3a suggests that some PTI.LiBr has been exfoliated via probe sonication in aprotic polar solvents, and that this exfoliation has resulted in isolated crystallites, of unknown thickness. In contrast figure 5.3c shows a less perfect hexagonal crystallite that appears to be folded on its upper left side and has clear frayed edges, suggesting that is has suffered some damage from the high energy sonication process. I also observe a significant number of dark spots covering the surface of the TEM grid (Figure 5.3c,d) as well as patches of slightly lighter material dispersed across the grid (Figure 5.3d). It is unclear if these are due to the sonication process creating small broken up pieces of carbon nitride material, or if the solvent has also been affected by the sonication process.

While some isolated hexagonal crystallites are observed it is clear that the sonication process is resulting in the formation of some anomalous material on the surface of the TEM grid as well damage to the flakes.

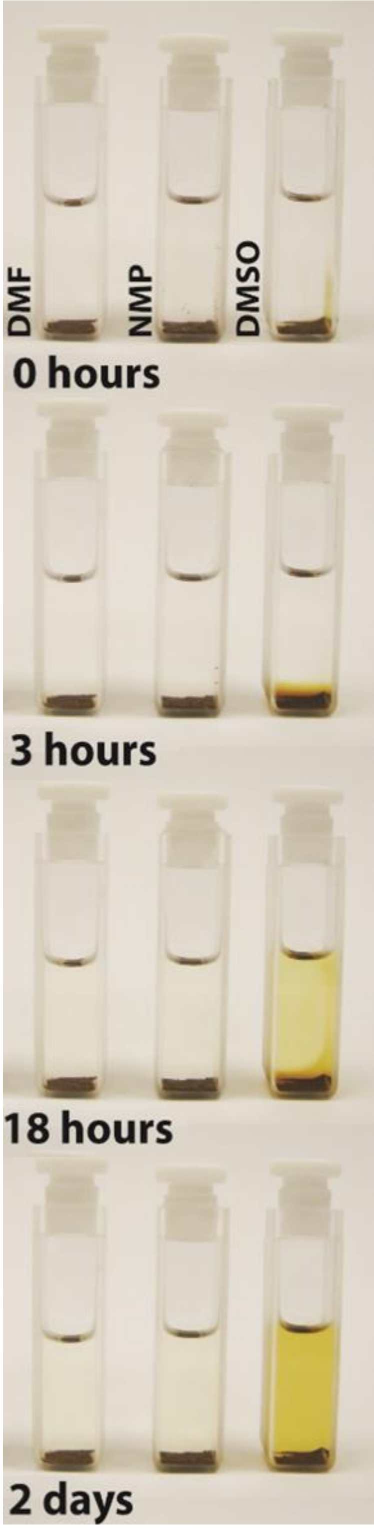

Figure 5.4. Image showing the colour change in PTI.LiBr solutions over 48h. The solvents used at DMF, NMP and DMSO.

5.4 Spontaneous dissolution in aprotic polar solvents

5.4.1 Experimental methods and observations

As shown in figure 5.2 it is clear that sonication of the solutions does not yield higher concentrations (as observed by the colour change of the solution) compared to simply contacting the PTI.LiBr with the solvent. This interesting observation contrasts with the general assumption in the literature that sonication is necessary for the exfoliation process.[70, 115, 125, 164] Given that the observed colour change when PTI.LiBr was put into contact with the same organic solvents was more intense than using a sonic probe, it seems that the dissolution mechanism is more complicated than simply breaking apart the blocks of nanomaterials that are then suspended in the liquid as is typically reported for exfoliation of carbon nitrides. This process required no mixing or sonication and hence I will be referring to it as spontaneous dissolution. A variety of solvents were investigated including water, acetonitrile, benzonitrile, hexane and IPA to see if they had a similar effect on PTI.LiBr. However it was found that only DMSO, DMF, NMP and dimethylacetamide (DMAc) produced a notable colour change in solution (Figure 5.4).

In a standard dissolution experiment 20ml of the solvent (either NMP, DMF, DMAc or DMSO) was very slowly dripped down the side of the vial containing the PTI.LiBr (60 mg). Special attention was paid to not disturbing the solid at the bottom of the vial when adding the solvent. After a certain amount of time depending on the solvent a colour change was observed in the solution, typically within a few hours and within several days the colour change had reached its maximum intensity. Figure 5.4 shows the colour change of DMSO, NMP and DMF solutions over 48h hours, clearly showing the unique spontaneous dissolution of PTI, which has been previously reported as ‘insoluble’.[38]

Solutions prepared by spontaneous exfoliation had reached their maximum intensity within a week, the solution was then gently removed with a pipette as to separate the solution from the residual PTI powder without disturbing it. These solutions showed no sign of precipitate formation or colour change even after a year. However those prepared by sonication only lasted several weeks before some solid material aggregated at the bottom of the vials. In addition when I centrifuged solutions prepared by both methods at 13000 rpm the sonicated solutions tended to precipitate out a small amount of solid and form a less concentrated supernatant. The solutions prepared by spontaneous exfoliation showed no precipitate forming after centrifugation at 13000 rpm.

The reported methods for liquid exfoliation of layered nanomaterials typically are reliant upon sonication and centrifugation steps.[70, 86, 153, 166-169] Consequently liquid processing of nanomaterials is often discussed with reference to “suspensions” or “colloids dispersions” rather than dissolution as would be expected in a solution. Although definitions vary colloidal is defined by IUPAC as ‘A state of subdivision, implying that the molecules or polymolecular particles dispersed in a medium have at least in one direction a dimension roughly between 1 nm and 1μm, or that in a system discontinuities are found at distances of that order'.[170] However, colloids are typically taken to be meta-stable dispersions of one phase in another.[167-169] They are typically described as a balance of the repulsive longer range electrostatic forces and shorter range attractive van der Waals forces as described by DVLO theory. [167-169] If the repulsive forces dominate the colloids will be stable for longer periods of time, steric effects can also be used to increase the stability of the suspension. However it has been pointed out that this model starts to break down when the dimensions of the particle in dispersions become comparable to that of the solvent, such as in traditional solutions where solvent-solute interactions define stability.[169] At which point solvent ordering which depends on the hydrogen bonding and steric effects around the particle has significant impact on its stability.[169] This leads to a breakdown of DVLO theory as the interactions between nanoparticles are non-additive.[169] Therefore nanomaterials could be considered a either a solution, a meta-stable colloid or some middle ground between theories governing colloidal dispersions and solutions.

In the present work centrifugation has no observable effect on the spontaneously dissolved PTI samples and they are stable over years, in contrast to the sonicated samples which are a suspension, typically defined by them forming a precipitate over time. From these observations and the spontaneous nature of the dissolution process clearly indicate that the spontaneous dissolution forms true solutions, which indicates a thermodynamic process. The PTI nanosheet solutions do not form due to nanomaterials being sonicated into a solvent and suspended over a certain time period, but rather dissolves without agitation forming a solution without the need for further stabilisation.

An important implication here is understanding "colloids" as stable or meta-stable suspensions is an interpretation that only works for a certain set of nanomaterial dispersions. This interpretation cannot be applied to all nanomaterials, and the universal applications of colloid theory to nanomaterials should be called into question. The importance of defining between these terms is that the science of colloids is typically used in the analysis of nanomaterials, such as is in the interpretation of zeta potential data, though in this case may not correct, as seen Section 5.4.3.

5.4.2 Investigation of different solvents

Apart from the solvents that showed dissolution of PTI.LiBr (DMF, NMP, DMSO and DMAc) many others were investigated and found not to show any colour change over several weeks. These included ethanol, THF, acenonitrile, benzonitrile, hexane, IPA and acetone. The solvents that appear to solubilise PTI.LiBr all have high boiling points contain no exchangeable proton and are polar. However not all solvents that match this description appear to work, including THF which is commonly used for the formation of nanomaterial suspensions.

Several curious effects were observed when forming the PTI.LiBr solutions. While I was unable for the most part to reliably quantify the concentration of the dissolved solutions (See Section 5.4.4), the intensity of the colour change gave us some ability to qualitatively compare the solutions. Typically when the PTI.LiBr is contacted with any of the solvents mentioned above the majority of the PTI.LiBr powder was left un-dissolved at the bottom of the vial. If a lower quantity of PTI.LiBr was contacted with the same amount of solvent then the colour changed in the solution would be less intense. At first taken to mean that the bulk PTI.LiBr has a ‘soluble fraction’ of material that is causing the colour changed in solution. However when the solution was gently removed replaced with ‘fresh’ solvent it again showed the same colour change across the same time period. So the PTI.LiBr does not have a soluble fraction, and it is was found that the concentration of the solution depended on the amount of bulk PTI powder in contact with the solution, even though there is un-dissolved bulk PTI still in contact with the solvent. In addition, if the solution is gently removed from contact with the powder no precipitates forms over the course of years. This is a unique observation and is in contrast to typical dissolution experiments in which a material will dissolve until it reaches its reaches it thermodynamic equilibrium. At this point all the material that can dissolve, will dissolve independently of the amount of undissolved material. Given that this is not occurring in our dissolution experiments it suggests that the undissolved PTI is playing a direct role in the dissolution, and that its activity term in the equilibrium constant may not be equal to 1, as is typical for solids. However it is also possible that an additional reaction between the solid and the solvent is occurring in tandem to the dissolution, which may be affecting the final concentration of the solution, possibly due to exchange of intercalants between the solvent and solid.

5.4.3 Characterisation of the PTI.LiBr solutions

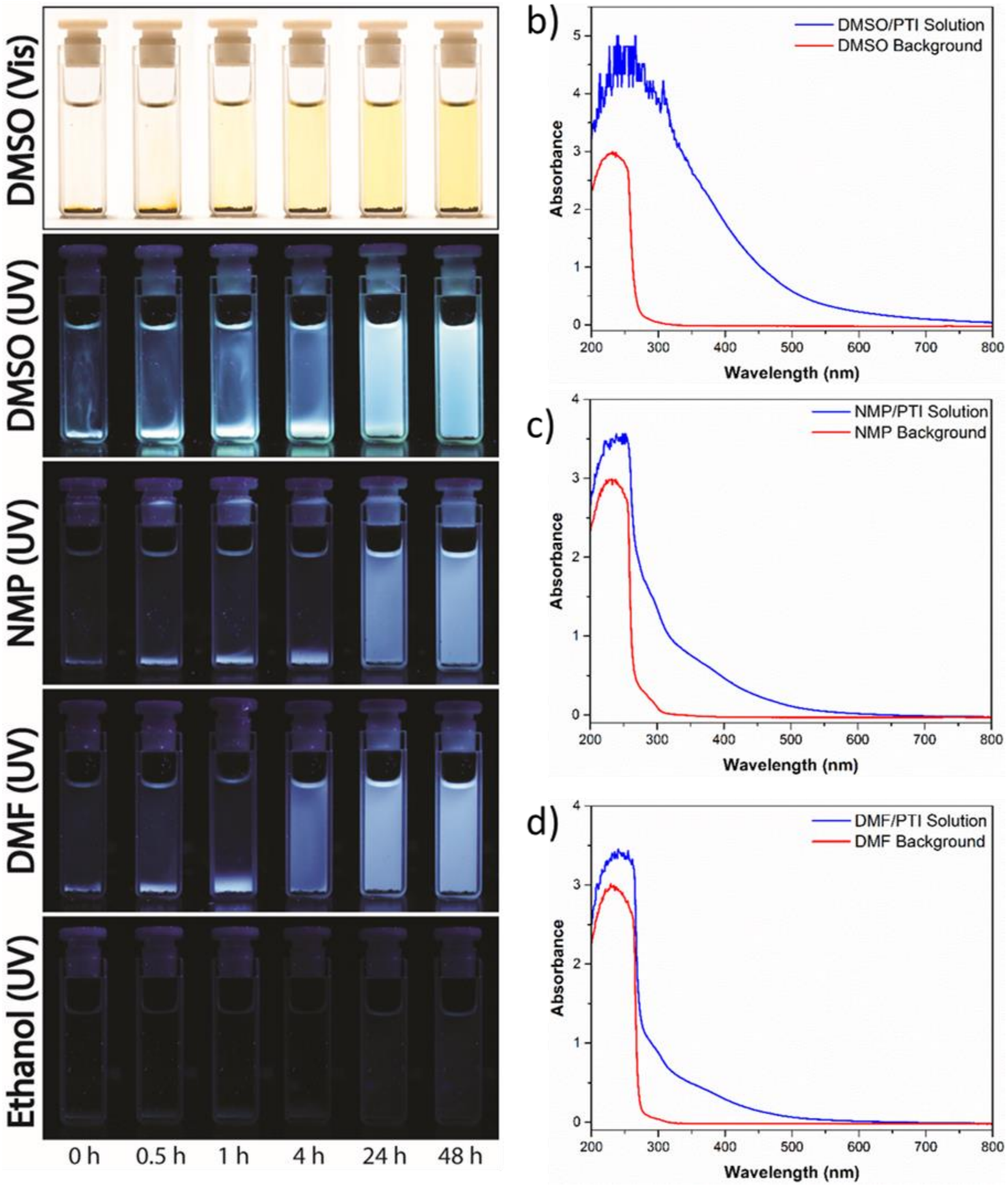

Figure 5.5. Pictures showing the dissolution of PTI.LiBr into different solvents overtime, UV-vis spectra of PTI.LiBr solutions and the solvent background. a) Pictures of the dissolution of PTI.LiBr DMSO, DMF, NMP and ethanol over 48 hours under UV-vis lamp and visible light for the DMSO solution. b) UV-vis spectra of DMSO/PTI solution compared with only DMSO solvent. c) UV-vis spectra of NMP/PTI solution compared with only NMP solvent. d) UV-vis spectra of DMF/PTI solution compared with only DMF solvent.

As I have seen in figure 5.4 there is a distinct colour change when the PTI.LiBr dissolves into solution. Under UV illumination this colour change is even more dramatic (Figure 5.5a). While the PTI.LiBr fluoresces under UV illumination, the PTI.LiBr solutions show a much stronger fluorescence signature, via which I can observe the solvation of PTI.LiBr even more clearly. The bright fluorescence appears as slightly different shades of blue and intensities between DMSO, NMP and DMF. Given that these solutions do not strongly fluoresce under near UV illumination the changing wavelength of fluorescence between each solution is most likely due to differences in solvent-nanosheets interaction. Also shown is the ethanol solution in which no fluorescence is observed.

Tyndall scattering is an effect whereby light is scattered by particle in a dispersion. It is commonly used to show the presence of nanoparticles in solution by shining a laser pen across the liquid and observing the scattering. No Tyndall effect is observed when a red laser pen is used to illuminate the DMSO solution, however under UV lamp illumination Tyndall scattering is observed. Tyndall scattering occurs when particle sizes are on the order of the wavelength.[171] The appearance of this scattering only under UV light (356 nm) is due to the shorter wavelength matching with the small 50-150 nm lateral dimensions of the dissolution PTI crystallites.

Samples were prepared for characterisation by pipetting out some solution near the top of the sample vials to reduce the quantity of large aggregates that would be taken up by the pipette. These were centrifuged at 4500 rpm for 15 minutes and then at 13000 rpm for 10 minutes no material could be seen to be deposited. If the centrifugation step was skipped no significant variation in the solutions was observed. Therefore the centrifugation step was eliminated.

UV-vis spectra of the different PTI.LiBr solutions were taken (Figure 5.5b,c,d) and compared with those of the relevant solvent. All three solvent used have very strong absorbance in the UV region between 200 – 300 nm. As seen in Section 4.5 the UV-vis spectra of PTI materials typically have a slow broad onset from 700 nm to a maxima at 400 nm, a series of more intense peaks at around 300 to 350 nm and an increasing absorption after 250 nm. However due to the detector response becoming non-linear at this absorbance it is difficult to directly compare peaks when the transmitted light is below 0.1% (absorbance over 3), as this starts to approach the equipment limit. This is especially true for the DMSO/PTI.LiBr solution where a significantly higher absorbance peak compared to the background DMSO solvent is observed at ~250 nm. A large absorbance is observed from bulk PTI.LiBr between 200 and 400 nm (Figure 4.14). This suggests a large concentration of dissolved PTI.LiBr. The same peaks are observed in the NMP and DMF (Figure 5.5c,d) both show a higher absorbance in the PTI.LiBr solutions compared to the solvents, a clear indication of dissolution. Of interest is the relatively lower intensity when compared to the DMSO sample, this agrees with the images shown in figure 5.4 which further indicate the DMSO is the most concentrated. The next feature of note is a broad peak at ~310 nm in DMF and NMP solutions. This feature appears to be much sharper in the DMSO solution, only a small absorbance peak is observed in the background solvent in this region. Peaks in this position were assigned to π to π* transitions in the bulk PTIs so this peak can be assigned to PTI.LiBr in solution. Finally a long broad onset for the solutions which is not seen in the solvent backgrounds is observed. This is likely due to the n to π* transitions as discussed in Chapter 4.

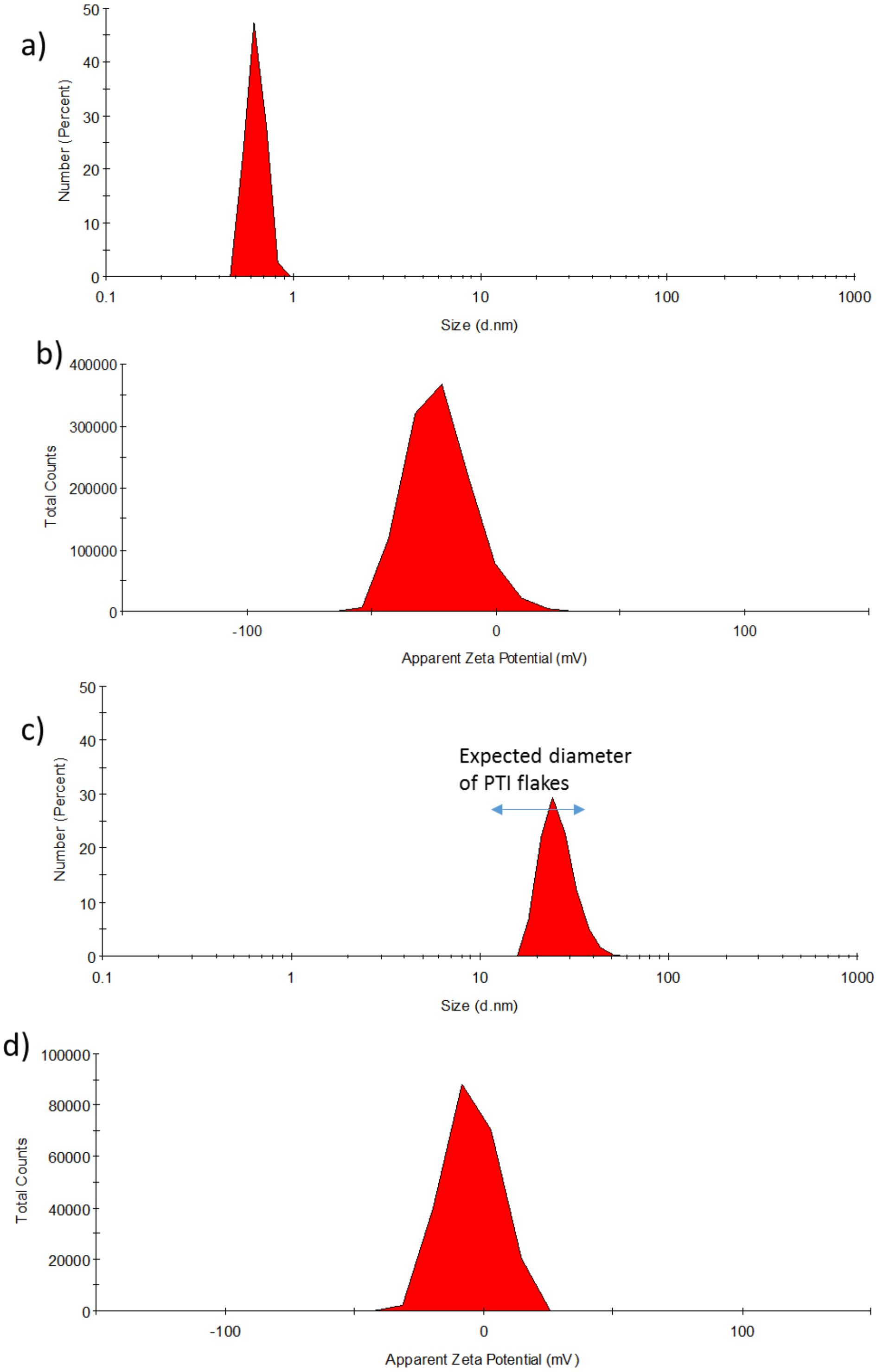

Figure 5.6. Graphs showing the zeta potential and particle size distribution data for PTI.LiBr DMF solutions. a) Particle size distribution graph for the DMF solvent. b) Measured zeta potential of the DMF solvent. c) Particle size distribution graph of DMF/PTI.LiBr solution, highlighted is expected diameter of PTI flakes. d) Measured zeta potential of DMF/PTI.LiBr solution.

Measuring the zeta potential is a common technique used to investigate the charge of molecules, colloids or ions in a dispersion. It is determined by placing a voltage potential across a specially designed cuvette, the speed of the charged particles towards either the positive or negative electrode is measured by laser Doppler electrophoresis. The magnitude of the charge determines the speed of the particle, and a neutral particle would not be expected to show any significant movement. Dynamic light scattering (DLS) is used to calculate the translational diffusion coefficient of the detected particles, apply this value to a spherical particle with diameter dependent on the measured magnitude. DLS assumes a spherical particle, so if the measured particle is a flake its measured translational diffusion coefficient would correspond to a sphere with a diameter smaller than the flakes lateral diameter. Zeta potential measurements are for the most part carried out in aqueous environments, and are by far the most well understood solvent systems.[172] While uncommon, non-aqueous zeta potentials measurements have been reported, typically in polar organic solvents, the changes in dielectric constant and viscosity are taken into account in the zeta potential calculations.[173-176] Zeta potential in non-aqueous solvents have been reported, however the data is limited to giving an indication of the surface charge of suspended colloids.[173-176]

Particle size distribution data for the DMF solvent before the addition of the PTI (Figure 5.6a) shows that it contains nanoparticles smaller than 1 nm across. Given that anhydrous DMF was used and no particles would be expected, I suggest that these small particles are from either the manufacturing or drying process. When the same analysis was performed on the DMF/PTI.LiBr (Figure 5.6c) the only peak that is observed is between 17 – 50 nm. The size of the measured particles is close to but smaller than that observed diameter for the PTI flakes, which were from SEM images of 30 – 180 nm. Given the observance of only PTI flakes in solutions via TEM we suggest that these smaller than expected particles are PTI. The difference between the two values can be explained by the fact that the DLS analysis calculates particle size based on a spherical model.

Typically zeta potential data is analysed using colloid theory in which,[172] the stability of suspended material can be indicated by the surface charge, as uncharged particles would be more susceptible to aggregation. Particles with a zeta potential value around 0 mV may be considered to be unstable and will flocculate. Having a high zeta potential value (e.g. ±50 mV means) they are considered stable, this general rule of thumb type analysis is typically applied for zeta potential measurement of nanomaterials in disperions.[124, 153, 177, 178] Figure 5.6b,d shows the zeta potential data of the DMF solvent and of the PTI.LiBr/DMF solutions. The first thing of note is the presence of some dissolved particles in the solvent that have a zeta potential of -24 mV. These are most likely the 1 nm particles found from the DLS analysis, and since they are not observed in the PTI.LiBr/DMF solution they will not be explored further. For the PTI.LiBr/DMF solution one peak with maxima around -4 mV is observed, this would imply PTI.LiBr flakes have no or little potential at the double layer, and hence would be expected to be an unstable colloid dispersion. Given the observed stability of the solutions I suggest that in this case the colloidal analysis cannot be applied to these materials. These solutions are formed by spontaneous dissolution and I have observed no aggregation of PTI/solvent solutions left over the course two years. This is a strong indication of stability, with no charge and no expected steric effects on the flake not having an apparent effect on their stability. Clearly the PTI solutions cannot be treated as a traditional nanomaterial dispersion and/or colloidal suspension. The zeta potential data and large aspect ratio of the PTI in solution would suggest a significant stabilisation by solvent-solute interactions. As discussed above this places this nanomaterial in a middle ground between colloids and solutions.

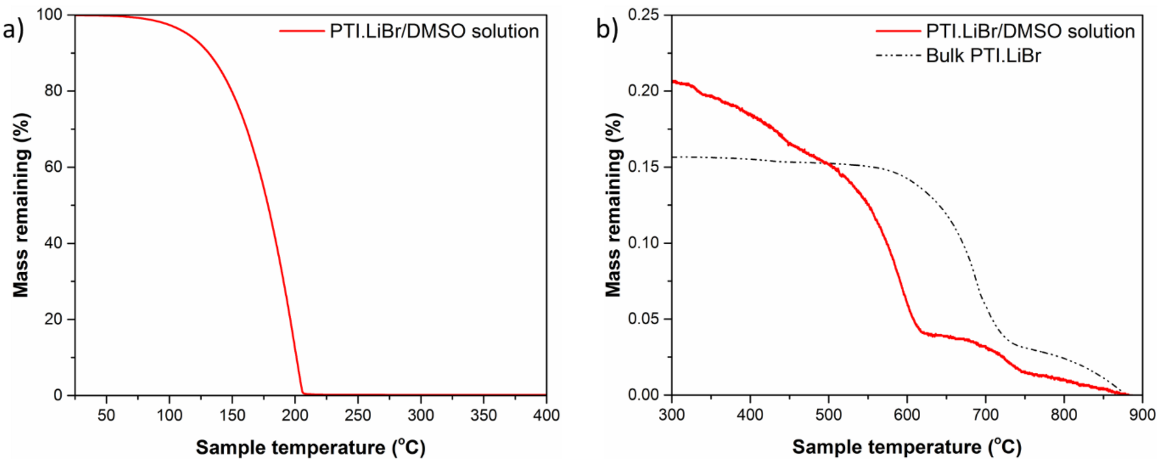

Figure 5.7. Graphs showing the mass remaining as a function of sample temperature of a PTI.LiBr/DMSO solution, calculated via TGA. a) Graph of TGA of PTI.LiBr/DMSO solution showing the loss of the solvent between 100 – 200 ˚C b) Zoom in of the previous graph showing the PTI.LiBr/DMSO compared against bulk PTI.LiBr.

While the UV-vis spectra of PTI.LiBr give us a qualitative indication of the concentration of the different solvents, quantitative assessment is needed to be able to compare our solutions to the scientific literature. To achieve this I ran TGA of the PTI.LiBr solutions (Figure 5.7). Because most of the mass is due to solvent special precautions had to be taken while running the samples to ensure as little instrumental noise as possible, such as the use of a brand new platinum can. Even so these experiments were carried out near the noise limit of the TGA apparatus and day-to-day machine variation often led to some datasets with unacceptably high noise/drift. The TGA data for DMSO/PTI.LiBr solution (Figure 5.10a) shows one major mass loss event between 150 – 200 ˚C. As the boiling point of DMSO is 189 ˚C this peak that represents the loss of over 99% of the weight is due to the evaporation of the solvent. Figure 5.10b shows the expanded area between 300 - 900 ˚C. It is clear that there is a major mass loss between 500 - 600 ˚C and a second event between 600 – 750 ˚C. If the relative intensity and position of these peaks are compared they match closely with the TGA of bulk PTI.LiBr, however these mass loss events occur at ~100 ˚C lower temperature in solution compared to the bulk. I suggest that they have a similar origin. The lower temperature is caused by the smaller crystallite size in the solvated and then dried PTI.LiBr, this size dependence on temperature is a well reported phenomena for nanomaterials.[179-183] Using the known mass of the PTI.LiBr in solution and the TGA of bulk PTI.LiBr the concentration of PTI.LiBr/DMSO solutions was calculated to be ~ 1mg/ml.

5.4.4 Characterisation of the deposited nanosheets

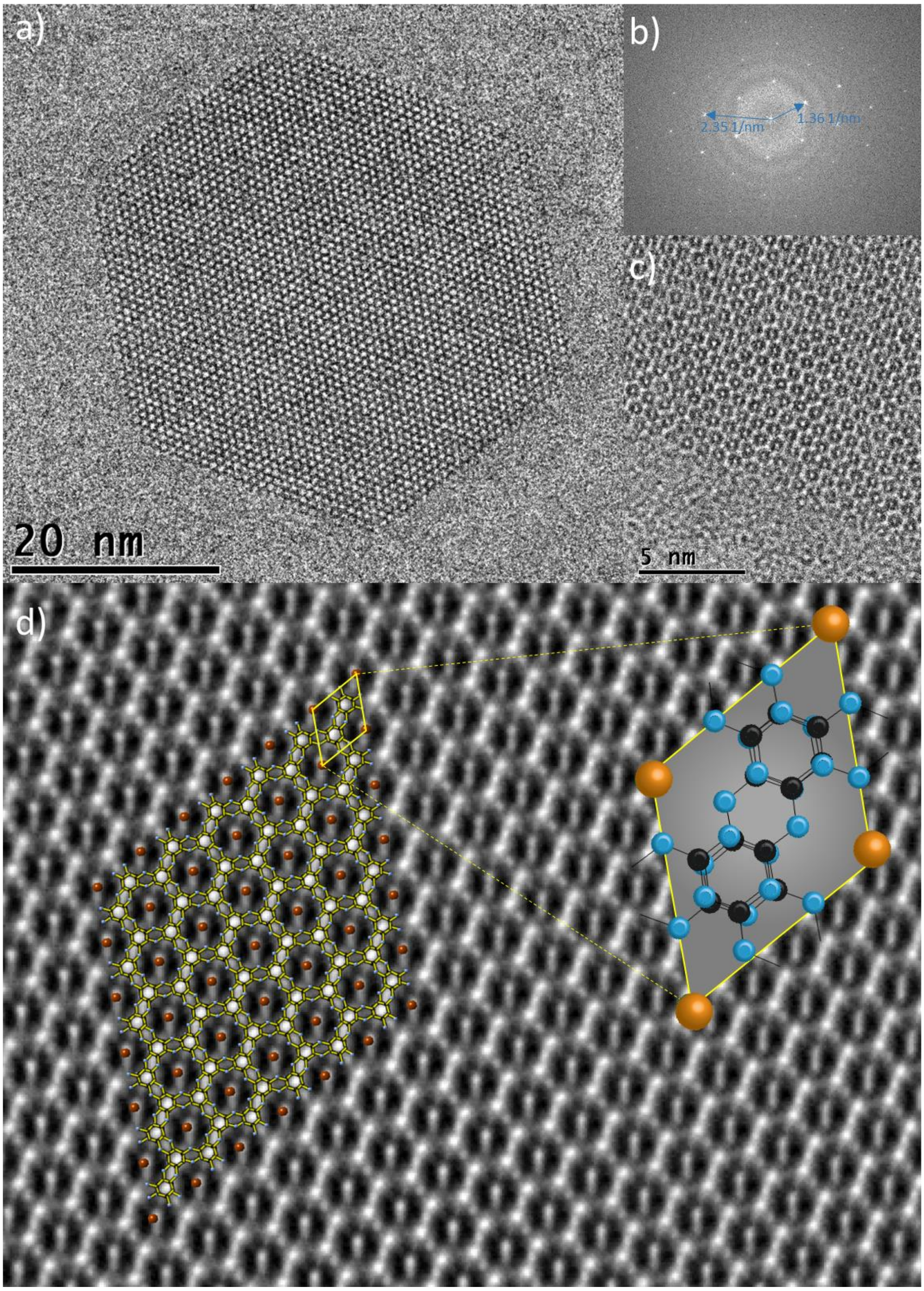

Figure 5.8. High resolution TEM images and Fourier transformed image of PTI.LiBr nanoflakes deposited out of NMP solution. a) HR-TEM image of a crystalline and undamaged PTI.LiBr flake. b) SAED of a flake of PTI.LiBr showing the typical lengths observed for PTI.LiBr. c) Zoomed in image of a, the focus has been changed to clearly show the hexagonal PTI structure. d) Image of c with the carbon background removed, the crystal structure of PTI.LiBr has been overlaid.

An aliquot of the PTI.LiBr/NMP solution was then dropped onto holey copper TEM grids which were placed on a hot plate that was heated to 80 °C, these were then dried at 100 °C under a 10^{-6} mbar atmosphere. These were then imaged using 80 kV TEM on a FEI TITAN. The TEM (Figure 5.8a) image shows an undamaged hexagonal crystallite which is clearly structurally similar to those observed for bulk PTI.LiBr (Figure 3.11). This isolated flake is ~50 nm in diameter, similar to that observed by TEM for bulk PTI.LiBr in Chapter 3. The Fourier transformed image (Figure 5.8b) of this flake matches the structure reported by Chong *et al.*[54] as well as the images observed for PTI.LiBr in Chapter 3 (Figure 3.11). The characteristic distances were measured and they match with the crystal structure of PTI.LiBr (Figure 3.11). In these images I observe isolated hexagonal PTI sheets with no visible damage to the crystalline structure, and there is no indication of any other dissolved nanomaterials deposited onto the grids.

These images clearly show that the spontaneous dissolution method causes no visible damage to the flake and is able to maintain the same in plane unit cell. When imaging the surface of the sample the contrast between the crystallite and the carbon grid is very low due to their similar elemental composition. This is effect is even more severe due to the thinness of the deposited flakes. To enhance our images of the PTI flakes and see the atomic structure the defocus condition was adjusted (Figure 5.8c) and then the amorphous carbon background was removed (Figure 5.8d). These defocused images show, remarkably, the stacks of individual triazine rings arranged in the hexagonal pattern around a bright spot in the centre of the ring. The structure of bulk PTI.LiBr has the bromine lying in the centre of this void between the layers, this halide is the bright spot that is observed in the centre of the rings. Overlaid with this image is the crystal structure of PTI.LiBr, clearly visible are the stacks of triazine rings as well as the bridging amine groups.

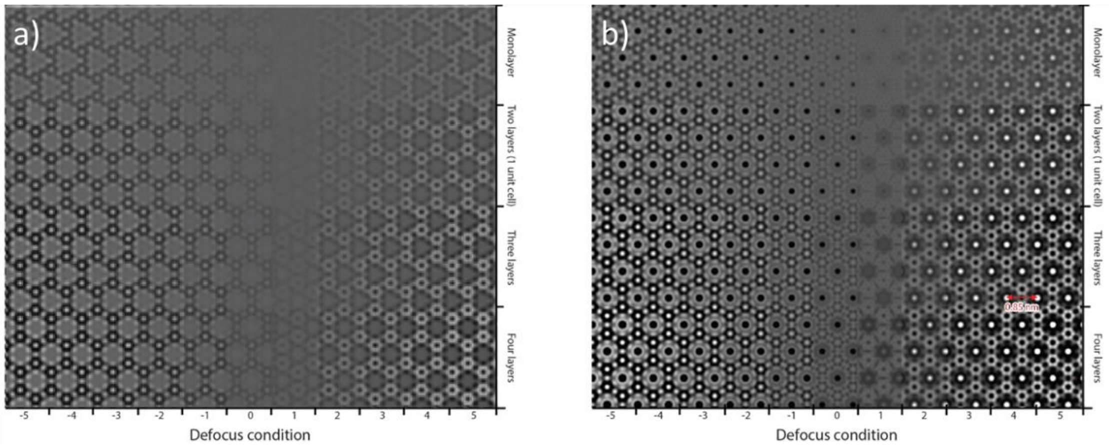
a)
Monolayer
Two layers (1 unit cell)
Three layers
Four layers
-5
-4
-3
-2
-1
0
1
2
3
4
5
Defocus condition
b)
Monolayer
Two layers (1 unit cell)
Three layers
Four layers
0.85 nm
-5
-4
-3
-2
-1
0
1
2
3
4
5
Defocus condition

Figure 5.9. TEM calculated projections of PTI.LiBr under different defocus conditions, layer thickness and halide occupancy. a) TEM projection of PTI.LiBr without intercalated halides. b) TEM projection of PTI.LiBr with intercalation halides.

To confirm if the intercalated halides has remained during the exfoliation, TEM calculated projections of the PTI structure with and without the intercalated bromine were calculated by collaborator Dr Vasiliki Tileli (Figure 5.9a,b). These two images both show the same PTI backbone structure, but clearly the projection with the halides matches significantly better with the observed experimental TEM image due to the bright spots located in the centre of the triazine ring. It is clear then that the intercalated halide and therefore the charge countering lithium ions have remained attached within the structure after the dissolution. What is also amazing is that every single one of these voids appears to be filled with the intercalated halide ions. Also of note is that the TEM projections clearly show that nanosheet stacks that are more than one monolayer thick do not appear different via TEM, and the additional layers serve only to contrast the PTI flakes against the carbon grids and not change the TEM image significantly. The thickness of the deposited sheet could not be determined using TEM. I turned to AFM to access this data.

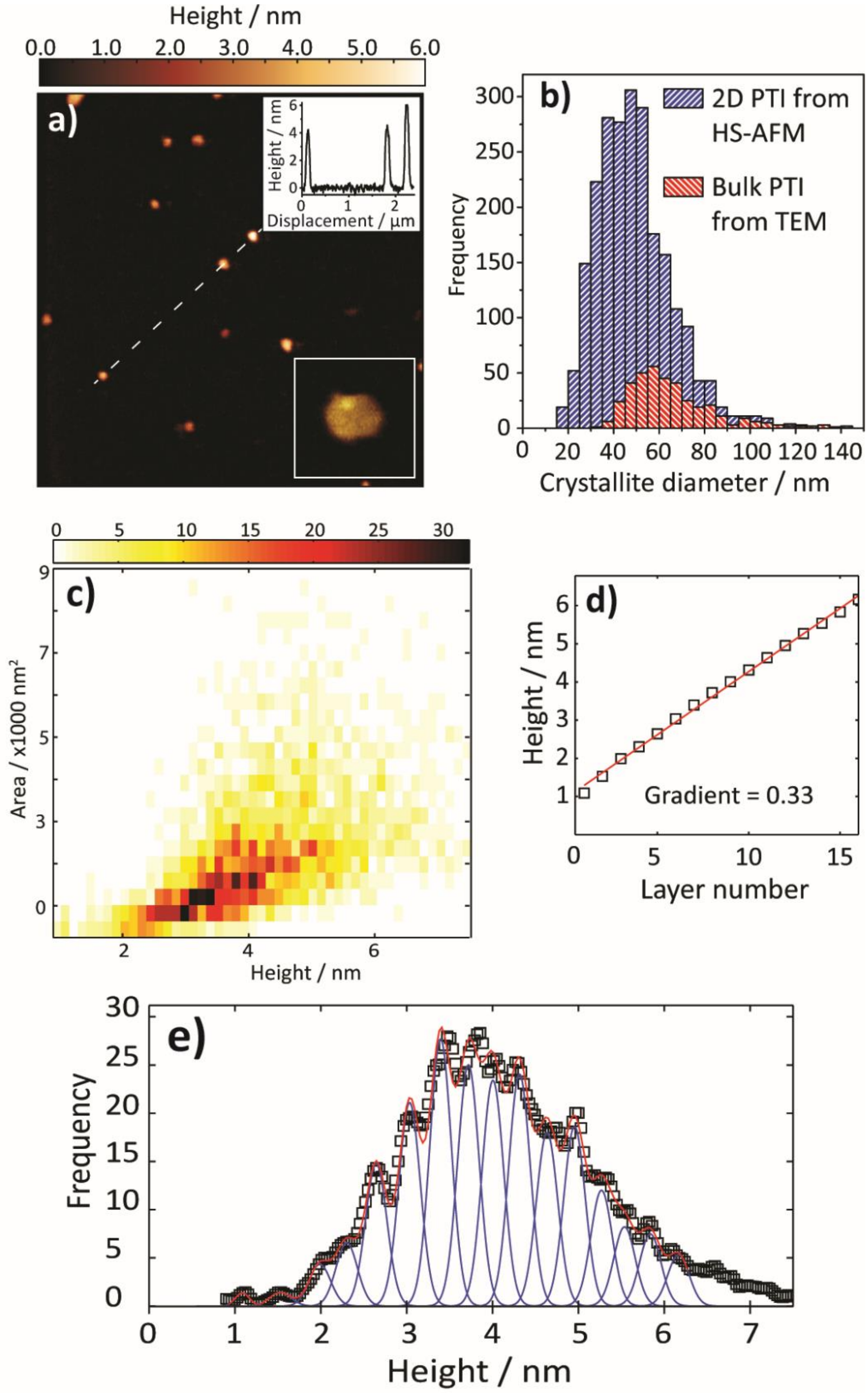

Figure 5.10. AFM characterisation of PTI.LiBr nanosheets deposited from NMP solution. a) HS-AFM image of few-layer PTI nanosheets. b) Histogram showing the distribution of crystallite sizes from both HS-AFM and from TEM. c) Frequency colour map of nanosheets areas (y-axis) and heights (x-axis). d) Histogram of flake area from just under 2400 crystallites. e) Histogram showing the frequency of the heights measured for just under 2400 crystallites, this is fitted with multiple Gaussian peaks each separated by a value close to the interlayer spacing of the PTI.LiBr. f) Peaks heights taken from (i) and plotted as a function of layer number.

The AFM samples were prepared by taking an aliquot of the PTI.LiBr/NMP solution. This was dropped onto freshly cleaved mica which had been placed on a hot plate heated to 80 °C, and then dried at 100 °C under a 10^{-6} mbar atmosphere. Figure 5.9a shows the height data over a small area, in which, I observe several flakes with heights between 2 and 6 nm, a zoom in of one of these flakes clearly shows that is a flat hexagonal flake ~40 nm across. This is exactly what is observed in the TEM images, confirming the presence of exfoliated crystalline PTI.LiBr nanosheets deposited onto the substrate. During observation of the mica substrate only PTI.LiBr was observed, no indication of other materials were found.

Working with collaborators at the University of Bristol, Dr Loren Picco, Dr Oliver D.Payton and Mr Freddie Fussell-Pavier we used a custom made high speed AFM (HS-AFM) system. This enabled us to collect height data over a much larger area of sample in over a much shorter time period (figure 5.9b). This allowed us to measure the heights of just under 2400 PTI.LiBr flakes deposited from solution, and compare their lateral areas against those measured from bulk PTI.LiBr (Figure 3.11). There is a close overlap between these two histograms, though the flake size data from AFM appears to be slightly skewed towards the lower sizes. This indicates that no significant degradation of the crystallite sizes has taken place due to the dissolution process. Figure 5.9c shows the relationship between flake size, height and frequency. These shows a clear trend between flake area and thickness, perhaps indicating that smaller flakes are easier to exfoliate. If the heights of all the measured flakes are plotted as a function of frequency (Figure 5.9e) the presence of several peaks within the data can be observed. These peaks can be fit by a series of Gaussian curves that matches well with the experimental data. Each of these Gaussians represents a stack of PTI.LiBr with a different number of layers (Figure 5.9e), the height difference between the maxima of each of the Gaussians is 0.33 nm (Figure 5.9d), close to the measured interlayer spacing of PTI.LiBr of 0.35 nm. There is a clear correlation between of the number of layers per deposited PTI.LiBr stack with the model number being 8 or 9 layers. This remarkable data sets shows that the spontaneous dissolution of PTI.LiBr has led to exfoliation down to only a few layer in thickness, without damaging the material. The first observed Gaussian peak is at 1.1 nm (Figure 5.9d) which is around three times the typical spacing, this increased height is either due to the PTI.LiBr flakes not forming mono/bi-layers and the smallest stack being tri-layers or a significantly increased height caused but the interaction of a mono/bi-layer and the underlying support. Monolayers of graphene are reported to have heights between 0.4 - 1.1 nm[184] and typical interlayer spacing of 0.335 nm. However I suggest that this first Gaussian peak is due to tri/bilayer PTI with the difference in height measured being due to solvent between the mica substrate and the PTI nanosheet.

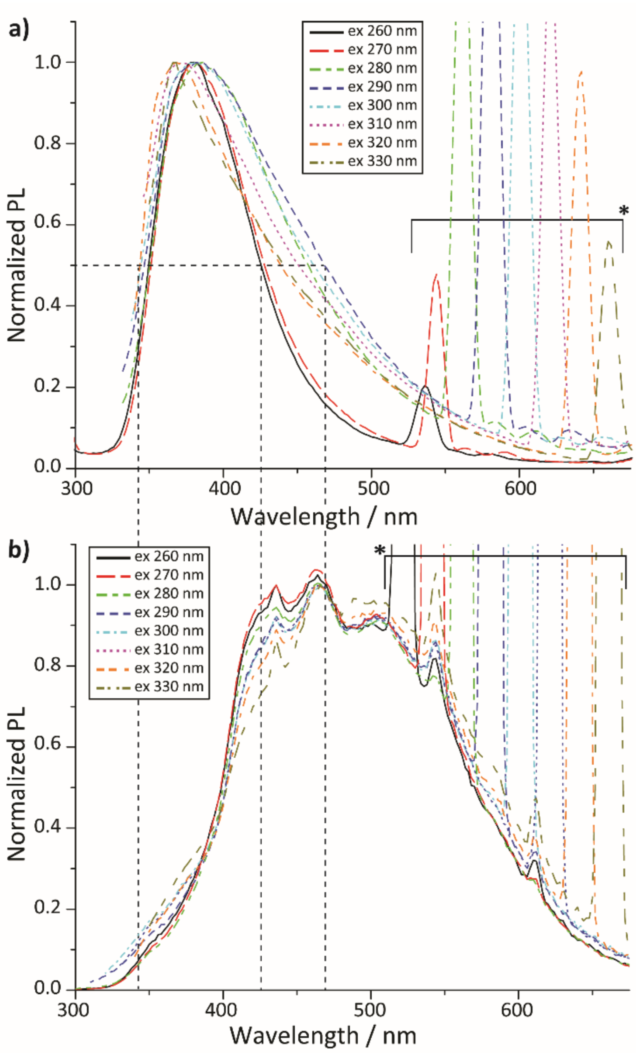

Figure 5.11. Photoluminescence emission spectra of PTI nanosheets obtain with excitation wavelengths between 260 - 330 nm. a) PL spectra with a range of excitation wavelengths of PTI.LiBr/DMF solutions, with the intensity normalised to that at ~ 380nm. b) PL spectra with a range of excitation wavelengths of PTI.LiBr deposited from PTI.LiBr/DMF solutions, with intensity normalised to that at ~ 450 nm. In both spectra the sharp peaks are observed at double the excitation wavelength are instrumental in origin.

PTI.LiBr absorbs mostly in the UV region, and under UV illumination it fluoresces. This has led these materials to be explored for optoelectronic applications.[37, 66, 153, 185-187] Figure 5.5 showed that the PTI.LiBr solutions appear to fluorescence more strongly than the bulk powders. PTI.LiBr/DMF solutions were excited with UV light with wavelengths between 240 – 330 nm, (figure 5.11a).

Typically for carbonaceous nanomaterials a narrow photoluminescence (PL) peak that does not vary between different excitation wavelengths is an indication of crystalline, similar sized materials, emitting over an extended length. [188, 189] A broad peak with a strong excitation dependence would be an indication of a multitude of different chomophores emitting at different wavelengths. Broad peaks could also indicative a range of nanoparticle sizes within a system where quantum confinement could be in effect. [188-192]

The emission spectra using different excitation wavelengths show only a small shift of maxima between 360-380 nm. Apart from a slight broadening in the 280 – 330 nm excitation the peaks are narrow for all wavelengths. Since PTI typically spatially extends over 50 nm I suggest that quantum confinement effects are unlikely to be happening across a single sheet.

The PL of a film of PTI.LiBr by depositing from a solution (Figure 5.11b) was measured by collaborators at Imperial College London, Dr Andrew Telford and Prof Jenny Nelson. The emission spectra now has its maxima at ~ 480 nm, but it has significantly broadened as compared to emission spectra of the solution. This increased broadening of the deposited PTI.LiBr cannot be explained by a large variation in the lateral size of the crystals as the bulk material has shown to have tight size distribution and the same as that in solution. Another explanation of this broadening is quantum confinement effects across several PTI sheets in a single stack, as charge delocalisation between different sheets in a stack is possible and has been suggested previously for carbon nitride.[193, 194] This would be consistent with restacking of PTI.LiBr flakes after they are dried out of solution. Merschjann *et al.* [193, 194] proposed a model for the triazine based C_3N_4 where the amine bridging group breaks the conjugation between each triazine ring, so each acts as an non-conjugated molecule. The π orbitals of triazine rings stacked above and below overlap well with the triazine ring, allowing movement of electrons from one sheet to another. Therefore in a system with a narrow height distribution of stacked sheets such as in solution it is possible that the electrons are confined to only a few layers, while in the bulk PTI.LiBr electrons are not confined and can travel the entire large and varied length of different hexagonal crystal stacks. This leads to a variation in peak broadening and positions between the thin and narrow height range stacks in solution and the thick and varied height stacks in the deposited film. This indicates that the PL wavelength depends on the number of layers in a stack. If the stack height could be controlled to an even narrower region it could be tuned and potentially prove very useful in for UV-blue and white LED emitters.

5.5 Conclusion

It is clear from the characterisation of the solutions that the when bulk PTI.LiBr is contacted with either DMF, NMP, DMSO or DMAc the hexagonal crystallites spontaneously dissolve and exfoliate into the solvent. The spontaneous dissolution of nanomaterials is rare, typically to observe this behaviour the materials have to be charged first. Zeta potential measurements of the dissolved nanosheets indicate they have little to no charge, so the thermodynamically driven spontaneous dissolution has to be caused largely by solvent-nanoparticle interactions. What is also clear from observations of the solutions is that the dissolution process has not affected the crystal structure of the material or introduced any defects. Remarkably this path of forming dissolved PTI flakes in solutions has also caused them to exfoliate into a narrow height distribution of around 9 layers. The concentrations of these solutions are up to 1 mg/ml, which is significantly higher than that reported from sonication studies of PTI.LiCl in water.[153]

Chapter 6 – Spontaneous exfoliation of PTI in water

In Chapter 5 the dissolution and exfoliation of PTI.LiBr in polar aprotic organic solvents was explored. However these solvents have a high boiling point which makes processing them more difficult and most are very toxic, therefore I decided to investigate the possibility of using water as a solvent in these materials.

6.1 Experimental method and initial observations

If PTI.LiBr was contacted with water a slight colour change was observed in solution similar to that of the aprotic polar solvents. This spontaneous dissolution occurred without any stirring, sonication or mixing. This was found to significantly depend on the pH, with the more basic solutions resulting in greater solubility. As with the aprotic polar solvents the concentrations of the prepared solutions were dependent on the initial quantity of PTI.LiBr that was put in contact with the basic water.

In a standard dissolution experiment 20 ml of the water was very slowly dripped down the side of the vial containing the PTI.LiBr (60 mg), special attention was paid to not disturbing the solid at the bottom of the vial when adding the solvent. After a certain amount of time depending on the pH of the water a colour change was observed in the solution, typically within a few days a slight colour change was observed, the solution typically reached its maximum intensity within a few weeks. The slight small colour change to a light yellow colour was observed in solution (Figure 6.1a). As with the aprotic polar solvents the colour change is much more significant under UV-Vis illumination (Figure 6.1b).The Tyndall effect is observed only in the UV illuminated solution, due to its correlation to the size of the PTI.LiBr crystallites.

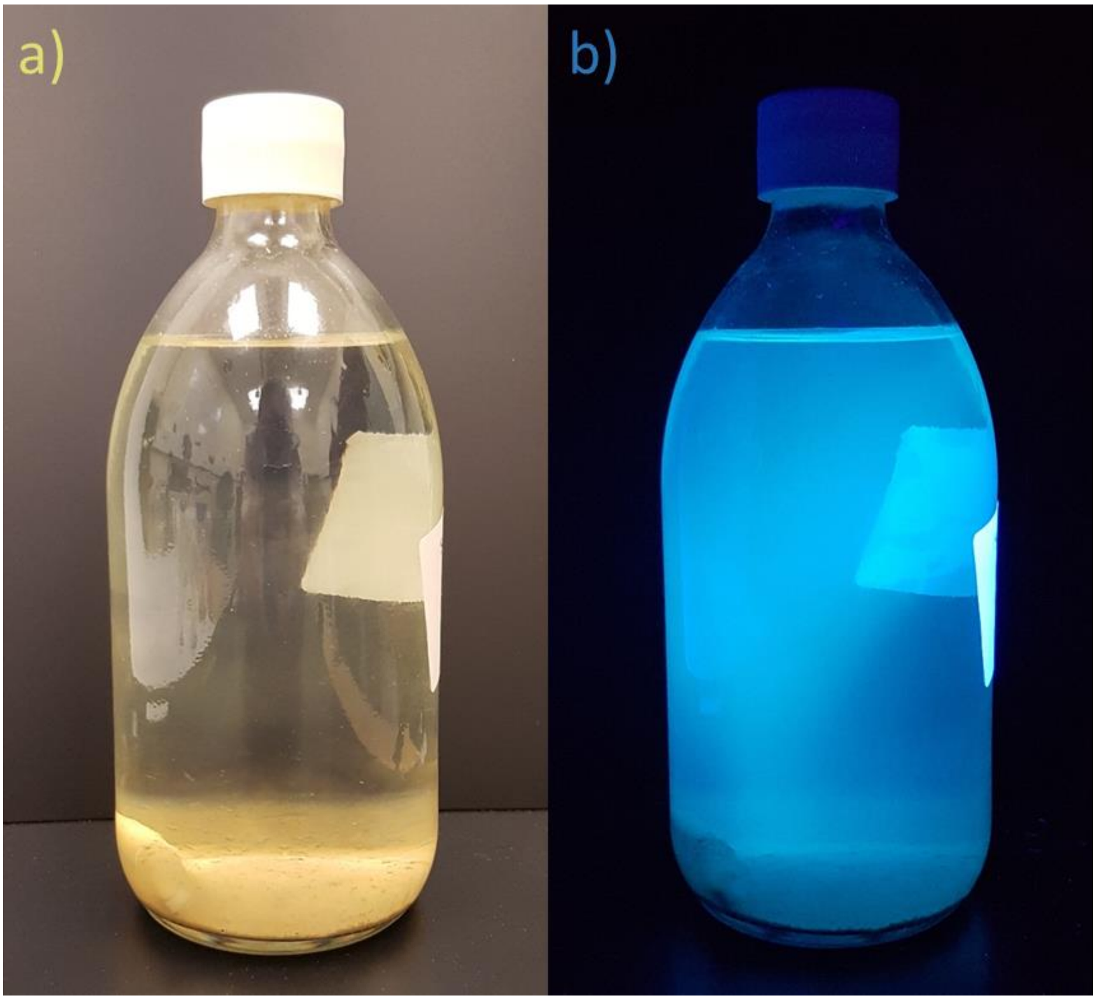

Figure 6.1. Visible and UV-vis images of PTI.LiBr/water solutions a) Image showing the slight yellow colour of the PTI.LiBr/water solution. b) Image of PTI.LiBr/water under UV illumination showing the strong fluorescence of PTI.LiBr dissolved in water.

6.2 TEM imaging and EDX mapping of the deposited nanosheets

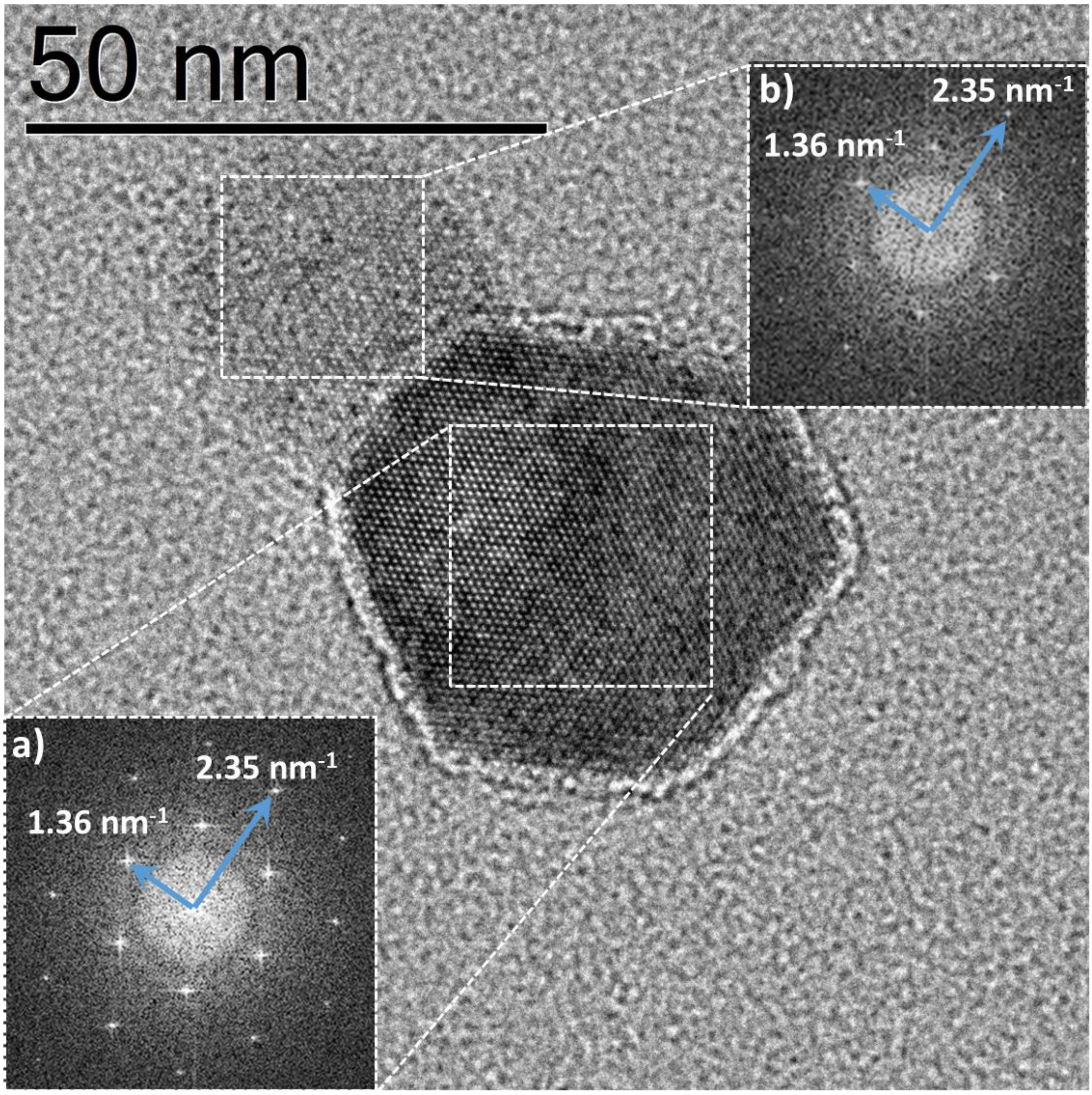

Figure 6.2. TEM images and Fourier transform of two different PTI.LiBr nanosheets with different thicknesses dried out of a pH 13 water solution. Inset a) Fourier transform image of the thicker PTI.LiBr flake. Inset b) Fourier transformed image of the thinner PTI.LiBr flake.

The solutions were gently removed with a pipette in order to separate the solution from the residual PTI powder without disturbing it. These solutions showed no sign of precipitate formation or colour change even after a year. In addition when centrifuged at 13000 rpm no precipitate was observed. An aliquot of the PTI.LiBr/pH 13 water solution was then dropped onto holey copper TEM grids which were placed on a hot plate that was heated to 60°C, then were dried at 100°C under a 10^{-6} mbar atmosphere. TEM images of the PTI.LiBr/pH 13 water solution (Figure 6.2a) clearly shows two overlapping crystalline flakes. The thicker crystal is ~40 nm across, while a smaller and much thinner crystal is partially overlapping the thicker crystal. The Fourier transforms of the TEM images for the thick and thin crystals are shown in the inset a and b respectively. The measured characteristic lengths of 1.36 nm^{-1} and 2.35 nm^{-1} (Figure 6.2a,b) correspond to the *100* and *110* reflections of the PTI.LiBr nanoflakes. These match exactly for those observed for bulk PTI.LiBr (Figure 3.3) and nanosheets of PTI.LiBr (Figure 5.8b) from the aprotic polar solvents. This shows that like the aprotic polar solvents the alkaline water solutions are capable of dissolving PTI.LiBr nanosheets into solutions. Again remarkably this dissolution process occurs without any observable change in the crystal structure of the PTI.LiBr flakes.

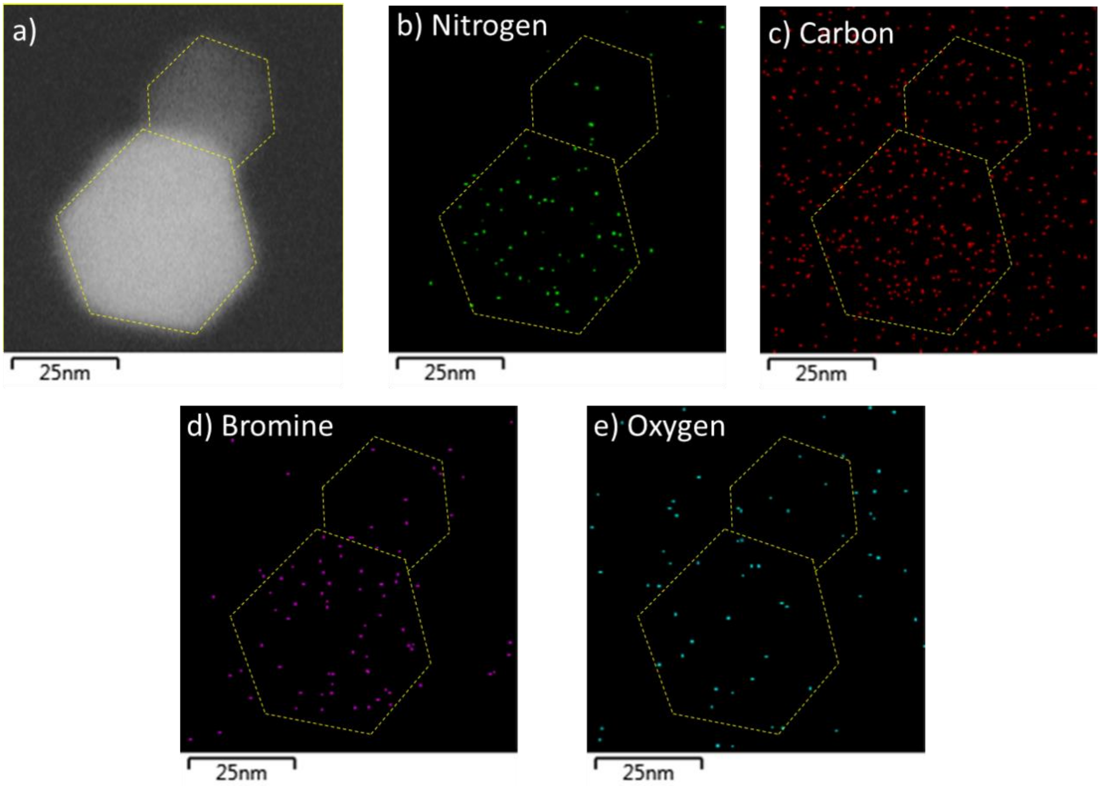

Figure 6.3. EDX image and elemental data of the PTI.LiBr flakes shown in figure 6.2. a) TEM image of the overlapping flakes. b) Nitrogen content with the flake outline marked c) Carbon content with the flake outline marked. d) Bromine content with the flake outline marked e) Oxygen content with the flake outline marked.

I used EDX spectroscopy to observe the elemental distribution of the nanosheets dried out from the PTI.LiBr/pH 13 water solution (Figure 6.3). These images were taken of the same flakes shown in figure 6.2. The carbon signal (Figure 6.3b) appears throughout the image, due to flakes being loaded onto a holey carbon TEM grid, although I note higher concentration within the deposited flakes region. The nitrogen (Figure 5. 6.3c) and bromine (Figure 6.3d) contents are located almost entirely within the flake. However the oxygen content (Figure 6.3e) appears to be evenly spread across the image. This agrees with the expected composition of the PTI.LiBr flakes consisting mainly of carbon, nitrogen and bromine, with lithium and hydrogen remaining undetected. The observation of the bromine is also significantly interesting as it shows that the LiBr intercalants are not significantly removed during the dissolution process, similar to that observed for the aprotic polar solvents.

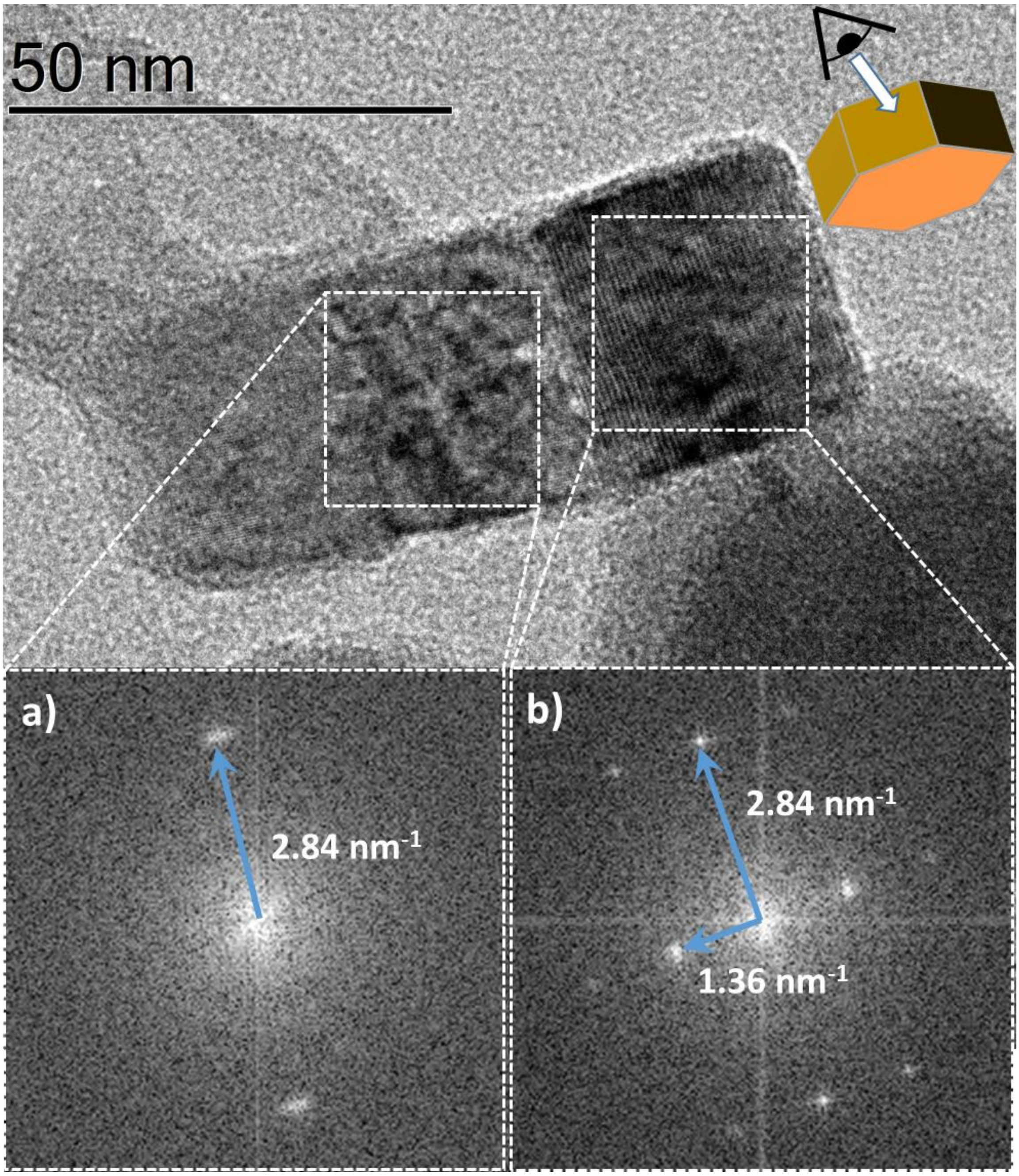

Figure 6.4. TEM image of a stack of PTI.LiBr flakes from the side showing several different faces of the crystal, Fourier transforms of this different faces are shown (Inset a, b).

Further TEM examination of the PTI.LiBr flakes deposited from the pH 13 water solution show a stack of PTI.LiBr flakes laying on its side. This allows us to directly measure the thickness of the stack to be ~30 nm across, corresponding to ~ 88 layers thick. While significantly thicker than observed for the aprotic polar solvents this still represents a degree of exfoliation just not down to few-layer stacks. However it is clear from figure 6.4/6.2 that there is a much wider range of thicknesses of the stacks of deposited PTI.LiBr crystallite compared to the aprotic polar solvents. Fourier transforms of the different edges of the hexagonal stack of PTI.LiBr (figure 6.4a,b) show the characteristic distances of 2.84 nm^{-1} and 1.36 nm^{-1} which correspond to the *100* and the *002* reflections of the PTI.LiBr phase. This shows the interlayer spacing of the PTI.LiBr has remained at 3.52 Å even after dissolution in the pH 13 water solution. Since any significant washing procedure would remove the intercalants and therefore significantly reduce the gallery height (Figure 4.7), it is clear that the halide intercalants has not been significantly affected by the dissolution process. So this dissolution is not being driven by the intercalated ions dissolving into solution.

6.3 The effect of pH on the dissolution of PTI.LiBr water solutions

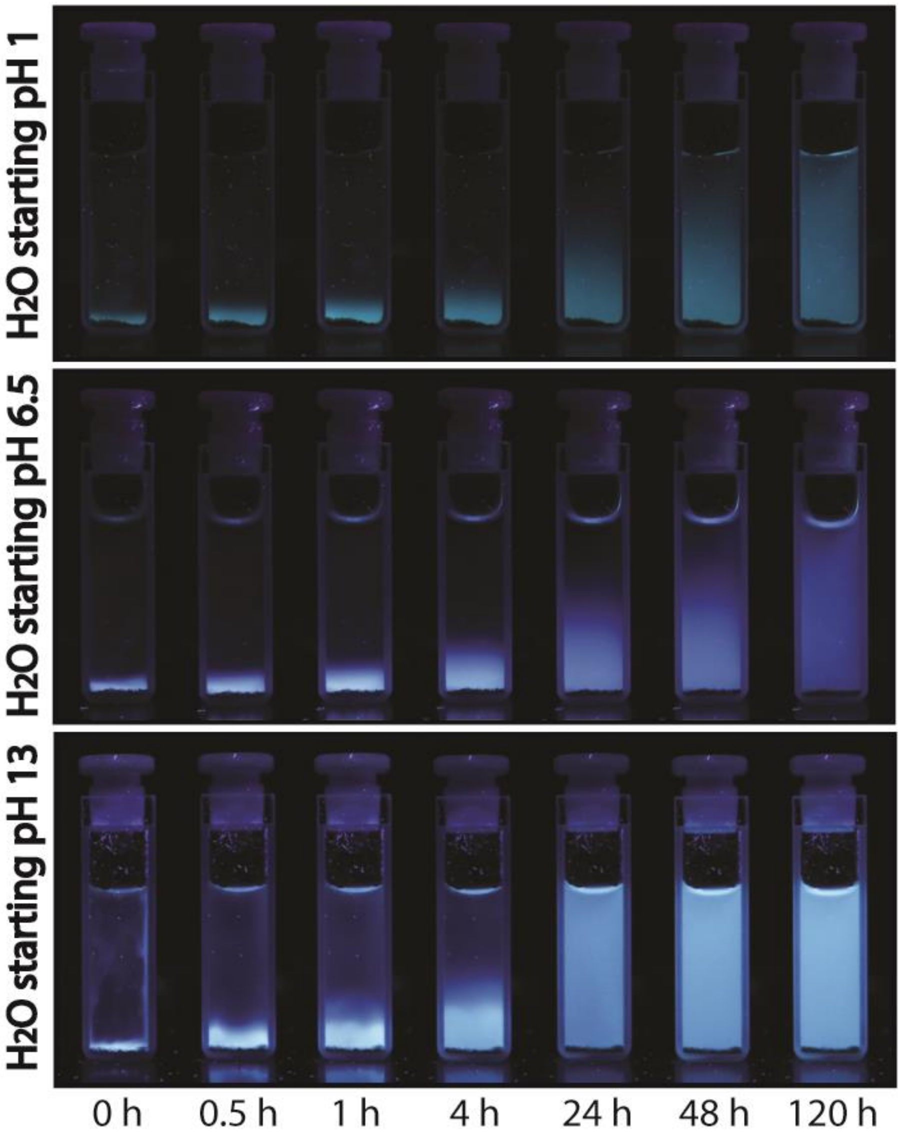

Figure 6.5. Images of PTI.LiBr/water solutions illumination by UV light. Several different water solutions are shown, the pH before the water was contacted with the PTI.LiBr was 1, 6.5 and 13.

As shown in figure 6.1 when the PTI.LiBr was contacted with pH 13 water solution the resulting solution fluorescence under UV illumination, figure 6.5 compares the fluorescence of PTI.LiBr contacted with different pH water solutions, the reported pH value as measured before the addition of the PTI. These images appear very similar to those observed for aprotic polar solvents, however there is a clear colour change of the solution dependent on pH. The pH 13 and pH 6.5 solutions have similar colour of fluorescence, however that for the pH 6.5 solution is significantly less intense suggesting it is at a lower concentration. In addition the pH 6.5 solution took longer to dissolve completely. The fluorescence of the pH 1 solution appears as a different colour. The concentration of the solution and speed to dissolution appears to be dependent on pH. Schwinghammer *et al.*[153] reported a dependence of the zeta potential to pH, with either low or high pH values (< 2, > 8) having a value high/low enough to be considered stable. This is likely due to the N-H bridging groups or in-ring nitrogens being protonated [129, 130] by the HCl in the pH 1 solution or the N-H bridging groups being deprotonated by the LiOH in the pH 13 solutions.[195] Though the deprotonation maybe occurring as H^+/Li^+ exchange. It is also possible that as with the PTI.HCl structure the nitrogen on the triazine ring could be protonated.[40, 129, 130] This would result in the formation of either an acidic or basic PTI.LiBr structure dependent on the pH of the solution, this could explain the relationship between final concentration of the solution and pH.

6.3.1 UV-visible spectra PTI.LiBr solutions with different starting pH

A series of solutions with pH values ranging from 1 – 13 were made using either HCl or NaOH, these solutions are named from the initial pH of each solution. 8 ml of these solutions were then contacted with 20 mg PTI.LiBr and left to spontaneously exfoliate for 2 weeks. An aliquot of each of these was taken and the UV-vis spectra of them taken (Figure 6.6).

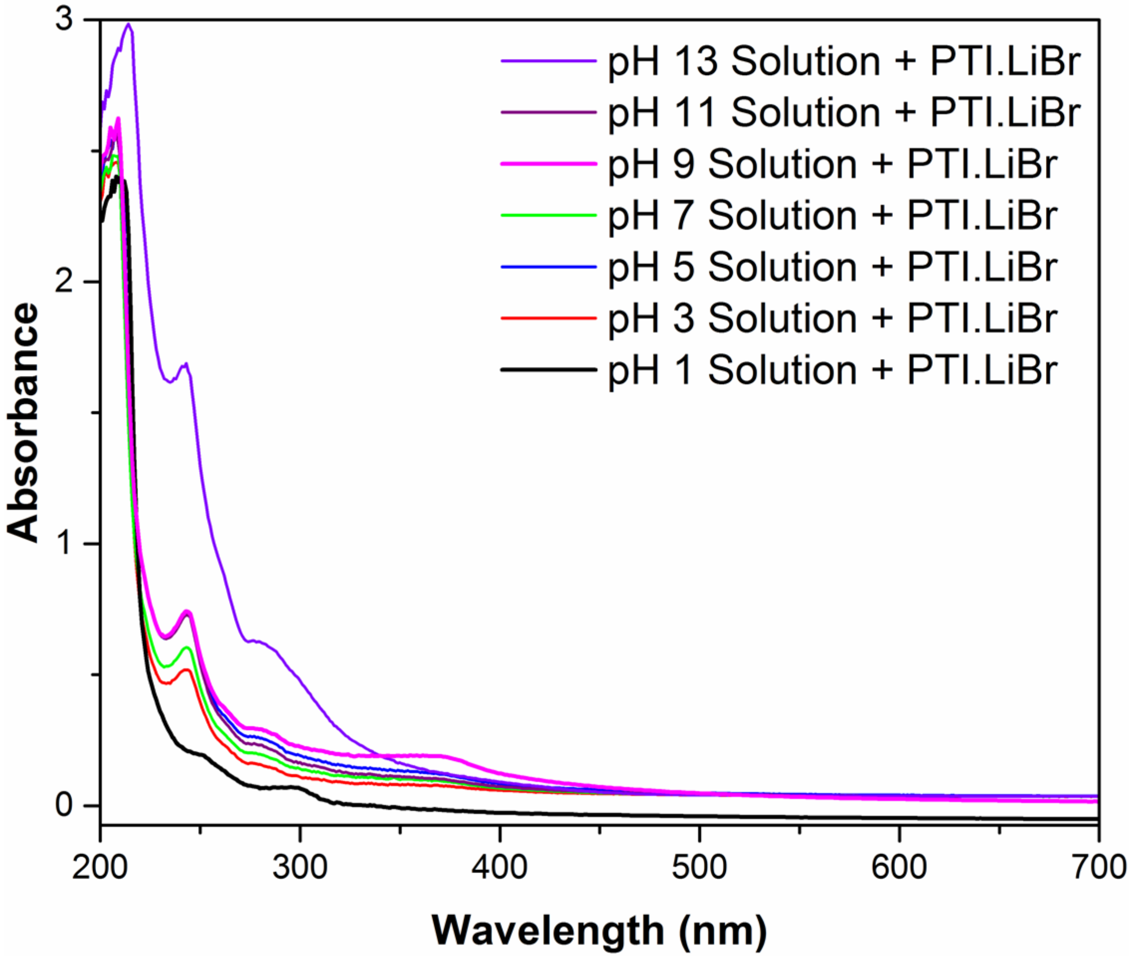

Figure 6.6. UV-vis absorbance spectra of PTI.LiBr/water solutions with different initial pH values of the water. pH was measured before it was contacted with PTI.LiBr.

In this series of solutions the only visible colour change was in the pH 13 solution, however all the solutions exhibited fluorescence under UV illumination. The pH 3 to 11 solutions all show maxima at the same wavelength, with the higher pH solutions having slightly higher absorbance. The shape of the UV-vis absorbance spectra of the pH 3-13 solutions have identical features and only differ in terms of absorbance. They all have a large peak ~210 nm, a smaller but sharp peak at ~245 nm, a less intense broad peak at ~280 nm and a broad shoulder at ~ 370 nm. The positions of these peaks is significantly different to those of the bulk material in which peaks are typically observed in 300 – 360 nm region. In the more concentrated aprotic polar solvents the UV-vis absorbance still showed some intensity between 400 – 500 nm, but the peaks between 300 – 400 nm were less intense than the bulk.

I also observe that the UV-vis absorbance spectrum of the pH 1 solution is distinctly different to that of the other solutions, with a broad peak at 260 nm and at 300 nm.

These do not appear in the same location or relative intensities as that of the other solutions. As mentioned above this may be an indication that at pH 1 the PTI.LiBr may be a protonated and hence the UV-vis absorbance spectrum has changed compared to the basic solutions.

6.3.2 pH of water before and after the addition of carbon nitrides

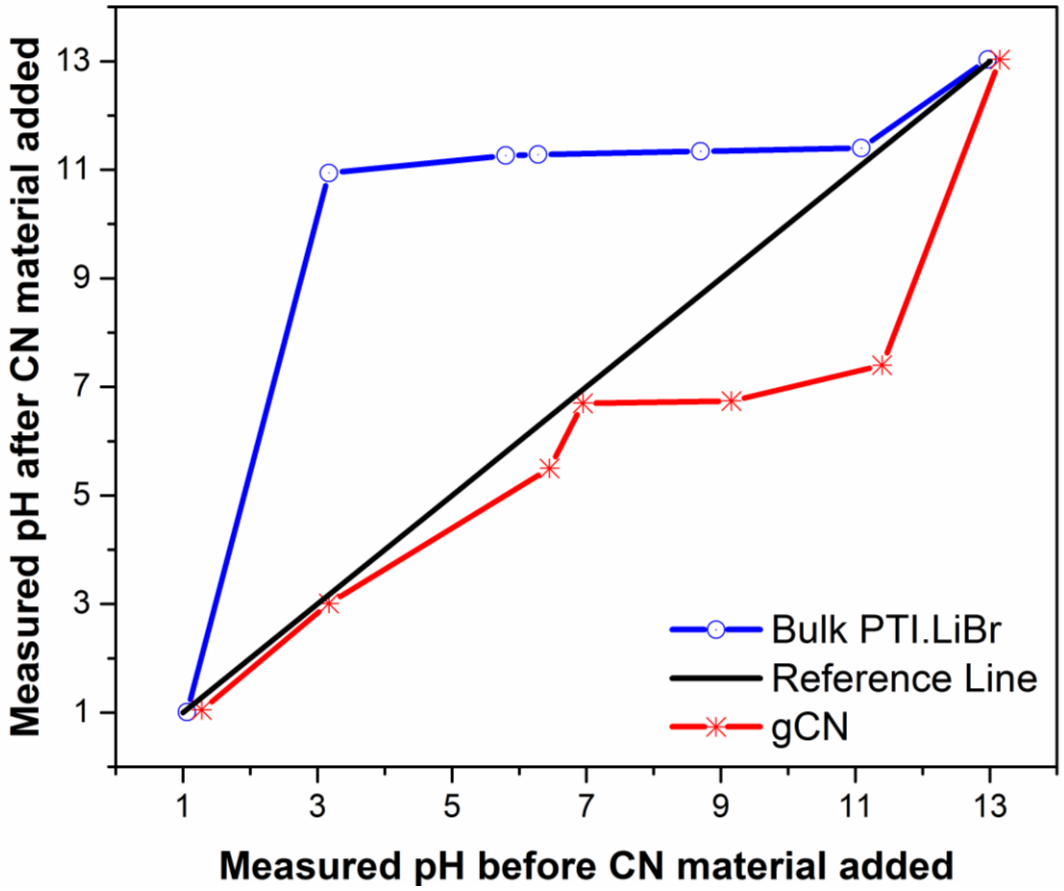

Figure 6.7. A chart showing the pH of water before and after addition of a carbon nitride material.

The UV-vis absorbance spectra of the pH 3 – 13 (Figure 6.6) appear to be very similar indicating they may all be the deprotonated PTI.LiBr. Given the observed change in pH when the bulk PTI.LiBr was washed (see Section 4.1) the pH of the solutions before and after the addition of the PTI.LiBr was investigated. A series of solutions with pH values ranging from 1 – 13 were made using either HCl or NaOH. 8 ml of these solutions were then contacted with 20 mg PTI.LiBr and left to spontaneously exfoliate for 2 weeks. An aliquot of these were taken and the pH measured after the dissolution process (Figure 6.7). These clearly show that the addition of PTI.LiBr results in the solution becoming highly basic (pH 11), unless it is initially at pH 1 or pH 13. The same procedure was repeated for gCN as it shares a similar carbon nitride structure but does not possess intercalated lithium. This shows that the gCN appears to have the opposite effect and results in neutral solutions when the basic water solutions are added, this suggests that the carbon nitride structure appears to independently be acting as a pH buffer. The N-H bridging environments are able to act as a Lewis base, Brønsted acid and base, while the in-ring nitrogen can act as a Lewis base and Brønsted base.

It has been previously noted by Schwinghammer *et al.*[153] and seen in our experiments that the addition of PTI.LiBr to water forms a basic solution. This likely due to the formation of lithium hydroxide as water exchanges a proton with the bridging N-Li bonds to form LiOH. Previous reports of the lithium content of PTI suggest between 1 and 3 lithium per unit cell, which is roughly 0.07 mmols of potentially exchangeable lithium for 20 mg of PTI.LiBr. This calculates to be ~ 8 mM of lithium cations within the 8 ml water solution, which equates to ~ 11.9 pH. Due to the relatively large amounts of N-Li environments within the PTI even fairly acidic pH 3 solutions become basic after the addition of PTI.LiBr.

6.3.3 The effect of different starting mass on the concentration of PTI.LiBr solutions

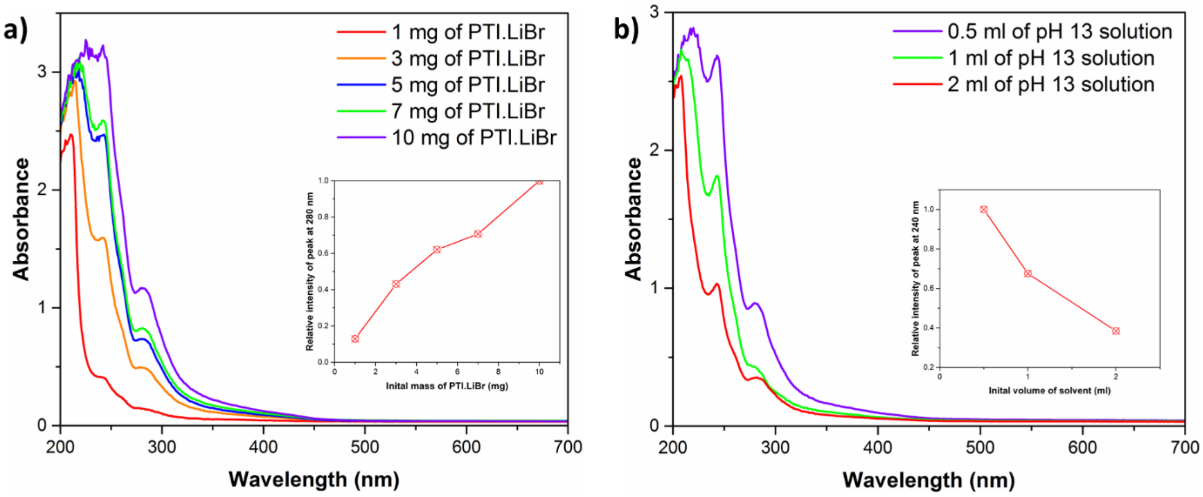

Figure 6.8. UV-vis absorbance spectra of PTI.LiBr/pH 13 water solutions formed using different quantities of either the solvent or the bulk PTI.LiBr. a) Absorbance spectra of PTI.LiBr /pH 13 water solution formed by different initial mass of PTI.LiBr, with inset showing the change of the relative intensity of the peak at 280 nm with initial mass. b) Absorbance spectra of PTI.LiBr /pH 13 water solution formed by different initial volume of pH 13 water, with inset showing the change of the relative intensity of the peak at 240 nm with initial volume.

As mentioned before the concentration of the solution is dependent on the initial mass of PTI.LiBr, to further examine this further I made a series of solutions formed using a different amount of pH 13 water solutions and PTI.LiBr, the UV-vis absorbance spectra of them was then recorded (Figure 6.8). 8ml of a pH 13 solutions was contacted with a given amount of PTI.LiBr and left to spontaneously exfoliate for 2 weeks. The UV-vis spectra of these samples (Figure 6.8a) clearly show a strong relationship between the initial mass PTI.LiBr and the absorbance of the peaks, the relative intensity of the peaks clearly shows a strong dependence on the initial mass (Figure 6.8a inset).

A given amount of pH 13 solutions was contacted with 10 mg of PTI.LiBr and left to spontaneously exfoliate for 2 weeks. An aliquot of these was removed and the UV-vis spectra of them taken (Figure 6.8 b), clearly showing that the lower PTI.LiBr mass to water ratio reduces the concentration (Figure 6.8b inset). In addition when all of the solution is removed from contact with the PTI and replaced with more pH 13 water a colour change is observed in this new solution. This shows there is not just a soluble fraction of PTI.LiBr that can dissolve but rather the amount of material dissolving into solution is proportional to the initial mass of PTI.LiBr. This is the same effect I observe in the polar aprotic solvents (Chapter 5.4.2), where the activity of the solid must not be equal to zero to balance the equilibrium equation or a reaction is occurring simultaneously. In the water based systems it can be easily understood that the Li^+/H^+ exchange that causes the change in pH of the water is proportional to the amount of solid. Since I have shown the final concentration of solution to be dependent on pH (See Section 6.3.2), the amount of solid PTI will indirectly effect the final concentration via the Li^+/H^+ exchange between the water and the PTI solid. However I have not yet identified the cause of this atypical behaviour of the solid in the polar aprotic solvents (Chapter 5.4.2), so whatever is causing this effect in in the organic solvents may also be occurring in the water based solutions in conjunction with the pH effects mentioned above. Without further investigation of the dissolution mechanics of both the water and organic solvent dissolutions we cannot be if the solid’s activity is not 1 or if there are additional reactions occurring.

6.4 Conclusion

I have shown that PTI.LiBr spontaneously exfoliates in water solutions in addition to the aprotic polar solvents. The dissolved nanosheets were observed under TEM, this showed crystalline undamaged PTI.LiBr nanosheets deposited on the surface. The thicknesses of these stacks of nanosheets were significantly more varied, with some flakes being much thicker than those observed for the aprotic polar solvents. The UV-vis spectra of the PTI.LiBr shows a different series of peaks compared to the bulk PTI.LiBr, this is most likely due to the significantly lower concentration of the water solutions, allowing us to observe peaks that were previously hidden. I observed that the concentration of the solutions is dependent on the pH of the water and unusually the related initial mass of PTI.LiBr and initial volume of water. A change in UV-vis spectra of the PTI solutions is seen for different initial pH water, most likely due to protonated or deprotonated of the PTI framework.

Chapter 7 – Triazine based graphitic carbon nitride (TGCN)

Forming a layered C_3N_4 material has become of significant interest due to potential applications in photocatalysis and optoelectronics.[45, 166, 196-198] As discussed in Section 1.2 many papers use the phrase g-C_3N_4 or just C_3N_4 in their title, however only three reports have experimentally shown the formation of a C_3N_4 material.[41, 51, 52] Kouvetakis *et al.*[51, 52] reported the CVD synthesis of a layered carbon nitride from precursors based on C_3N_3 rings. They reported the formation of a polycrystalline material contain sp^2 carbon and nitrogen, with no N-H/O-H observed from IR. From this it was suggested to be triazine based C_3N_4 material. Algara-Siller *et al.*[41] recently reported an ionothermal eutectic salt synthesis based on that used for PTI.LiBr, they reported the method to yield a layered triazine based C_3N_4 material. HR-TEM images were used to observe a highly crystalline region with spacing that matched the reported structure. In addition a very recent report by Ladva *et al*.[199] detailed a synthesis of a carbon nitride containing material. This method used a similar eutectic salt synthesis to Algar-Siller *et al*. but instead of heating in a sealed ampoule the gaseous products were collected and the resultant film was investigated. Interestingly even though this report details a material with similar flake-like morphology, XRD pattern, X-ray photoelectron spectra and synthesis method it was reported to be a layered HCN based polymer.

This chapter will focus on our attempts to reproduce the synthesis of one of these C_3N_4 materials reported by Algara-Siller *et al.* for triazine based graphitic carbon nitride (TGCN).

7.1 Synthesis of 'TGCN'

The synthetic procedure reported by Algara-Siller *et al.*[41] was followed. Due to a slight difference in the length of our ampoules the mass of the regents used were adjusted proportionally to the volume of the ampoule reported by Algara-Siller *et al.*[41] Dicyandiamide (0.83g, Sigma Aldrich) was ground together with a pre-dried eutectic mixture of KBr (5.99g, Alfa Aesar) and LiBr (6.48g, Aldrich) under an N_2 atmosphere. The mixture was transferred to a quartz ampoule (OD 25 mm, ID 22 mm, 15 cm long, Robson Scientific) and evacuated to 10^{-5} mbar (Leybold vacuum systems, PT70G compact). The ampoule was sealed under vacuum using a ethylene/O_2 flame by the in-house glass blowing service at UCL. The ampoule was placed in an aluminium sleeve which was then heated to 400˚C at 40 ˚C/min, maintained for 4h at this temperature, then raised to 600˚C at 40 ˚C/min for 60h, in a horizontal tube furnace (Carbolite MTF 12/38/400). The block containing reaction products and salt was broken up and placed in distilled water. Insoluble flakes up to 1-5 mm in dimension were identified by their distinctive colour and shiny appearance and separated individually with tweezers and washed in water. Recovered flakes (~70 mg) were placed in a drying oven (Figure 7.1b). However due to variation in flake size and thin nature of the flake recovering all of the synthesised sample is difficult. The remaining bulk powder was a mix of dark brown powder and shiny flakes that are too small to manually separate this out. This mixture was filtered and washed to remove any residual salt content (Figure 7.1a).

During the synthesis ammonia pressure is generated in the ampoule, this results in potentially rupturing of the ampoule during synthesis if the glass cap has not formed a good seal, or if the salts used in the synthesis are wet. Ampoule rupturing results in loss of the material and damage to the oven, significant care should be taken when following this synthetic method. From our experience small variations in reaction condition can result in loss of ampoule or no formation of the desired product. In addition the DCDA to volume ratio inside the ampoule must be kept the same if a larger ampoule is used and if the DCDA is not increased to match then little to no flakes forms, if too much DCDA is used then the pressure is too great for the ampoule which results in its loss.

In a typical synthesis the flakes form within the salt block, concentrated around the part of the ampoule that is nearest to end of the aluminium sleeve, and are deposited on the surface of the ampoule. In addition if the ampoule is placed in the furnace vertically the yield of flakes is significantly reduced, with those synthesised being located near the top of the ampoule in a ring rather than in the salt block. The flakes form when using both Br and Cl salts, the yield when using bromine salts appears to be slightly higher, though this has not been thoroughly explored.

7.2 Characterisation of resultant material

7.2.1 Visual images of the recovered materials

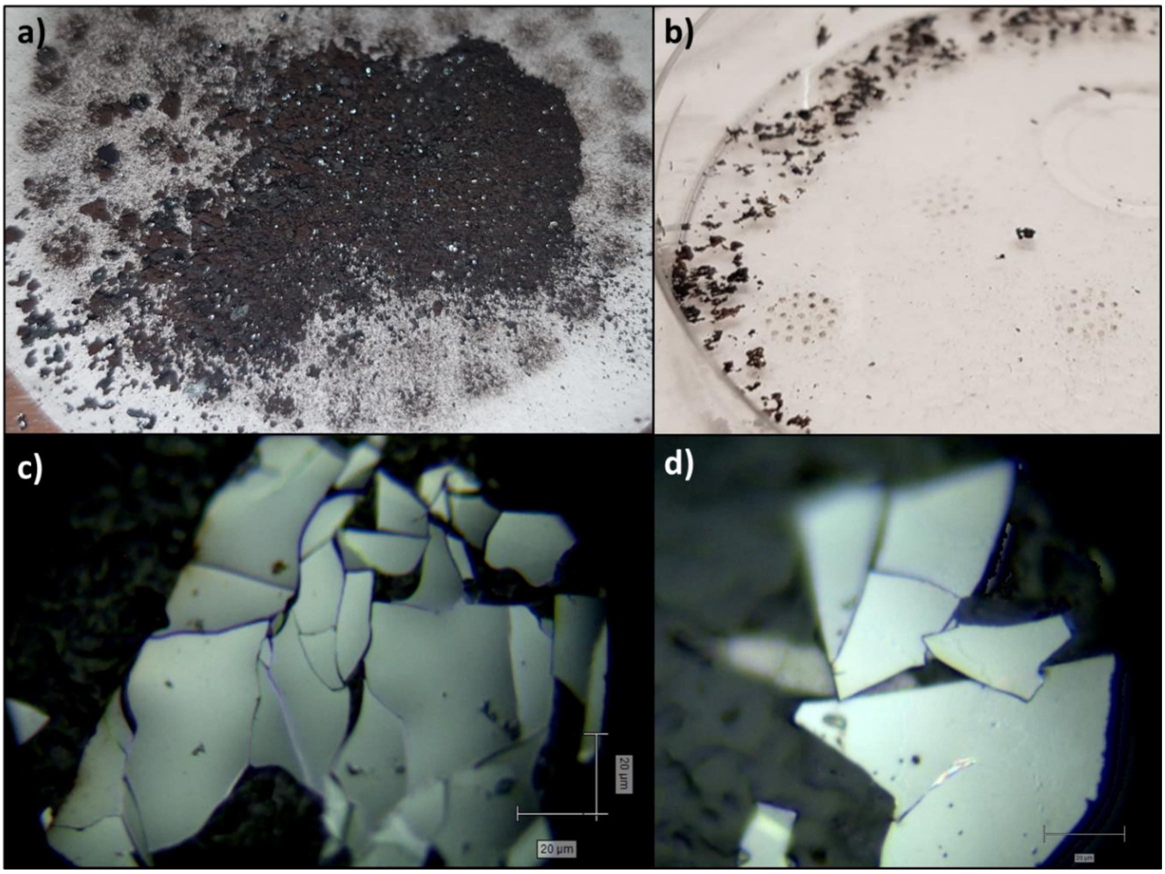

Figure 7.1. Pictures of the recovered materials. a) Picture of recovered bulk material showing the dark brown powder mixed with black reflective flakes. b) Black reflective flakes separated from the brown powder. c,d) Front lit images, showing the highly reflective surface of the cleaved flakes.

Optical images of the recovered material shows two distinct phases, the millimetre sized dark reflective flakes (Figure 7.1b,c,d) and a dark brown powder (Figure 7.1a). The dark brown powder is intermixed with the flakes that are too small to remove. When the larger flakes are cleaved using Scotch tape the surfaces of the flakes flat, uniform and highly reflective (Figure 7.1c,d). This suggests a continuity of the flakes over microns without significant imperfections post-cleaving. Carbon nitride materials do not typically form into millimetre sized flakes, a clear indication that this synthesis has yielded a distinct layered material. I followed the lead of Algara-Siller *et al.* and focussed on the characterisation of the flakes rather than the dark powder.

7.2.2 TEM and SEM of the flakes

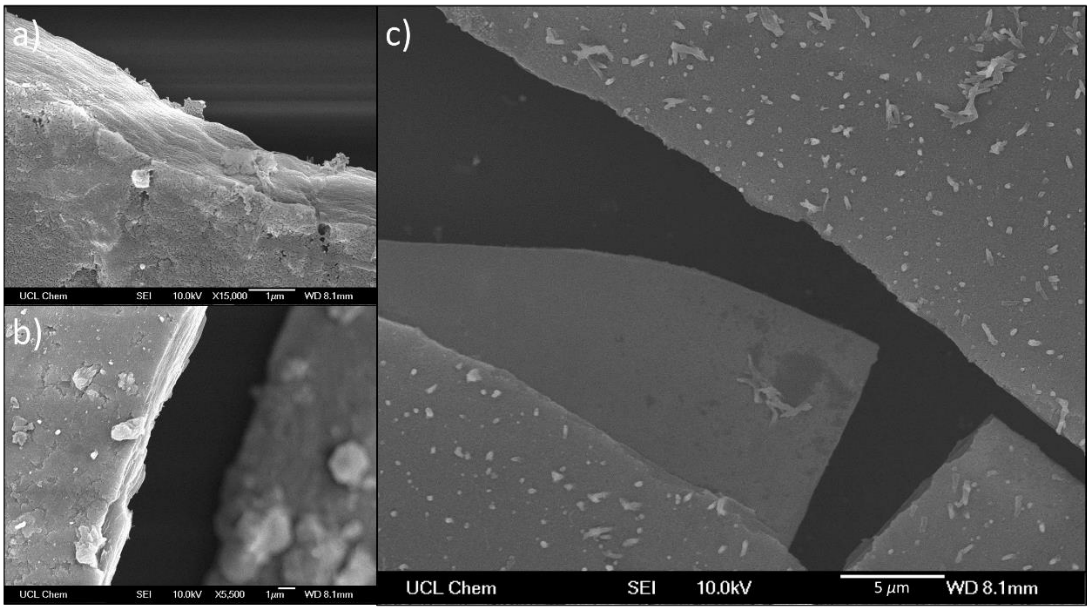
a)
UCL Chem SEI 10.0kV X15,000 1μm WD 8.1mm
b)
UCL Chem SEI 10.0kV X5,500 1μm WD 8.1mm
c)
UCL Chem SEI 10.0kV 5 μm WD 8.1mm

Figure 7.2. SEM images of uncleaved flakes. a) SEM image clearly showing layer stacking and some damage to the top sheet b) SEM image of inhomogeneity on the surface of the flakes as well as showing the layered stacking c) Zoomed out image showing a large crack between the millimetre sized flakes.

SEM images of the recovered material (Figure 7.2) show large flakes that can extend up to several millimeters and are several microns thick. Clear layering of the flakes is observed. Damage to the surface of the flakes is evident from the ‘cracks’ across the surface of the layers as well as numerous imperfections on the surface. This is in clear contrast to the uniform and reflective images seen for the cleaved samples in Figure 7.1, indicating that the top surface of flakes is decorated with other carbon nitride materials and salt residue from the synthesis. The thickness and extent of the sheets match the morphology reported by Algara-Siller *et al.*[41] for TGCN and the layered CNH polymer reported by Ladva *et al*.[199] Other crystalline carbon nitrides have only shown nanoflakes that are up to several hundred nanometer across (Figure 3.10, 3.11). No millimeter/micron sized structures with clear layer stacking have been reported prior to Algara-Siller *et al.* first showing the macroscopic structure of TGCN, making it unique amongst carbon nitrides.[56, 131]

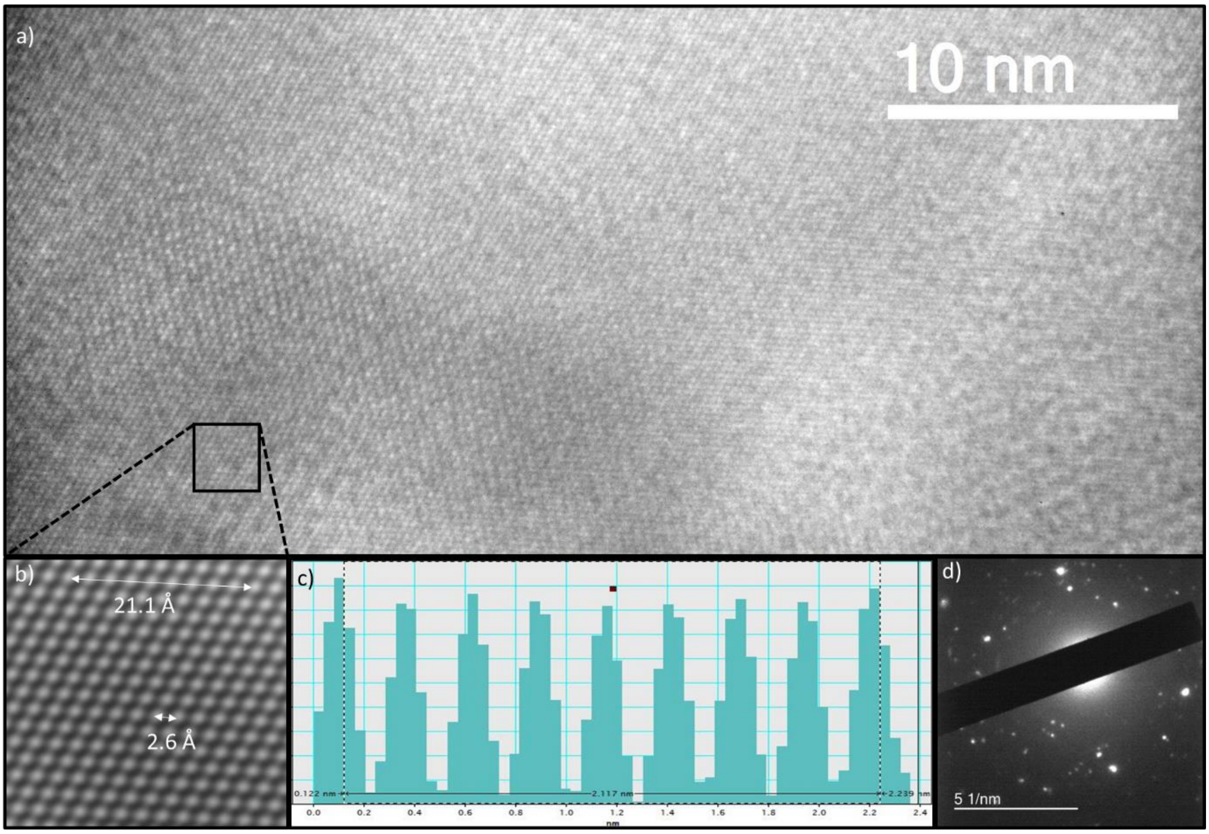

Figure 7.3. TEM images for an uncleaved thin flake of our sample focussed on a region showing lattice fringes. a) TEM image showing the presence of crystalline domains within a small region of the sample. b) Expanded filtered TEM image of one nanocrystalline region demonstrating the hexagonal layer symmetry with a characteristic 2.6Å separation between bright spots. c) Line scan across the image intensity variations used for the FT determination of the intralayer lattice spacing. d) SAED pattern indicating different crystalline layer orientations sampled by the electron beam passing through the flake.

TEM images (Figure 7.3) for the recovered flakes were taken by sonicating the samples in methanol for several minutes, this suspension was then dropped onto a TEM grid and dried. One of the resultant TEM images (Figure 7.3a) shows an area with multiple lattice fringes, indicating several crystalline structures. However the appearance of the lattice fringes changes over the length of the image. Given that there appears to be continuity of the flake across this image this is an indication of several different stacking regimes in the same area. There is also a significant variation of thickness across the image indicated by the varied contrast. One of these crystalline domain (Figure 7.3a,b,c) has with an in-plane hexagonal lattice spacing of 2.6 Å as determined by Fourier transformation of the image intensity data, showing the identical spacing and images as to those recorded by Algara-Siller *et al.*[41] Selected area electron diffraction (SAED) data (Figure 7.3d) for this region of our samples exhibited irregularly spaced series of bright spots around the main diffraction rings. This indicates the presence of several different crystalline structures, potentially overlapping crystalline domains with different orientations. Moiré patterns also appeared in some parts of the TEM images, indicating that slightly misaligned layers are present throughout the thickness. These observations from the TEM strongly suggest the presence of several different crystalline structure, possibly due to different stacking regimes of the material over even a small area of the flake. The energy difference between the different stacking regimes were reported to be low,[41] making the possibly of multiple stacking regimes across the same flake surface likely.

However in addition to images showing large areas of lattice fringes I also observe large regions where no indications of crystalline structure could be observed, or areas where different lattice fringes are only observed on the edges of the flakes. A catalogue of these images can be found in the appendix (Section 9). It is clear then from the TEM images that the material is not formed from one continuous crystalline material with a single structure. It has some crystalline regions with different crystal structures, however I was unable to identify the exact crystal structures that were observed by SAED. From this I suggest that the recovered material is not different stacking regimes of the TGCN reported by Algara-Siller *et al*. but a continuous flake with a series of different unidentified crystal structures throughout.

Algara-Siller *et al.* presented high resolution TEM images from thin regions of mechanically cleaved flakes of TGCN.[41] These images showed a crystalline region with a characteristic distance between bright posts of 2.6 Å. This was used to confirm the presence of triazine-based C_3N_4 layers that were best modelled with an ABC stacking pattern, however this characteristic distance is also seen for graphite. The same 2.6 Å characteristic distances were observed in Figure 7.3b.

7.2.3 Powder and reflection geometry XRD

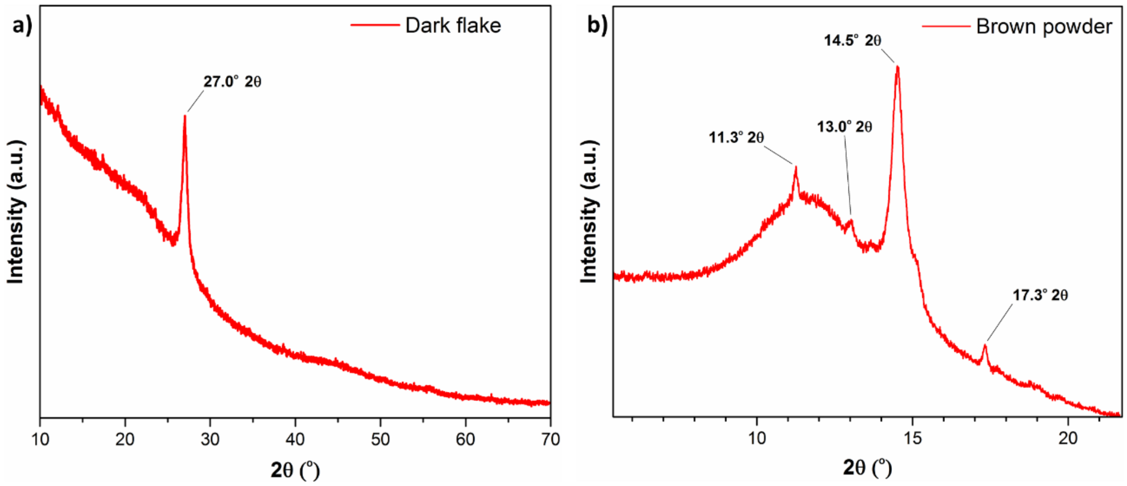

Figure 7.4. XRD patterns of different parts of the recovered materials a) Rocking geometry of the dark flakes b) PXRD of the dark brown powder. Note the scale of a is given where (λ = 1.54056 Å) and the scale of b is given where (λ = 0.827127 Å). This is for easier comparison to literature data.

XRD data (Figure 7.4a) were obtained for a single flake by mounting it perpendicular to the beam, this was combined with rocking the sample by +/- 5˚ about the incident beam axis. The pattern collected via this setup (Figure 7.4a) showed only a single strong peak at 27˚ with weak broad features at 22˚ 2θ, 45˚ 2θ and 56˚ 2θ. The XRD patterns of gCN also typically show a strong peak at ~27˚ 2θ, this is usually assigned to the interlayer spacing reflections between two graphitic sheets.[47] Given our observations of the layered structure via SEM (Figure 7.2), I suggest that this peak is due to the out of plane reflections in a layered system. However no other strong peaks that would indicate a crystalline material are observed.

The PXRD of the dark brown powder (interdispersed with small flakes) (Figure 7.4b) shows that no indication of any PTI materials. A large peak is observed at 14.5˚ 2θ (where λ = 0.827127 Å), the same peak would occur at 26.9˚ 2θ (where λ = 1.54056 Å). This peak can again be assigned to graphitic interlayer reflections. However unlike the XRD patterns of the flakes the powder shows several sharp peaks at 11.3˚ 2θ, 13.0 ˚ 2θ and 17.3 ˚ 2θ, these peaks are due to a small quantity of an unidentified crystalline material. However it is not clear if the main peak at 14.5˚ 2θ is from the mixed in flakes or due to the same crystalline material that is causing the appearance of the sharp peaks. Given this there is little structural information on the crystalline material, and therefore cannot determine what exactly it is. It is clear though that the powder and flakes have different components and that the only observed crystalline material is in the powder.

Algara-Siller *et al.*[41] reported two different XRD patterns obtained using laboratory and synchrotron facilities for their TGCN samples. The first pattern was collected in a reflection geometry. This pattern contained a main broad peak at 27˚ 2θ (where λ = 1.54056 Å), assigned to the (*002*) interlayer reflection and a second smaller broad peak at 24˚ 2θ, some small higher order features are also observed. An AB stacked TGCN structure was fitted to these two peaks. Apart from the peak at 24˚ 2θ this pattern is similar to what is observe for the flakes synthesised in this thesis, however the lack of this peak suggests different crystal structure between our material and that reported by Algara-Siller *et al.*

The second pattern was a powder XRD pattern measured on a synchrotron beamline (where λ = 0.827127 Å). This showed a main feature at ~14.5˚ 2θ along with small sharp peaks at ~11˚ 2θ, ~13˚ 2θ and 17˚ 2θ. The same AB stacked TGCN structure developed from the reflection geometry XRD pattern was also fitted to this data. However the overlap between the proposed and experimental data was not convincing, as the experimental data of the two different XRD patterns reported by Algara-Siller *et al.* do not match well. In particular there is no peak at 17˚ 2θ when this peak is clear in the experimental data. This second pattern matches exactly with the PXRD of our synthesised powder sample (Figure 7.4b). Given these similarities between the second XRD pattern reported by Algara-Siller *et al.* and the PXRD of the dark powder in this thesis it is unclear what material measured was.

I suggest that the carbon nitride millimeter sized flakes, both synthesized here and reported by Algara-Siller *et al.* should not be considered crystalline given their XRD patterns, even though some evidence for nanocrystalline regions are observed under TEM.

7.2.4 CNH analysis

To yield more information on the structure of the synthesised material and to investigate possible structural differences between the flakes and the powder, CNH analysis was performed. Samples were sent to the University of Sheffield for CNH elemental analysis. Elemental analysis was carried out at the using a Vario MICRO cube elemental analyzer (Elementar).

	PTI.LiBr	Dark flakes	Dark brown powder
Found Stoichiometry	$C_{12}H_{10.2}N_{16.6}$	$C_{12}H_{8.1}N_{9.6}$	$C_{12}H_{8.9}N_{9.8}$

Table 7.1. Stoichiometry of several carbon nitrides found by CNH analysis.

The stoichiometries of the synthesised flakes and the dark brown powder are shown in Table 7.1, CNH analysis of PTI.LiBr was also performed for comparison. The stoichiometry found for PTI.LiBr is very close to that previously reported, though the hydrogen content is slightly higher than would be expected.[54, 56, 131] The family of carbon nitrides that PTI is a part of is partly defined but its high nitrogen to carbon ratio, C<N.[37, 46, 53, 54, 56, 131] The reported C:N ratio for flakes was found to be 4:3 rather than the expected 3:4, an inversion of the carbon/nitrogen ratio compared to PTI. This suggests a significantly different structure, either closer to nitrogen doped graphite materials or a composite formed of graphitic carbon and carbon nitride. The same ratio is observed for the dark brown powder. These similarities in the composition are surprising given their structural differences and that they both show similar deviation from typical carbon nitrides stoichiometries. This may suggest they are structurally similar with the powder being the pulverised formed of the flakes.

Surprisingly given the similarities between the flakes synthesised in this thesis and those reported by Algara-Siller *et al.* reported a composition of $C_{12}H_{1.9}N_{16.0}$ for the combustion and ICP analysis for TGCN.[41] The discrepancy between this result and those shown in Table 7.1 suggests a significantly different material in each case, this is in contrast to the similarities of the visual appearance, SEM images, TEM images and X-ray photoelectron spectra. (Figure 7.1, 7.2, 7.3, 7.6)

Ladva *et al*.[199] found the C:N ratio to be 1.2:1, very close to those found for the flakes synthesised in this thesis. The similarities of this unique C:N ratio, SEM images, TEM images and X-ray photoelectron spectra (Figure 7.2, 7.3, 7.6) strongly suggest that the flake synthesised in this report and that by Ladva *et al*.[199] are structurally related.

7.2.5 XPS of the recovered flakes

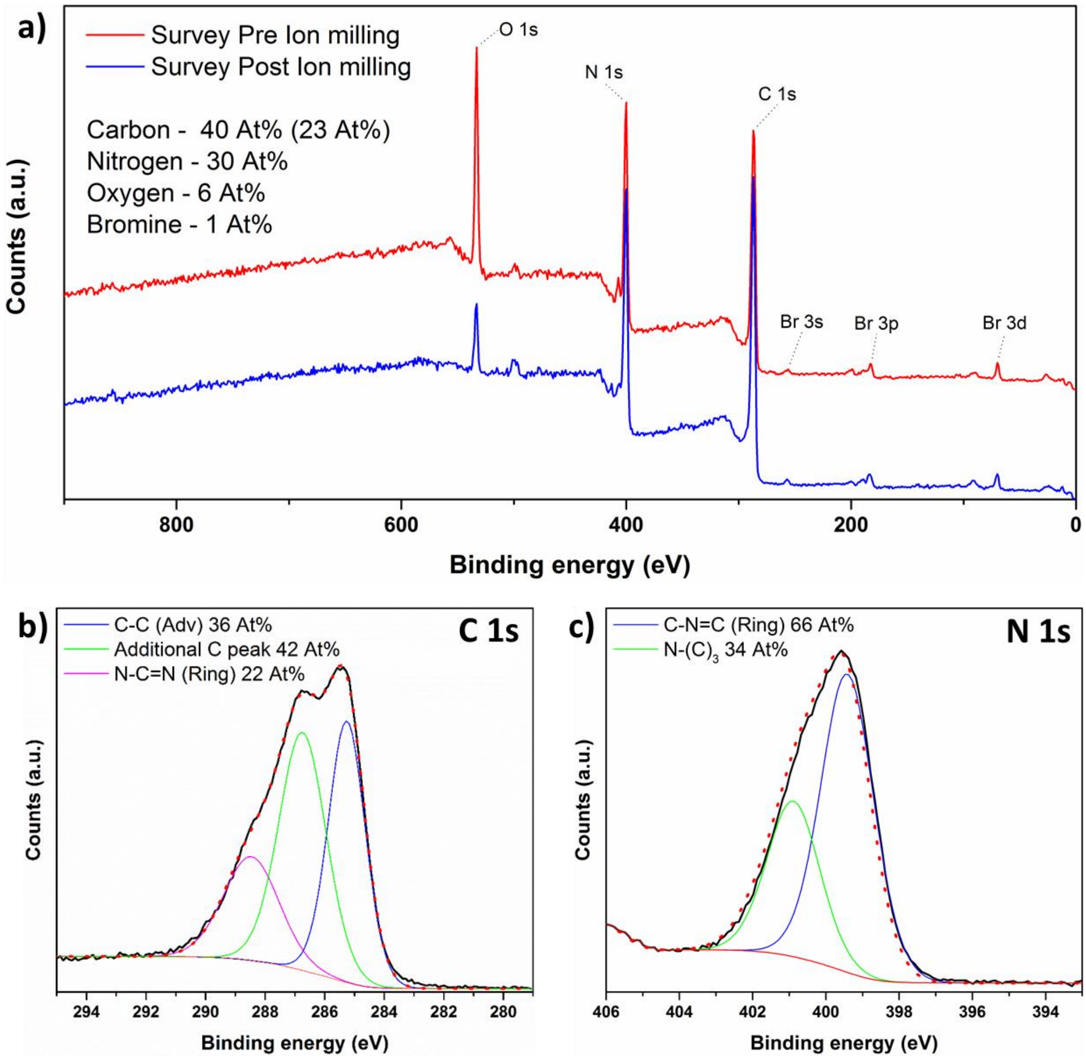

Figure 7.5. XPS and analysis of the recovered flakes a) Survey spectrum, showing pre and post ion milling. b) C1s spectrum. c) N1s spectrum. The elemental composition of the material is given in atomic percent post ion milling.

The XPS survey spectrum of recovered flakes (Figure 7.5a) shows a significant carbon, nitrogen and oxygen content, with the presence of a small amount of bromine. The O 1s peak decreased in intensity upon ion-milling. Atomic percentages of different elements post ion milling are shown, the carbon from non-adventitious content is listed first while that just from the adventitious component is shown in the brackets.

The C 1s peak can be fit with three Gaussian-Lorentzian peaks (Figure 7.5b) indicating three distinct carbon environments. The peak at 285.3 eV can be attributed adventitious carbon, a thin layer of non-graphitic carbonaceous material as a result of the samples air exposure,[200] typically XPS of carbon nitrides show a strong adventitious peak. However a peak in this position can also be attributed to C-C bonding in graphitic systems. The peak at 288.5 eV is at a similar position as found for the carbon in the triazine ring of the molecular compound melamine,[138] and seen for PTI materials (Figure 3.6 and 3.7). This peak can be assigned to in-ring C-N-C, typically seen in a carbon nitride material.[41]

The third environment, at 286.7 eV, is also observed in the PTI materials (Figure 3.6 and 3.7) though with a significantly smaller relative intensity. Peaks in this position for carbon nitride has previously assigned to nitrile bonding.[41] However I suggest that the peak 286.7 eV cannot be assigned to nitrile peaks as no vibrations related to this group are observed in the IR spectrum (Figure 7.7). Peaks in this region can also be associated with C-O,[201] as seen in the spectrum of carbon tape (Figure 3.5). Given that this peak does not significantly change intensity after ion milling it is unlikely to be fully explained by C-O bonding. Nitrogen doped graphene materials also exhibit a peak in this area,[202] this is typically assigned to sp^2 carbon environment where the carbon is bonded both to other carbon and to nitrogen atoms. The difference in binding energy is caused by the carbon bonding with fewer electron withdrawing nitrogen atoms as shown in Figure 7.6. The peak at 286.7 eV therefore could be assigned to carbons bonded to a mix of carbon and nitrogen atoms, these environments are typical in nitrogen doped graphenes and not observed in traditional carbon nitride structures where all bonding is only $C\text{-}(N)_3$.

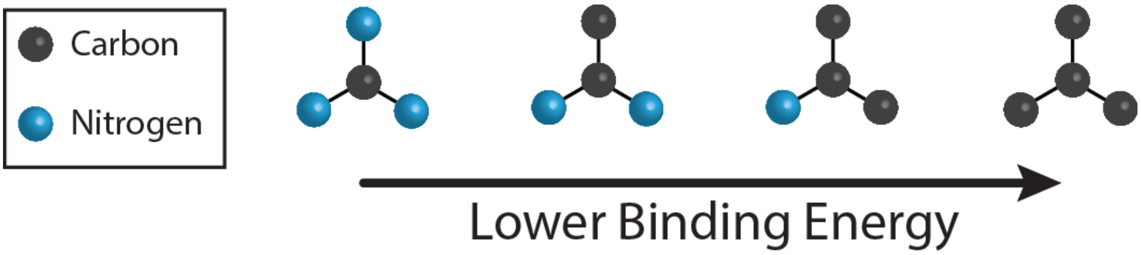

Figure 7.6. Schematic showing different types of sp^2 carbon nitride bonding.

The N1s region shows two distinct environments when fit with Gaussian-Lorentzian peaks (Figure 7.5b). The first, at 399.4 eV, is assigned to the nitrogen environment inside the triazine ring, as seen in melamine[138] and similarly the second peak at 400.1 eV is assigned to the nitrogen bridging environments, based on the amine groups in melamine[138]. These are the same peak assignments as seen in PTI. (Figure 3.5) The area of the peak at 399.4 eV is ~1.9 times more than the peak at 400.1 eV which is not in line with the 3:1 ratio expected for a perfect C_3N_4 structure suggesting a lower proportion of in-ring nitrogen positions compared to PTI.

The XPS survey, the relative positions and intensities of the C 1s and N 1s match well with that previously reported by Algara-Siller *et al.* They also report a peak at 286.7 eV in the C1s, this was assigned to nitrile bonding by Algara-Siller *et al.* however I suggest 64% of the non-adventitious carbon content being assigned to terminal groups is impractical even for a surface sensitive techniques such as XPS. No further interpretation or its ramifications on the proposed structure of TGCN is discussed in the report.

The profile of the XPS C1s reported by Ladva *et al*.[199] matches well with that shown in Figure 7.5 and also shows the largest area peak at 286.7 eV. They suggest that the environment is an indication of carbon bound to nitrogen in a CNH polymer, though the exact carbon environment is not concluded upon. However they also suggest that the peak positions are consistent with those reported in the review by Miller *et al*.[47] While this is correct, Miller *et al*.[47] also make clear that the intensity of the peak at 286.7 eV is always significantly smaller than the other C1s peaks. This is seen in the XPS of all the PTI investigated in this thesis (Figures 3.6, 3.7, 4.1, 4.8, 4.9, 4.11).

7.2.6 The C:N ratio and structural implications

	Only peak at 288.5 eV	Peaks at 286.7 and 288.5 eV	All peaks including the adventitious carbon
C:N composition	$C_{12}N_{26.5}$	$C_{12}N_{9.8}$	$C_{12}N_{5.7}$

Table 7.2. Carbon and nitrogen composition found from XPS. Different compositions depending on which environments from XPS are considered.

The C1s spectrum is distinctly different to that of the PTI materials I have observed in Chapter 3,4. Previously the peak at ~285.3 eV was assigned to the adventitious component, and therefore ignored when finding the C:N ratio from XPS. However, bulk CNH analysis suggests a much larger carbon content than observed for the PTI materials. Given that no unaccounted for nitrogen is typically found for PTI or carbon tape (Figure 3.5) I assume that all the nitrogen from figure 7.4c can be assigned to the flakes. To be able to correctly assign if the flakes have a significant amount of C-C bonding or if the peak at 285.3 eV is purely from adventitious carbon, C:N ratios were calculated using different combinations of the C1s peaks. (Table 7.2) This shows that if only the peak at 288.5 eV which is typically assigned to C=N-C bonding is assumed to be part of the structure, then the C:N composition is $C_{12}N_{26.5}$, which is unfeasible. If both non-adventitious peaks are included than the composition is $C_{12}N_9$, while if all the peaks are included then it is $C_{12}N_{5.7}$. From combustion analysis (Table 7.1) the C:N composition of the flakes were found to be $C_{12}N_{9.8}$, which matches well for that found from XPS from all the non-adventitious carbon environments. Therefore the only way to unify both the combustion analysis, XPS and C:N compositions is by assigning the preponderance of the peak at 285.3 eV to adventitious carbon. This leaves two distinct carbon environments with relative areas that do not match any known synthesised carbon nitride material, including the structure reported by Algara-Siller *et al.*

There have been several reports detailing calculations for a carbon nitride material with the composition C_4N_3,[203-205] matching the CNH analysis for our recovered material. These details computational investigations of a C_4N_3 material either based on a triazine or heptazine structure, with carbon taking the place of the bridging nitrogen N-(C)$_3$. The synthesis of a material composed of a single structure with a strict C_4N_3 composition has never been reported. A structure based on either a triazine or heptazine structure would be expected to have 2 carbon environments as seen from XPS, one as typically assigned to carbon nitrides (N-C=N) and the other C-(C)$_3$, with the relative intensity being 3:1. While I observe a bulk composition close to C_4N_3, XPS of our synthesised flakes indicate a 1:2 ratio of these environments. In addition a C_4N_3 structure would be expected to have only one nitrogen environment, the in-ring nitrogen position, while from N 1s we observe 2 peaks again with a ratio of 2:1. From this and the significant amount of N-H bonding as indicated from CNH analysis (Table 7.1) and IR (Figure 7.7) I suggest there is no indication of C_4N_3 structures. However the possibility of small C_4N_3 regions existing within the flake cannot be ruled out.

Given the carbon rich stoichiometry the C1s peak at 286.7 eV can be assigned to carbon sp^2 bonding to a combination of carbon and nitrogen atoms, such as in a nitrogen doped carbon (Figure 7.6). The peak at 288.5 eV can be assigned to carbon sp^2 bonded to three nitrogen atoms such as in typical carbon nitrides materials. The flakes could therefore be a combination of these two different carbon environments, both of which could be expected to structurally interlink to form layers.

From the above no significant graphitic C-C, C-O, nitrile bonding is expected in this structure. It is unclear if the flakes are a combination of two distinct structures, both carbon nitrides but one with a high carbon content and one more like the traditional carbon nitrides with a high nitrogen content, or if the entire flakes are a continuum of different types of carbon nitride bonding with no significant order to the bonding regime. If the flakes had two distinct structures then the small crystalline areas under TEM would be either the carbon nitride or the nitrogen doped carbon, with the amorphous areas constituting regions where the two overlapped significantly. If the flakes are formed of a continuum with different C-N/C-C bonding then the crystalline regions would represent small areas of a particular ‘accidental’ regular bonding regime and not an overall crystal structure. With many different crystalline regions existing on a spectrum between a C_3N_4 carbon nitride and a nitrogen doped carbon structure. These could be based on similar 6 membered graphitic structures, hence they could form a continuously bonded flake. If two distinct carbon nitride phases form a composite then I may expect to see crystalline XRD patterns of either or both phases. The XRD patterns of the flakes show no bulk crystallinity apart from a layered structure, and that the TEM images shows small nanocrystalline areas with different crystal structure. From this I suggest that a flake formed from a continuum of near randomly ordered C-C/C-N bonding, this amorphous structure would only display a broad graphitic peak under bulk XRD.

This structure could best be understood as a carbon doped carbon nitride (CDCN), where nitrogen positions are replaced with carbon with no particular ordering. The changing ratio between the two environments in the N 1s XPS indicates that the in-ring nitrogen positions are more likely to be doped than the bridging nitrogen. However given lack of order to this structure it most likely forming of a large variety of different small structural regimes bordering on a continuum.

It is not clear why the standard carbon nitride precursor DCDA has atypically formed a carbon rich layered structure. As explored in Section 1.2, the ternary diagram of carbon nitrides shows that they release NH_3 to loss nitrogen. However if all the NH_3 is lost then the composition will reach C_3N_4. To approach the composition $C_4N_{3,3}$ as seen in the flakes additional nitrogen would need to be lost, however no additional hydrogen would be available. The reaction proceeds at 600˚C, above that of the beginning of the decomposition of the carbon nitrides.[206] (Figure 3.12) At this temperature gas products including CNH species and C_2N_2 are formed.[199, 206] However both of these products would not significantly change the C:N ratio. While some other carbon nitride reactions occur at 600˚C (including the PTI, Section 3.2.1), these reactions typically last for only up to 12 hours (Section 3.2.1), while the method reported by Algara-Siller *et al.* is for 60 hours. The reaction conditions of the flakes occur in very similar conditions to the PTI but for much longer. If decomposition is happening during this time then a layered carbon nitride structure either based on, or similar to, PTI would be expected to decompose. I speculate that the CNH/C_2N_2 decomposition products react within the high pressure sealed ampoule to form N_2 gas, which would not react further due to its stability. Interestingly the presence of gas with the same molecular mass as N_2 is observed by Ladva *et al*.[199] in their mass spectrometry of the decomposition products of DCDA. This would leave a gaseous carbon rich environment within the ampoule that could via a chemical vapour deposition route form a continuous film of C-C/C-N bonding. Interestingly this CVD method is exactly the method followed by Ladva *et al*.[199] which produced a carbon nitride material the data of which is very similar to the flakes explored in this report even though it was suggested to be a layered CNH polymer.

This speculation is intended only to understand what may be causing the formation of a carbon rich layered material in this environment and should not be taken as a mechanism. Without further investigation of the composition of the gas phase and in particular if N_2 is formed within the ampoule during the reaction a mechanism may not be possible.

7.2.7 IR and Raman studies

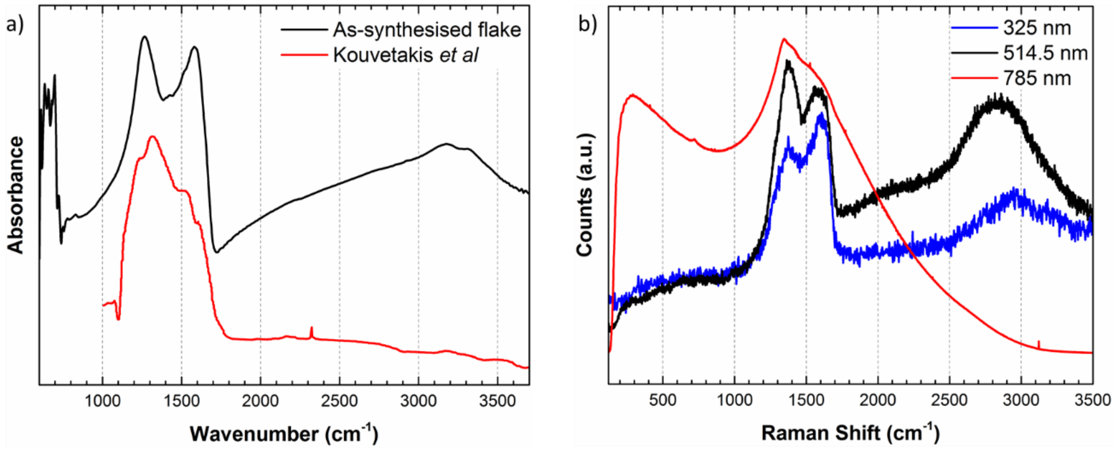

Figure 7.7. Comparison of the IR and Raman spectra of the synthesised flakes and similar literature structures. a) IR spectrum for nanocrystalline C_3N_4 prepared by CVD synthesis redrawn from Ref,[51, 52] (red curve) IR spectrum for the synthesised flakes. (black curve) b) Unpolarized Raman spectra obtained at normal incidence using different laser excitation wavelengths (325, 514.5, 785 nm) for the synthesised flakes.

The FTIR spectrum reported by Kouvetakis *et al.*[51, 52] (Figure 7.7a red curve) for nanocrystalline C_3N_4 triazine-based thin films shows a broad region between 1100 – 1700 cm^{-1} that can largely be assigned to C-N stretching bands. No N-H stretching features are observed, this is to be expected for a fully condensed C_3N_4 structure prepared from H-free precursors by CVD. [51, 52] The C-N stretching vibrations of flakes prepared in our study (Figure 7.7a black curve) also span the same wavenumber range as that reported by Kouvetakis *et al.*[51, 52] Two distinct peaks at 1250 and 1600 cm^{-1} are observed that appear similar to D and G peaks in graphite and nitrogen doped graphene.[207] These are most likely are due to the range of different C-C/C-N bonding that is occurring in the material. I do not observe any indication of the typical carbon nitride peak at 800 cm^{-1} that is assigned to 6 membered C_3N_3 ring out-of-plane bending vibration.[47, 59, 142] This may be an indication that the structure of the flakes is significantly disordered compared to most carbon nitrides. The flakes also exhibit a strong, broad absorption feature in the 3000 - 3400 cm^{-1} region with two maxima at 3179 and 3311 cm^{-1}. These correspond closely to the N-H stretching vibrations observed for PTI.LiBr and PTI.LiCl (Figure 3.8).[54, 56] It is clear that the synthesised flakes have significant C-N and N-H bonding, with the latter having similar local environments to those observed in PTI.LiBr or PTI.LiCl compounds.[54, 56]

Microbeam Raman spectra for the flakes were recorded using excitation wavelengths extending from the near-IR (785 nm) through the visible (514.5 nm) to the UV region (325 nm) (Figure 7.7 b). It is known from studies of layered carbonaceous materials including gCN that the appearance of the spectra and hence their structural interpretation depends on the excitation wavelength.[141, 146-148] These effects have been seen in the Raman spectra of PTI (Figure 3.9). UV-Raman spectra of the flakes exhibit two main peaks near 1700 and 1300 cm^{-1}. Similar features are typically assigned to the "G" and "D" features observed for graphitic carbon, graphene and gCN materials. [141, 146-148] The profile of the spectra appears very similar to that of the PTI, apart from the lack of the peak at 1000 cm^{-1}. (Figure 3.9) Peaks in the 1000-1100 cm^{-1} region appear in the Raman spectra of PTI.HCl,[130] PTI.LiCl and PTI.LiBr. (Figure 3.9) The lack of the peak at 1000 cm^{-1} which is typically associated with vibrations of the triazine and heptazine ring structures suggests a significant distortion from the carbon nitride structures I have previously observed. However without a clear structure with which to model the Raman spectra I cannot understand why this peak is missing.

7.3 Conclusions

This chapter has detailed the synthesis and characterization of a layered carbon nitride material. The initial aim was to investigate the material reported by Algara-Siller *et al.*, including characterization via SEM, TEM, XRD, XPS and CNH analysis. These indicated that the synthesized flakes are not a crystalline material based on a uniform carbon nitride structure like those reported by Kouvetakis *et al.*[51, 52] and Algara-Siller *et al.*[41] They are rather a composite of different structures that could be best modelled by carbon doped carbon nitride (CDCN). Leading to micron sized flakes with a high carbon content for carbon nitrides, a significant N-H bonding component and no clear regular structure. Given a curious mix of similarities and differences between our data and that reported by Algara-Siller *et al.* it is not clear if by following the reported synthesis I have formed the same material or not. However it is clear that the data reported by Ladva *et al*.[199] matches closely with that observed in this thesis. In addition potential mechanism for the synthesis of the flakes in this thesis matches well with the synthetic method reported. From this I would suggest that the work done here, by Ladva *et al*.[199] and Algara-Siller *et al.*[41] all have synthesized carbon nitride materials of the same family and are structurally related, and that they should be more directly compared within the literature.

Chapter 8 – Conclusion and outlook

This thesis has dealt with the synthesis, characterisation, intercalation and exfoliation of a series of layered crystalline carbon nitride materials. This subset of carbon nitrides is less well reported than the amorphous variety, and has been well characterised in this thesis. This allowed a series of innovative intercalation and exfoliation methods to be employed, manipulating the structure of PTI.

Chapter 3 explored the synthesis and characterisation of two structurally analogues materials, PTI.LiBr and PTI.LiCl. These crystalline layered carbon nitrides are formed by triazine units linked by amine bridges. As a result of their synthesis in a eutectic salt mix intercalants are found between and within the layers. Extensive characterisation of these were performed showing that these material were based on the same carbon nitride backbone which adapted to allow the change of halide intercalant. This also gave the reader a strong grounding in this material in preparation for Chapters 4,5,6.

Chapter 4 explored a series of de-intercalation and re-intercalation procedures for the synthesis of different PTI structures. The intercalants of PTI.LiX were removed forming a true carbon nitride analogue of graphite, IF-PTI. Re-intercalation experiments with IF-PTI showed that a variety of different materials could intercalate into the layered structure, these occurred without significant damage to the material. The intercalants have also been shown to have a significant effect on the electronic properties of the PTI. This method therefore allows the tuning of PTI via the reversible and non-damaging de-intercalation and re-intercalation procedure developed during the PhD and explored in this thesis.

Chapter 5 followed a series of exfoliation procedures, finding, remarkably that PTI.LiBr and PTI.LiCl both spontaneously exfoliate when contacted with select organic polar solvents. HR-TEM images and AFM data of nanosheet-solvent solutions showed isolated stacks of PTI. The intercalated ions were found to have not been disrupted by the exfoliation procedure. These stacks were found to be an average of 8-9 layers thick with a narrow height distribution. I observed indications of an electron confinement effect with the excitation/emission spectra of the nanosheets depending on the number of layers within a stack. This could allow tuning of the photoemission spectrum of the solutions, making these potential LED materials. This damagless exfoliation route has resulted for the first time in stable PTI nanosheet solutions without the need for sonication, centrifugation or agitation.

Chapter 6 showed that PTI.LiX spontaneously dissolved when exposed to water. As with the organic solvents PTI nanosheets were observed, however they were found to be thicker than those seen in Chapter 5. The concentration of the resulting solutions was found unusually, to depend not only on pH but also on the initial mass of PTI. The electronic properties of the dissolved nanosheets appear to be dependent on the pH, most likely due to protonation/deprotonation of the PTI framework. This has yielded a potential scaleable processing route for PTI in an aqueous solution.

Chapter 7 was an attempt to follow the synthesis previously reported crystalline carbon nitride material TGCN. While the recovered material visually matched well with the literature there were some also discrepancies with the characterisation. The synthesised flakes were found to be layered and non-crystalline, with a suggested structure based on a carbon doped carbon nitride (CDCN). The characterisation was unable to elucidate the exact structure, and I suggest that a range of different C-N/C-C bonding regimes co-exist within a single layer. From this work is in unclear if the synthesis was able to successfully reproduce TGCN as reported by Algara-Siller *et al.*[41]. However this work has elucidated the structure a potentially interesting carbon nitride structure that may be able to be synthesised via CVD.

Overall the potential of the crystalline layered carbon nitrides was explored by investigating how effect intercalation and exfoliation had on the properties and structure of the material. This showed that both exfoliation and intercalation could be used to tune the properties without damaging the structure of the material. PTI is a highly corrosive resistant crystalline porous layered material that has the potential for be useful for many different applications. This thesis has developed several methods for fine tuning the properties of the PTI to make them more attractive for a variety of applications.

Chapter 9 – Appendix

9.1 Collection of TEM images of the flakes discussed in Chapter 7

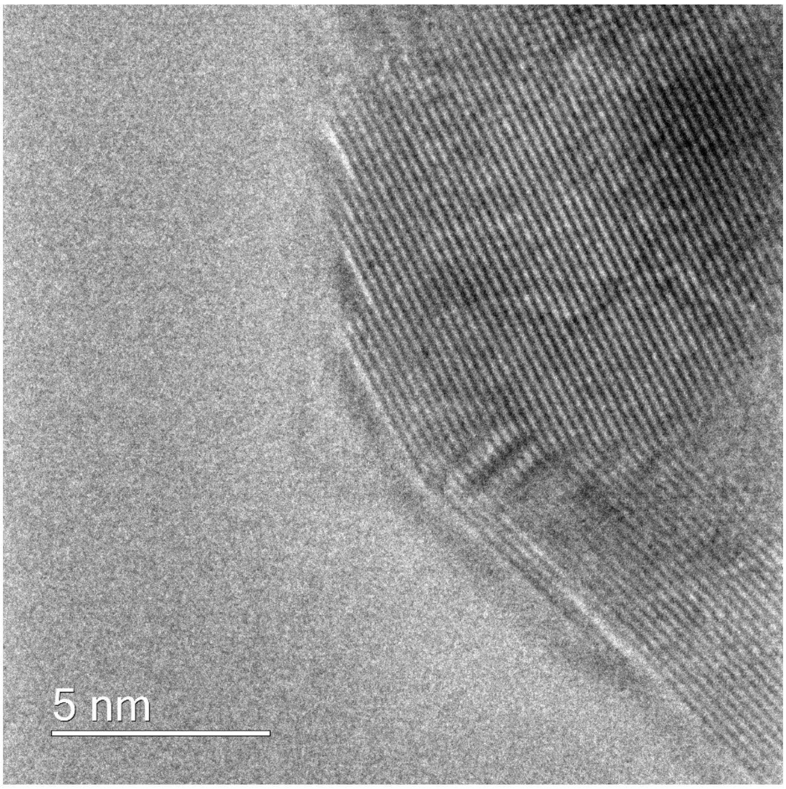

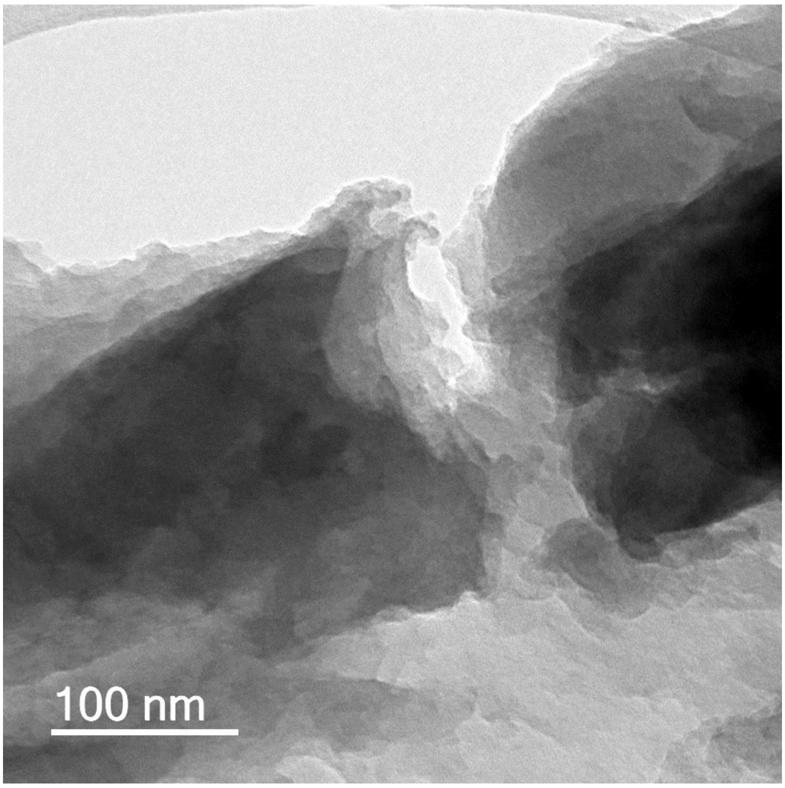

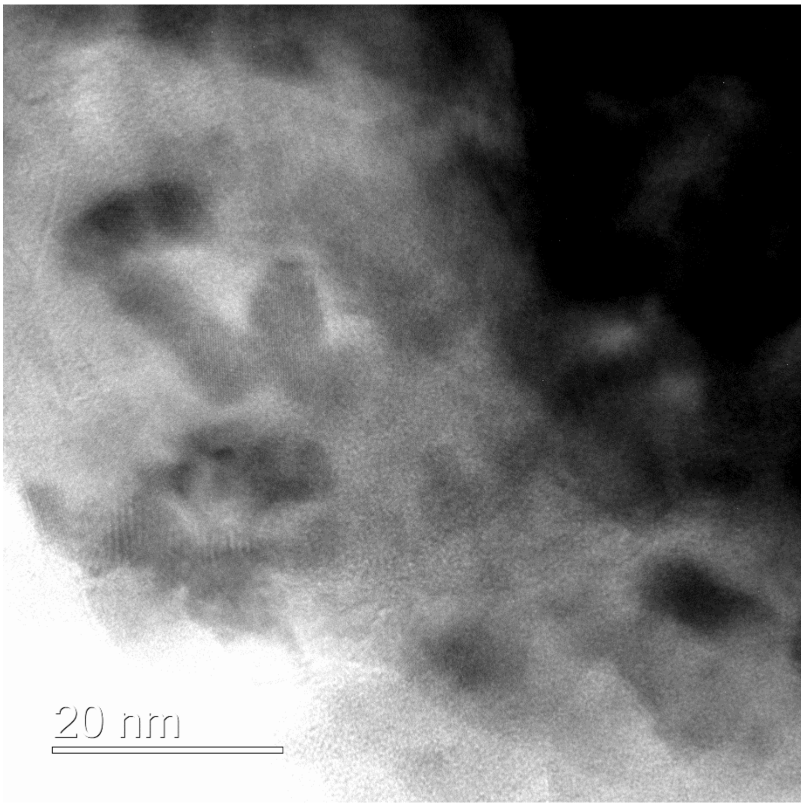
20 nm

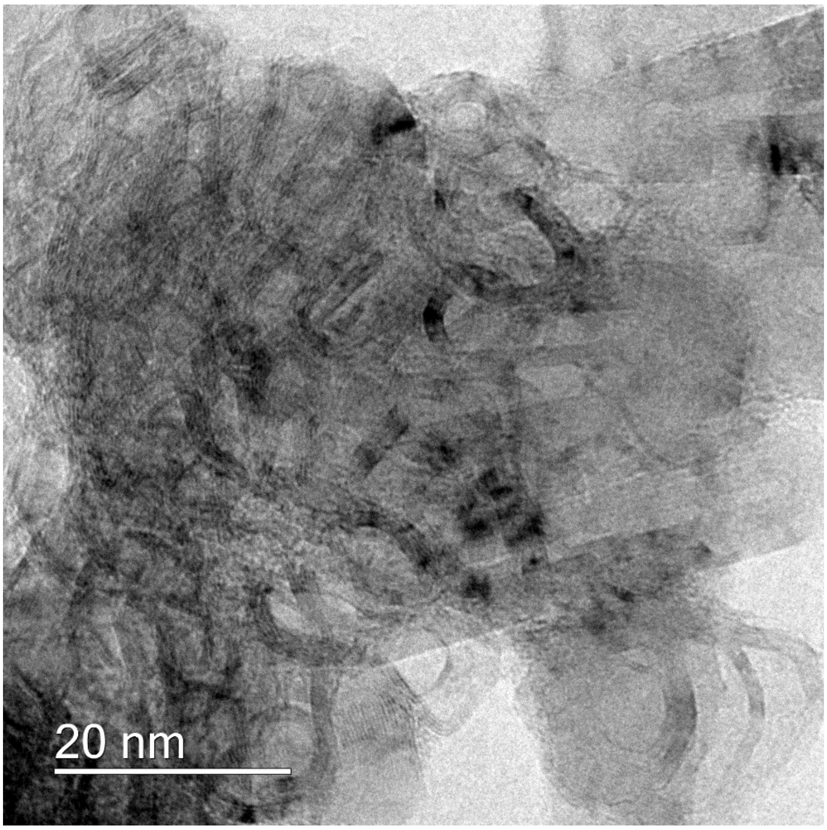
20 nm

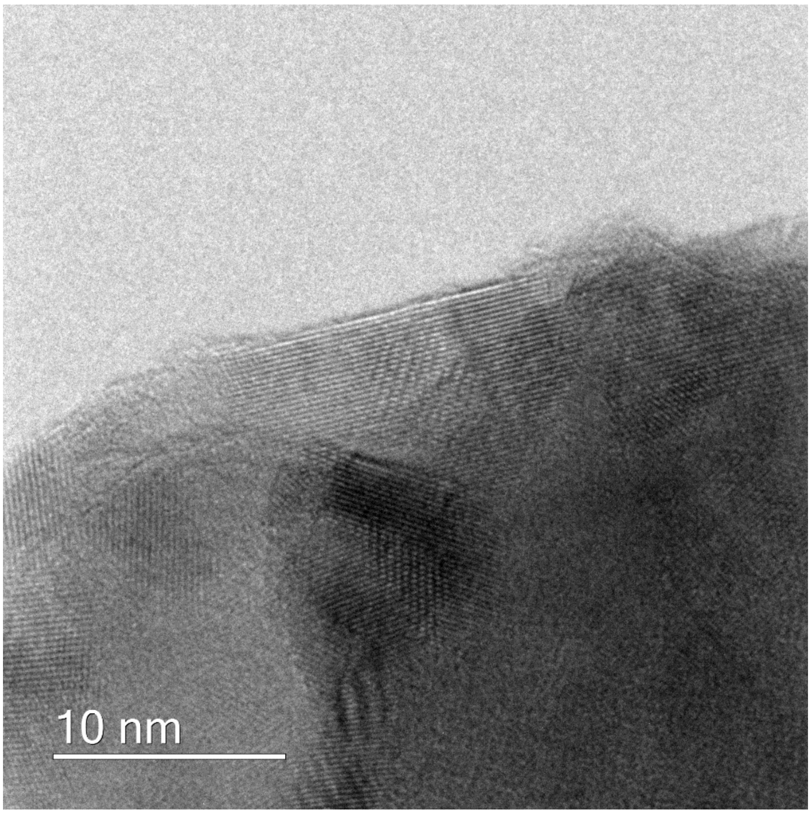
10 nm

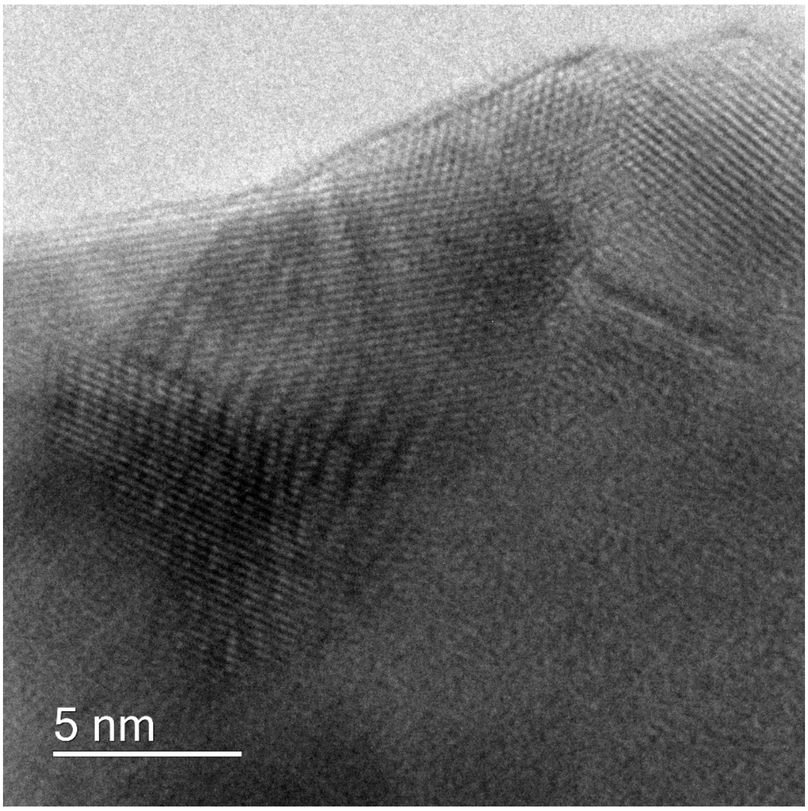
5 nm

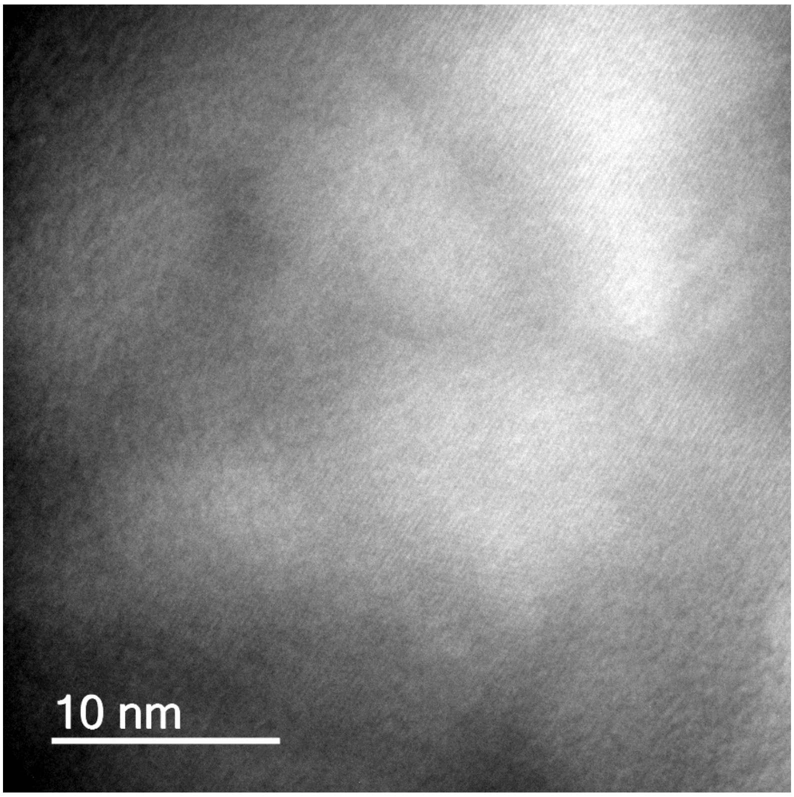
10 nm

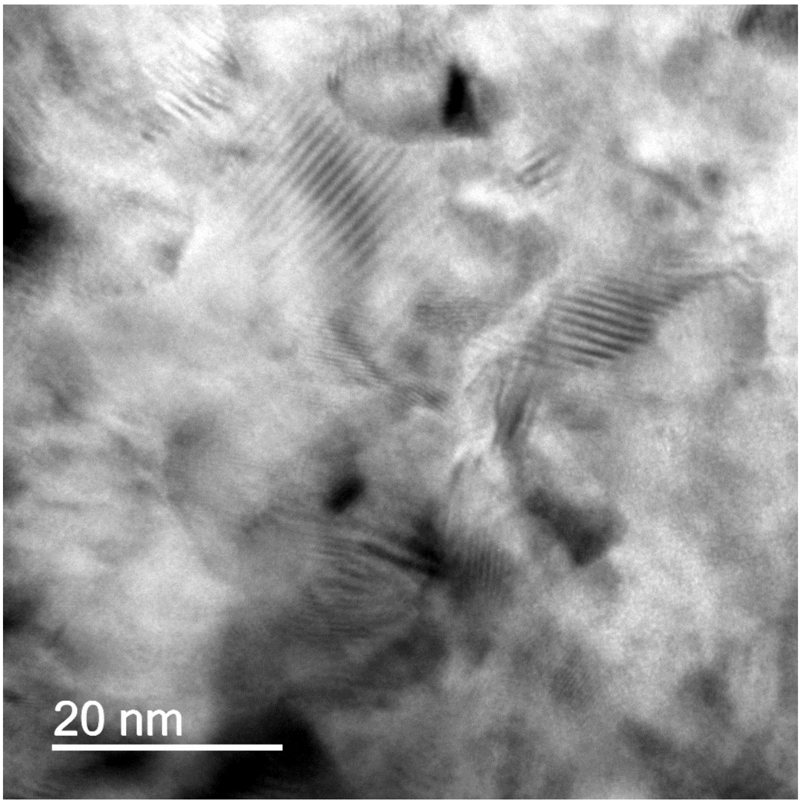
20 nm

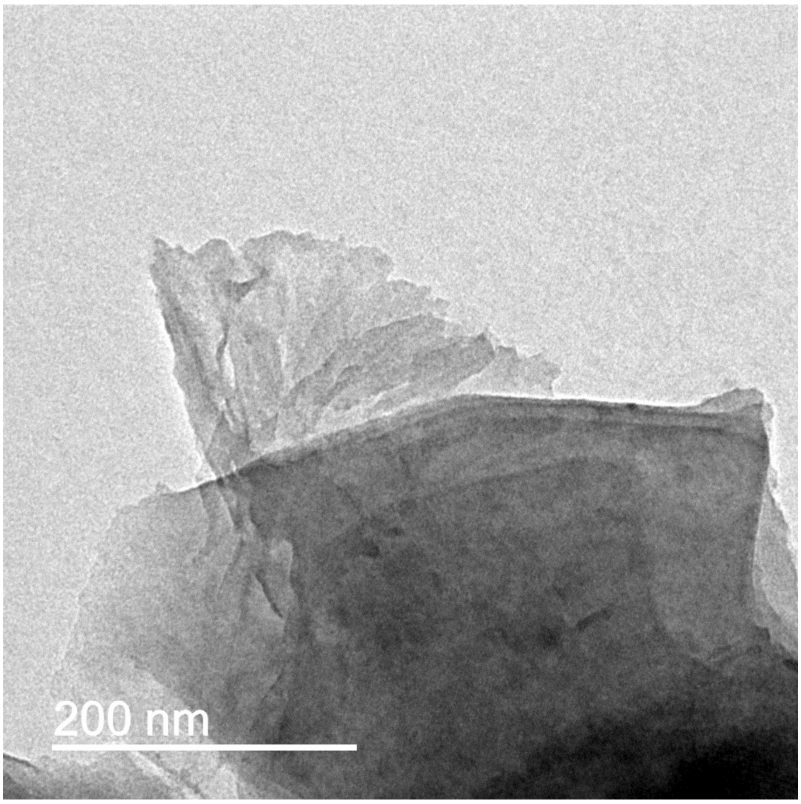
200 nm

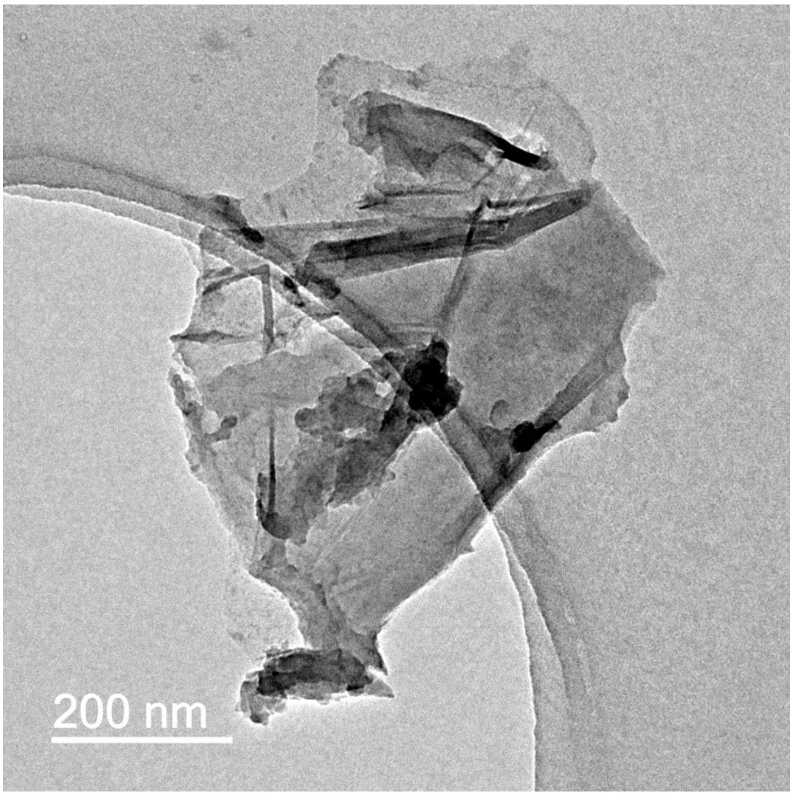
200 nm

References

1. D. Ford, *Journal*, 2015.
2. H. L. Wang, L. S. Zhang, Z. G. Chen, J. Q. Hu, S. J. Li, Z. H. Wang, J. S. Liu and X. C. Wang, *Chem Soc Rev*, 2014, **43**, 5234-5244.
3. Y. Wang, X. C. Wang and M. Antonietti, *Angew Chem Int Ed Engl*, 2012, **51**, 68-89.
4. H. Tong, S. X. Ouyang, Y. P. Bi, N. Umezawa, M. Oshikiri and J. H. Ye, *Adv Mater*, 2012, **24**, 229-251.
5. A. Kudo and Y. Miseki, *Chem Soc Rev*, 2009, **38**, 253-278.
6. U. I. Gaya and A. H. Abdullah, *J Photoch Photobio C*, 2008, **9**, 1-12.
7. M. N. Chong, B. Jin, C. W. K. Chow and C. Saint, *Water Res*, 2010, **44**, 2997-3027.
8. J. M. Herrmann, *Catal Today*, 1999, **53**, 115-129.
9. S. N. Habisreutinger, L. Schmidt-Mende and J. K. Stolarczyk, *Angew Chem Int Ed Engl*, 2013, **52**, 7372-7408.
10. P. Usubharatana, D. McMartin, A. Veawab and P. Tontiwachwuthikul, *Ind Eng Chem Res*, 2006, **45**, 2558-2568.
11. R. de Richter, T. Z. Ming, P. Davies, W. Liu and S. Caillol, *Prog Energ Combust*, 2017, **60**, 68-96.
12. W. G. Tu, Y. Zhou, Q. Liu, Z. P. Tian, J. Gao, X. Y. Chen, H. T. Zhang, J. G. Liu and Z. G. Zou, *Adv Funct Mater*, 2012, **22**, 1215-1221.
13. R. Asahi, T. Morikawa, T. Ohwaki, K. Aoki and Y. Taga, *Science*, 2001, **293**, 269-271.
14. K. Maeda, K. Teramura, D. L. Lu, T. Takata, N. Saito, Y. Inoue and K. Domen, *Nature*, 2006, **440**, 295-295.
15. F. E. Osterloh, *Chem Mater*, 2008, **20**, 35-54.
16. A. Kubacka, M. Fernandez-Garcia and G. Colon, *Chem Rev*, 2012, **112**, 1555-1614.
17. B. Oregan and M. Gratzel, *Nature*, 1991, **353**, 737-740.
18. Q. H. Wang, K. Kalantar-Zadeh, A. Kis, J. N. Coleman and M. S. Strano, *Nat Nanotechnol*, 2012, **7**, 699-712.
19. J. Burschka, N. Pellet, S. J. Moon, R. Humphry-Baker, P. Gao, M. K. Nazeeruddin and M. Gratzel, *Nature*, 2013, **499**, 316-+.
20. L. D. Landau, E. M. Lifshit͡s and L. P. Pitaevskiĭ, *Statistical physics*, Pergamon Press, Oxford ; New York, 1980.
21. L. D. Landau, *Phys. Z. Sowjetunion* 1937, **11**, 26-35.
22. R. E. Peierls, *Helvetica Physica Acta*, 1934, 81-83.
23. R. E. Peierls, *Annales de l'Institut Henri Poincaré*, 1935, 177-222.
24. G. Ruess and F. Vogt, *Monatshefte für Chemie und verwandte Teile anderer Wissenschaften*, 1948, **78**, 222-242.
25. H. P. Boehm, A. Clauss, G. O. Fischer and U. Hofmann, *Z Anorg Allg Chem*, 1962, **316**, 119-127.
26. A. K. Geim and K. S. Novoselov, *Nat Mater*, 2007, **6**, 183-191.
27. K. S. Novoselov, A. K. Geim, S. V. Morozov, D. Jiang, Y. Zhang, S. V. Dubonos, I. V. Grigorieva and A. A. Firsov, *Science*, 2004, **306**, 666-669.
28. J. C. Meyer, A. K. Geim, M. I. Katsnelson, K. S. Novoselov, T. J. Booth and S. Roth, *Nature*, 2007, **446**, 60-63.
29. *Journal*, 2017.
30. H. B. Wang, T. Maiyalagan and X. Wang, *Acs Catal*, 2012, **2**, 781-794.
31. G. K. Dimitrakakis, E. Tylianakis and G. E. Froudakis, *Nano Lett*, 2008, **8**, 3166-3170.
32. G. X. Wang, X. P. Shen, J. Yao and J. Park, *Carbon*, 2009, **47**, 2049-2053.
33. K. K. Kam and B. A. Parkinson, *J Phys Chem-Us*, 1982, **86**, 463-467.

34. S. X. Wu, Z. Y. Zeng, Q. Y. He, Z. J. Wang, S. J. Wang, Y. P. Du, Z. Y. Yin, X. P. Sun, W. Chen and H. Zhang, *Small*, 2012, **8**, 2264-2270.
35. B. Radisavljevic, A. Radenovic, J. Brivio, V. Giacometti and A. Kis, *Nat Nanotechnol*, 2011, **6**, 147-150.
36. A. B. Jorge, D. J. Martin, M. T. S. Dhanoa, A. S. Rahman, N. Makwana, J. W. Tang, A. Sella, F. Cora, S. Firth, J. A. Darr and P. F. McMillan, *J Phys Chem C*, 2013, **117**, 7178-7185.
37. A. Thomas, A. Fischer, F. Goettmann, M. Antonietti, J. O. Muller, R. Schlogl and J. M. Carlsson, *J Mater Chem*, 2008, **18**, 4893-4908.
38. E. J. McDermott, E. Wirnhier, W. Schnick, K. S. Virdi, C. Scheu, Y. Kauffmann, W. D. Kaplan, E. Z. Kurmaev and A. Moewes, *J Phys Chem C*, 2013, **117**, 8806-8812.
39. F. Dong, L. W. Wu, Y. J. Sun, M. Fu, Z. B. Wu and S. C. Lee, *J Mater Chem*, 2011, **21**, 15171-15174.
40. M. Deifallah, P. F. McMillan and F. Cora, *J Phys Chem C*, 2008, **112**, 5447-5453.
41. G. Algara-Siller, N. Severin, S. Y. Chong, T. Bjorkman, R. G. Palgrave, A. Laybourn, M. Antonietti, Y. Z. Khimyak, A. V. Krasheninnikov, J. P. Rabe, U. Kaiser, A. I. Cooper, A. Thomas and M. J. Bojdys, *Angew Chem Int Ed Engl*, 2014, **53**, 7450-7455.
42. M. C. Rong, L. P. Lin, X. H. Song, Y. R. Wang, Y. X. Zhong, J. W. Yan, Y. F. Feng, X. Y. Zeng and X. Chen, *Biosens Bioelectron*, 2015, **68**, 210-217.
43. Z. J. Li, J. H. Wang, K. X. Zhu, F. L. Ma and A. Meng, *Mater Lett*, 2015, **145**, 167-170.
44. X. L. Zhang, C. Zheng, S. S. Guo, J. Li, H. H. Yang and G. N. Chen, *Anal Chem*, 2014, **86**, 3426-3434.
45. X. D. Zhang, X. Xie, H. Wang, J. J. Zhang, B. C. Pan and Y. Xie, *J Am Chem Soc*, 2013, **135**, 18-21.
46. E. Kroke, M. Schwarz, E. Horath-Bordon, P. Kroll, B. Noll and A. D. Norman, *New J Chem*, 2002, **26**, 508-512.
47. T. S. Miller, A. B. Jorge, T. M. Suter, A. Sella, F. Cora and P. F. McMillan, *Phys Chem Chem Phys*, 2017, **19**, 15613-15638.
48. Y. J. Ma, Y. Bian, P. F. Tan, Y. Y. Shang, Y. Liu, L. D. Wu, A. Q. Zhu, W. W. Liu, X. Xiong and J. Pan, *J Colloid Interf Sci*, 2017, **497**, 144-154.
49. H. F. Xu, S. J. Liang, X. Zhu, X. Q. Wu, Y. Q. Dong, H. S. Wu, W. X. Zhang and Y. W. Chi, *Biosens Bioelectron*, 2017, **92**, 695-701.
50. B. Pant, M. Park, J. H. Lee, H. Y. Kim and S. J. Park, *J Colloid Interf Sci*, 2017, **496**, 343-352.
51. J. Kouvetakis, A. Bandari, M. Todd, B. Wilkens and N. Cave, *Chem Mater*, 1994, **6**, 811-814.
52. M. Todd, J. Kouvetakis, T. L. Groy, D. Chandrasekhar, D. J. Smith and P. W. Deal, *Chem Mater*, 1995, **7**, 1422-1426.
53. E. Kroke and M. Schwarz, *Coord Chem Rev*, 2004, **248**, 493-532.
54. S. Y. Chong, J. T. A. Jones, Y. Z. Khimyak, A. I. Cooper, A. Thomas, M. Antonietti and M. J. Bojdys, *J Mater Chem A*, 2013, **1**, 1102-1107.
55. M. B. Mesch, K. Bärwinkel, Y. Krysiak, C. Martineau, F. Taulelle, R. B. Neder, U. Kolb and J. Senker, *Chemistry – A European Journal*, 2016, **22**, 16878-16890.
56. E. Wirnhier, M. Doblinger, D. Gunzelmann, J. Senker, B. V. Lotsch and W. Schnick, *Chem-Eur J*, 2011, **17**, 3213-3221.
57. J. Liebig, *Annalen der Pharmacie*, 1834, **10**, 1-47.
58. H. May, *Journal of Applied Chemistry*, 1959, **9**, 340-344.
59. B. V. Lotsch, M. Doblinger, J. Sehnert, L. Seyfarth, J. Senker, O. Oeckler and W. Schnick, *Chem-Eur J*, 2007, **13**, 4969-4980.
60. F. Fina, S. K. Callear, G. M. Carins and J. T. S. Irvine, *Chem Mater*, 2015, **27**, 2612-2618.

61. L. Wang, S. Dou, J. T. Xu, H. K. Liu, S. Y. Wang, J. M. Ma and S. X. Dou, *Chem. Commun.*, 2015, **51**, 11791-11794.
62. K. Y. Jiang, A. Eitan, L. S. Schadler, P. M. Ajayan, R. W. Siegel, N. Grobert, M. Mayne, M. Reyes-Reyes, H. Terrones and M. Terrones, *Nano Lett*, 2003, **3**, 275-277.
63. Y. Wang, Y. Y. Shao, D. W. Matson, J. H. Li and Y. H. Lin, *Acs Nano*, 2010, **4**, 1790-1798.
64. L. P. Zhang and Z. H. Xia, *J Phys Chem C*, 2011, **115**, 11170-11176.
65. F. Goettmann, A. Fischer, M. Antonietti and A. Thomas, *Chem. Commun.*, 2006, DOI: 10.1039/b608532f, 4530-4532.
66. Y. Wang, X. Wang and M. Antonietti, *Angewandte Chemie International Edition*, 2012, **51**, 68-89.
67. S. W. Cao, J. X. Low, J. G. Yu and M. Jaroniec, *Adv Mater*, 2015, **27**, 2150-2176.
68. M. Y. Ding, W. Wang, Y. J. Zhou, C. H. Lu, Y. Ni and Z. Z. Xu, *J Alloys Compd*, 2015, **635**, 34-40.
69. Z. F. Jiang, D. L. Jiang, Z. X. Yan, D. Liu, K. Qian and J. M. Xie, *Appl Catal B*, 2015, **170**, 195-205.
70. S. B. Yang, Y. J. Gong, J. S. Zhang, L. Zhan, L. L. Ma, Z. Y. Fang, R. Vajtai, X. C. Wang and P. M. Ajayan, *Adv Mater*, 2013, **25**, 2452-2456.
71. J. Liu, Y. Liu, N. Y. Liu, Y. Z. Han, X. Zhang, H. Huang, Y. Lifshitz, S. T. Lee, J. Zhong and Z. H. Kang, *Science*, 2015, **347**, 970-974.
72. Y. W. Zhang, J. H. Liu, G. Wu and W. Chen, *Nanoscale*, 2012, **4**, 5300-5303.
73. Z. W. Zhao, Y. J. Sun and F. Dong, *Nanoscale*, 2015, **7**, 15-37.
74. X. C. Wang, K. Maeda, A. Thomas, K. Takanabe, G. Xin, J. M. Carlsson, K. Domen and M. Antonietti, *Nat Mater*, 2009, **8**, 76-80.
75. X. Lu, Q. Wang and D. Cui, *Journal of Materials Science & Technology*, 2010, **26**, 925-930.
76. X. Zhou, F. Peng, H. Wang, H. Yu and Y. Fang, *Chem. Commun.*, 2011, **47**, 10323-10325.
77. N. Yang, G. Li, W. Wang, X. Yang and W. F. Zhang, *J Phys Chem Solids*, 2011, **72**, 1319-1324.
78. H. Yan and H. Yang, *J Alloys Compd*, 2011, **509**, L26-L29.
79. X. Zhou, B. Jin, L. Li, F. Peng, H. Wang, H. Yu and Y. Fang, *J Mater Chem*, 2012, **22**, 17900-17905.
80. Y. Guo, F. Kong, S. Chu, L. Luo, J. Yang, Y. Wang and Z. Zou, *Rsc Adv*, 2012, **2**, 5585-5590.
81. J. Wang and W.-D. Zhang, *Electrochim. Acta*, 2012, **71**, 10-16.
82. S. Zhao, S. Chen, H. Yu and X. Quan, *Separation and Purification Technology*, 2012, **99**, 50-54.
83. J. Yu, S. Wang, J. Low and W. Xiao, *Phys Chem Chem Phys*, 2013, **15**, 16883-16890.
84. X.-j. Wang, W.-y. Yang, F.-t. Li, Y.-b. Xue, R.-h. Liu and Y.-j. Hao, *Ind Eng Chem Res*, 2013, **52**, 17140-17150.
85. S. Zhou, Y. Liu, J. Li, Y. Wang, G. Jiang, Z. Zhao, D. Wang, A. Duan, J. Liu and Y. Wei, *Applied Catalysis B: Environmental*, 2014, **158–159**, 20-29.
86. L. Gu, J. Wang, Z. Zou and X. Han, *J Hazard Mater*, 2014, **268**, 216-223.
87. N. Boonprakob, N. Wetchakun, S. Phanichphant, D. Waxler, P. Sherrell, A. Nattestad, J. Chen and B. Inceesungvorn, *J Colloid Interf Sci*, 2014, **417**, 402-409.
88. L. Zhang, D. Jing, X. She, H. Liu, D. Yang, Y. Lu, J. Li, Z. Zheng and L. Guo, *J Mater Chem A*, 2014, **2**, 2071-2078.
89. S. Obregón and G. Colón, *Applied Catalysis B: Environmental*, 2014, **144**, 775-782.
90. Y. Lan, X. Qian, C. Zhao, Z. Zhang, X. Chen and Z. Li, *J Colloid Interf Sci*, 2013, **395**, 75-80.
91. J. Yan, H. Xu, Y. Xu, C. Wang, Y. Song, J. Xia and H. Li, *J Nanosci Nanotechno*, 2014, **14**, 6809-6815.

92. T. Zhou, Y. Xu, H. Xu, H. Wang, Z. Da, S. Huang, H. Ji and H. Li, *Ceram Int*, 2014, **40**, 9293-9301.
93. Y. Zang, L. Li, Y. Zuo, H. Lin, G. Li and X. Guan, *Rsc Adv*, 2013, **3**, 13646-13650.
94. K.-i. Katsumata, R. Motoyoshi, N. Matsushita and K. Okada, *J Hazard Mater*, 2013, **260**, 475-482.
95. L. Huang, H. Xu, Y. Li, H. Li, X. Cheng, J. Xia, Y. Xu and G. Cai, *Dalton T*, 2013, **42**, 8606-8616.
96. Z. Jin, N. Murakami, T. Tsubota and T. Ohno, *Applied Catalysis B: Environmental*, 2014, **150–151**, 479-485.
97. S. Chen, Y. Hu, S. Meng and X. Fu, *Applied Catalysis B: Environmental*, 2014, **150–151**, 564-573.
98. H. Katsumata, Y. Tachi, T. Suzuki and S. Kaneco, *Rsc Adv*, 2014, **4**, 21405-21409.
99. M. Kim, S. Hwang and J. S. Yu, *J Mater Chem*, 2007, **17**, 1656-1659.
100. N. Mansor, A. B. Jorge, F. Cora, C. Gibbs, R. Jervis, P. F. McMillan, X. C. Wang and D. J. L. Brettt, *J Phys Chem C*, 2014, **118**, 6831-6838.
101. Z. H. Chen, P. Sun, B. Fan, Q. Liu, Z. G. Zhang and X. M. Fang, *Appl Catal B*, 2015, **170**, 10-16.
102. Z. C. Yang, J. Li, F. X. Cheng, Z. Chen and X. P. Dong, *J Alloys Compd*, 2015, **634**, 215-222.
103. Q. B. Wang, W. Wang, J. P. Lei, N. Xu, F. L. Gao and H. X. Ju, *Anal Chem*, 2013, **85**, 12182-12188.
104. M. Shalom, S. Inal, C. Fettkenhauer, D. Neher and M. Antonietti, *J Am Chem Soc*, 2013, **135**, 7118-7121.
105. Y. Ham, K. Maeda, D. Cha, K. Takanabe and K. Domen, *Chem-Asian J*, 2013, **8**, 218-224.
106. H. Zhang, F. Liu, Z. G. Mou, X. F. Liu, J. H. Sun and W. W. Lei, *Chem. Commun.*, 2016, **52**, 13020-13023.
107. M. K. Bhunia, S. Melissen, M. R. Parida, P. Sarawade, J. M. Basset, D. H. Anjum, O. F. Mohammed, P. Sautet, T. Le Bahers and K. Takanabe, *Chem Mater*, 2015, **27**, 8237-8247.
108. M. K. Bhunia, K. Yamauchi and K. Takanabe, *Angew Chem Int Ed Engl*, 2014, **53**, 11001-11005.
109. K. Schwinghammer, B. Tuffy, M. B. Mesch, E. Wirnhier, C. Martineau, F. Taulelle, W. Schnick, J. Senker and B. V. Lotsch, *Angew Chem Int Ed Engl*, 2013, **52**, 2435-2439.
110. W. R. Lee, Y. S. Jun, J. Park and G. D. Stucky, *J Mater Chem A*, 2015, **3**, 24232-24236.
111. Y. L. Zhang, L. L. Hu, C. Zhu, J. Liu, H. Huang, Y. Liu and Z. H. Kang, *Catal Sci Technol*, 2016, **6**, 7252-7258.
112. Y. Wang, Q. Y. Yang, C. L. Zhong and J. P. Li, *J Phys Chem C*, 2016, **120**, 28782-28788.
113. A. Ciesielski and P. Samori, *Chem Soc Rev*, 2014, **43**, 381-398.
114. J. Ding, Q. Q. Liu, Z. Y. Zhang, X. Liu, J. Q. Zhao, S. B. Cheng, B. N. Zong and W. L. Dai, *Appl Catal B*, 2015, **165**, 511-518.
115. Z. Y. Xia, S. Pezzini, E. Treossi, G. Giambastiani, F. Corticelli, V. Morandi, A. Zanelli, V. Bellani and V. Palermo, *Adv Funct Mater*, 2013, **23**, 4684-4693.
116. B. C. Brodie, *Philosophical Transactions of the Royal Society of London*, 1859, **149**, 249-259.
117. N. I. Kovtyukhova, T. E. Mallouk, L. Pan and E. C. Dickey, *J Am Chem Soc*, 2003, **125**, 9761-9769.
118. S. Fogden, C. A. Howard, R. K. Heenan, N. T. Skipper and M. S. P. Shaffer, *Acs Nano*, 2012, **6**, 54-62.
119. E. M. Milner, N. T. Skipper, C. A. Howard, M. S. P. Shaffer, D. J. Buckley, K. A. Rahnejat, P. L. Cullen, R. K. Heenan, P. Lindner and R. Schweins, *J Am Chem Soc*, 2012, **134**, 8302-8305.

120. A. B. Bourlinos, V. Georgakilas, R. Zboril, T. A. Steriotis and A. K. Stubos, *Small*, 2009, **5**, 1841-1845.
121. B. Kim, Y. H. Lee, J. H. Ryu and K. D. Suh, *Colloid Surface A*, 2006, **273**, 161-164.
122. W. S. Hummers and R. E. Offeman, *J Am Chem Soc*, 1958, **80**, 1339-1339.
123. S. Jeong, D. Yoo, M. Ahn, P. Miro, T. Heine and J. Cheon, *Nat Commun*, 2015, **6**.
124. J. N. Coleman, *Adv Funct Mater*, 2009, **19**, 3680-3695.
125. J. N. Coleman, M. Lotya, A. O'Neill, S. D. Bergin, P. J. King, U. Khan, K. Young, A. Gaucher, S. De, R. J. Smith, I. V. Shvets, S. K. Arora, G. Stanton, H. Y. Kim, K. Lee, G. T. Kim, G. S. Duesberg, T. Hallam, J. J. Boland, J. J. Wang, J. F. Donegan, J. C. Grunlan, G. Moriarty, A. Shmeliov, R. J. Nicholls, J. M. Perkins, E. M. Grieveson, K. Theuwissen, D. W. McComb, P. D. Nellist and V. Nicolosi, *Science*, 2011, **331**, 568-571.
126. B. Valter, M. K. Ram and C. Nicolini, *Langmuir*, 2002, **18**, 1535-1541.
127. P. L. Cullen, K. M. Cox, M. K. Bin Subhan, L. Picco, O. D. Payton, D. J. Buckley, T. S. Miller, S. A. Hodge, N. T. Skipper, V. Tileli and C. A. Howard, *Nat Chem*, 2017, **9**, 244-249.
128. B. W. Erickson, S. Coquoz, J. D. Adams, D. J. Burns and G. E. Fantner, *Beilstein J Nanotech*, 2012, **3**, 747-758.
129. Z. H. Zhang, K. Leinenweber, M. Bauer, L. A. J. Garvie, P. F. McMillan and G. H. Wolf, *J Am Chem Soc*, 2001, **123**, 7788-7796.
130. P. F. McMillan, V. Lees, E. Quirico, G. Montagnac, A. Sella, B. Reynard, P. Simon, E. Bailey, M. Deifallah and F. Cora, *J Solid State Chem*, 2009, **182**, 2670-2677.
131. M. J. Bojdys, J. O. Muller, M. Antonietti and A. Thomas, *Chem-Eur J*, 2008, **14**, 8177-8182.
132. C. Fettkenhauer, J. Weber, M. Antonietti and D. Dontsova, *Rsc Adv*, 2014, **4**, 40803-40811.
133. C. F. Macrae, I. J. Bruno, J. A. Chisholm, P. R. Edgington, P. McCabe, E. Pidcock, L. Rodriguez-Monge, R. Taylor, J. van de Streek and P. A. Wood, *J Appl Crystallogr*, 2008, **41**, 466-470.
134. C. F. Macrae, P. R. Edgington, P. McCabe, E. Pidcock, G. P. Shields, R. Taylor, M. Towler and J. van De Streek, *J Appl Crystallogr*, 2006, **39**, 453-457.
135. J. B. Aladekomo and R. H. Bragg, *Carbon*, 1990, **28**, 897-906.
136. R. D. Shannon, *Acta Crystallogr A*, 1976, **32**, 751-767.
137. S. Britto, S. Joseph and P. V. Kamath, *J Chem Sci*, 2010, **122**, 751-756.
138. A. P. Dementjev, A. de Graaf, M. C. M. van de Sanden, K. I. Maslakov, A. V. Naumkin and A. A. Serov, *Diam Relat Mater*, 2000, **9**, 1904-1907.
139. C. D. Wagner, L. E. Davis, M. V. Zeller, J. A. Taylor, R. H. Raymond and L. H. Gale, *Surf Interface Anal*, 1981, **3**, 211-225.
140. A. C. Ferrari, S. E. Rodil and J. Robertson, *Phys Rev B*, 2003, **67**.
141. S. E. Rodil, A. C. Ferrari, J. Robertson and S. Muhl, *Thin Solid Films*, 2002, **420**, 122-131.
142. B. Jurgens, E. Irran, J. Senker, P. Kroll, H. Muller and W. Schnick, *J Am Chem Soc*, 2003, **125**, 10288-10300.
143. A. I. Finkel'shtein, *Zhurnal Obshchei Khimii*, 1961, **31**, 1132.
144. A. I. Finkelshtein and E. N. Boitsov, *Russ Chem Rev*, 1962, **31**, 712-720.
145. M. K. Marchewka, *J. Chem. Res.*, 2003, **2003**, 518-521.
146. A. C. Ferrari, S. E. Rodil and J. Robertson, *Diam Relat Mater*, 2003, **12**, 905-910.
147. Y. H. Cheng, B. K. Tay, S. P. Lau, X. Shi, X. L. Qiao, J. G. Chen, Y. P. Wu and C. S. Xie, *Applied Physics a-Materials Science & Processing*, 2001, **73**, 341-345.
148. C. Casiraghi, A. C. Ferrari and J. Robertson, *Phys Rev B*, 2005, **72**.
149. M. J. Bojdys, N. Severin, J. P. Rabe, A. I. Cooper, A. Thomas and M. Antonietti, *Macromol Rapid Comm*, 2013, **34**, 850-854.
150. M. J. Bojdys, Max Planck Institute of Colloids and Interfaces, 2009.

151. H. Z. Dai, X. C. Gao, E. Z. Liu, Y. H. Yang, W. Q. Hou, L. M. Kang, J. Fan and X. Y. Hu, *Diam Relat Mater*, 2013, **38**, 109-117.
152. X. F. Li, J. Zhang, L. H. Shen, Y. M. Ma, W. W. Lei, Q. L. Cui and G. T. Zou, *Applied Physics a-Materials Science & Processing*, 2009, **94**, 387-392.
153. K. Schwinghammer, M. B. Mesch, V. Duppel, C. Ziegler, J. Senker and B. V. Lotsch, *J Am Chem Soc*, 2014, **136**, 1730-1733.
154. D. D. L. Chung, *J Mater Sci*, 2002, **37**, 1475-1489.
155. A. B. Jorge, D. J. Martin, M. T. S. Dhanoa, A. S. Rahman, N. Makwana, J. Tang, A. Sella, F. Cora, S. Firth, J. A. Darr and P. F. McMillan, *J Phys Chem C*, 2013, **117**, 7178-7185.
156. S. Stankovich, D. A. Dikin, R. D. Piner, K. A. Kohlhaas, A. Kleinhammes, Y. Jia, Y. Wu, S. T. Nguyen and R. S. Ruoff, *Carbon*, 2007, **45**, 1558-1565.
157. M. Lotya, Y. Hernandez, P. J. King, R. J. Smith, V. Nicolosi, L. S. Karlsson, F. M. Blighe, S. De, Z. Wang, I. T. McGovern, G. S. Duesberg and J. N. Coleman, *J Am Chem Soc*, 2009, **131**, 3611-3620.
158. C. J. Shih, A. Vijayaraghavan, R. Krishnan, R. Sharma, J. H. Han, M. H. Ham, Z. Jin, S. Lin, G. L. C. Paulus, N. F. Reuel, Q. H. Wang, D. Blankschtein and M. S. Strano, *Nat. Nanotechnol.*, 2011, **6**, 439-445.
159. J. N. Coleman, M. Lotya, A. O’Neill, S. D. Bergin, P. J. King, U. Khan, K. Young, A. Gaucher, S. De, R. J. Smith, I. V. Shvets, S. K. Arora, G. Stanton, H. Y. Kim, K. Lee, G. T. Kim, G. S. Duesberg, T. Hallam, J. J. Boland, J. J. Wang, J. F. Donegan, J. C. Grunlan, G. Moriarty, A. Shmeliov, R. J. Nicholls, J. M. Perkins, E. M. Grieveson, K. Theuwissen, D. W. McComb, P. D. Nellist and V. Nicolosi, *Science*, 2011, **331**, 568-571.
160. G. Eda, H. Yamaguchi, D. Voiry, T. Fujita, M. Chen and M. Chhowalla, *Nano Lett.*, 2011, **11**, 5111-5116.
161. P. Joensen, R. F. Frindt and S. R. Morrison, *Mater. Res. Bull.*, 1986, **21**, 457-461.
162. V. Nicolosi, M. Chhowalla, M. G. Kanatzidis, M. S. Strano and J. N. Coleman, *Science*, 2013, **340**.
163. A. C. Ferrari, F. Bonaccorso, V. Fal'ko, K. S. Novoselov, S. Roche, P. Boggild, S. Borini, F. H. L. Koppens, V. Palermo, N. Pugno, J. A. Garrido, R. Sordan, A. Bianco, L. Ballerini, M. Prato, E. Lidorikis, J. Kivioja, C. Marinelli, T. Ryhanen, A. Morpurgo, J. N. Coleman, V. Nicolosi, L. Colombo, A. Fert, M. Garcia-Hernandez, A. Bachtold, G. F. Schneider, F. Guinea, C. Dekker, M. Barbone, Z. Sun, C. Galiotis, A. N. Grigorenko, G. Konstantatos, A. Kis, M. Katsnelson, L. Vandersypen, A. Loiseau, V. Morandi, D. Neumaier, E. Treossi, V. Pellegrini, M. Polini, A. Tredicucci, G. M. Williams, B. Hee Hong, J. H. Ahn, J. Min Kim, H. Zirath, B. J. van Wees, H. van der Zant, L. Occhipinti, A. Di Matteo, I. A. Kinloch, T. Seyller, E. Quesnel, X. Feng, K. Teo, N. Rupesinghe, P. Hakonen, S. R. T. Neil, Q. Tannock, T. Lofwander and J. Kinaret, *Nanoscale*, 2015, **7**, 4598-4810.
164. L. M. Viculis, J. J. Mack, O. M. Mayer, H. T. Hahn and R. B. Kaner, *J Mater Chem*, 2005, **15**, 974-978.
165. G. Eda, H. Yamaguchi, D. Voiry, T. Fujita, M. W. Chen and M. Chhowalla, *Nano Lett*, 2011, **11**, 5111-5116.
166. P. Niu, L. L. Zhang, G. Liu and H. M. Cheng, *Adv Funct Mater*, 2012, **22**, 4763-4770.
167. A. K. Gupta and M. Gupta, *Biomaterials*, 2005, **26**, 3995-4021.
168. G. Schmid, *Chem Rev*, 1992, **92**, 1709-1727.
169. C. A. S. Batista, R. G. Larson and N. A. Kotov, *Science*, 2015, **350**.
170. A. W. A. D. McNaught, M. Nic, J. Jirat, B. Kosata, A. Jenkins, *IUPAC. Compendium of Chemical Terminology, 2nd ed. (the "Gold Book"*, Blackwell Scientific Publications, 1997.
171. J. Yguerabide and E. E. Yguerabide, *Anal Biochem*, 1998, **262**, 137-156.
172. R. J. Hunter, *Zeta potential in colloid science : principles and applications*, Academic Press, London ; New York, 1981.

173. W. W. Liu, J. N. Wang and X. X. Wang, *Nanoscale*, 2012, **4**, 425-428.
174. A. N. J. Rodgers, M. Velicky and R. A. W. Dryfe, *Langmuir*, 2015, **31**, 13068-13076.
175. N. Arjmandi, W. Van Roy, L. Lagae and G. Borghs, *Anal Chem*, 2012, **84**, 8490-8496.
176. F. Y. Ke, Y. K. Luu, M. Hadjiargyrou and D. H. Liang, *Plos One*, 2010, **5**.
177. J. N. Coleman, *Accounts Chem Res*, 2013, **46**, 14-22.
178. Z. M. Markovic, D. M. Matijasevic, V. B. Pavlovic, S. P. Jovanovic, I. D. Holclajtner-Antunovic, Z. Spitalsky, M. Micusik, M. D. Dramicanin, D. D. Milivojevic, M. P. Niksic and B. M. T. Markovic, *J Colloid Interf Sci*, 2017, **500**, 30-43.
179. P. B. Rim and J. P. Runt, *Macromolecules*, 1984, **17**, 1520-1526.
180. W. H. Qi, *Accounts Chem Res*, 2016, **49**, 1587-1595.
181. M. Alcoutlabi and G. B. McKenna, *J Phys-Condens Mat*, 2005, **17**, R461-R524.
182. S. L. Lai, J. Y. Guo, V. Petrova, G. Ramanath and L. H. Allen, *Phys Rev Lett*, 1996, **77**, 99-102.
183. J. P. Koppes, A. R. Muza, E. A. Stach and C. H. Handwerker, *Phys Rev Lett*, 2010, **104**.
184. C. J. Shearer, A. D. Slattery, A. J. Stapleton, J. G. Shapter and C. T. Gibson, *Nanotechnology*, 2016, **27**.
185. J. Liu, Y. Liu, N. Liu, Y. Han, X. Zhang, H. Huang, Y. Lifshitz, S. T. Lee, J. Zhong and Z. Kang, *Science*, 2015, **347**, 970-974.
186. X. Wang, K. Maeda, A. Thomas, K. Takanabe, G. Xin, J. M. Carlsson, K. Domen and M. Antonietti, *Nat Mater*, 2009, **8**, 76-80.
187. F. Su, S. C. Mathew, G. Lipner, X. Fu, M. Antonietti, S. Blechert and X. Wang, *J Am Chem Soc*, 2010, **132**, 16299-16301.
188. Z. Gan, H. Xu and Y. Hao, *Nanoscale*, 2016, **8**, 7794-7807.
189. O. Kozák, M. Sudolská, G. Pramanik, P. Cígler, M. Otyepka and R. Zbořil, *Chem. Mater.*, 2016, **28**, 4085-4128.
190. T.-F. Yeh, C.-Y. Teng, L.-C. Chen, S.-J. Chen and H. Teng, *J. Mater. Chem. A*, 2016, **4**, 2014-2048.
191. H. Li, F. Q. Shao, H. Huang, J. J. Feng and A. J. Wang, *Sens. Actuators B Chem.*, 2016, **226**, 506-511.
192. S. Liu, J. Tian, L. Wang, Y. Luo, J. Zhai and X. Sun, *J. Mater. Chem.*, 2011, **21**, 11726-11729.
193. C. Merschjann, S. Tschierlei, T. Tyborski, K. Kailasam, S. Orthmann, D. Hollmann, T. Schedel-Niedrig, A. Thomas and S. Lochbrunner, *Adv. Mater.*, 2015, **27**, 7993-7999.
194. C. Merschjann, T. Tyborski, S. Orthmann, F. Yang, K. Schwarzburg, M. Lublow, M. C. Lux-Steiner and T. Schedel-Niedrig, *Phys. Rev. B*, 2013, **87**, 205204.
195. F. Guo, J. L. Chen, M. W. Zhang, B. F. Gao, B. Z. Lin and Y. L. Chen, *J Mater Chem A*, 2016, **4**, 10806-10809.
196. S. C. Yan, Z. S. Li and Z. G. Zou, *Langmuir*, 2009, **25**, 10397-10401.
197. Q. J. Xiang, J. G. Yu and M. Jaroniec, *J Phys Chem C*, 2011, **115**, 7355-7363.
198. Y. Hou, J. Y. Li, Z. H. Wen, S. M. Cui, C. Yuan and J. H. Chen, *Nano Energy*, 2014, **8**, 157-164.
199. S. A. Ladva, W. Travis, R. Quesada-Cabrera, M. Rosillo-Lopez, A. Afandi, Y. Li, R. B. Jackman, J. C. Bear, I. P. Parkin, C. Blackman, C. G. Salzmann and R. G. Palgrave, *Nanoscale*, 2017, DOI: 10.1039/C7NR06489F.
200. T. L. Barr and S. Seal, *J Vac Sci Technol A*, 1995, **13**, 1239-1246.
201. H. Piao and N. S. McIntyre, *Surf Interface Anal*, 2002, **33**, 591-594.
202. A. Yanilmaz, A. Tomak, B. Akbali, C. Bacaksiz, E. Ozceri, O. Ari, R. T. Senger, Y. Selamet and H. M. Zareie, *Rsc Adv*, 2017, **7**, 28383-28392.
203. X. W. Li, S. H. Zhang and Q. Wang, *Phys Chem Chem Phys*, 2013, **15**, 7142-7146.
204. J. Cui, S. H. Liang and J. M. Zhang, *Phys Chem Chem Phys*, 2016, **18**, 25388-25393.
205. A. Hashmi, M. U. Farooq, T. Hu and J. Hong, *J Phys Chem C*, 2015, **119**, 1859-1866.

206. M. J. Bojdys, 2009.
207. Z. Xing, Z. C. Ju, Y. L. Zhao, J. L. Wan, Y. B. Zhu, Y. H. Qiang and Y. T. Qian, *Sci Rep-Uk*, 2016, **6**.